Ladislaus Lang-Quantzendorff, BSc

MICROSTRUCTURE DEVELOPMENT OF THERMOMECHANICALLY TREATED MAGNESIUM ALLOYS AM50 AND ZK40

MASTER'S THESIS

to achieve the university degree of

Diplom-Ingenieur

Master's degree programme: Advanced Materials Science

submitted to

Graz University of Technology

Supervisor

Assoc.Prof Dr.tech Maria Cecilia Poletti

Dr.techn Fernando Gustavo Warchomicka

Institute for materials science, joining and forming

Graz, January 2019

AFFIDAVIT

I declare that I have authored this thesis independently, that I have not used other than the declared sources/resources, and that I have explicitly indicated all material which has been quoted either literally or by content from the sources used. The text document uploaded to TUGRAZonline is identical to the present master‘s thesis.

Date

Signature

Content

Abstract

Over the last decades magnesium alloys have gained increasingly importance as materials for lightweight constructions. Whilst, due to the hexagonal structure, the larger amount of magnesium components has been produced by casting, better mechanical properties suggest a deeper study of the metallurgical phenomena of hot deformation.

This thesis has dealt with the deformation behaviour of AM50 magnesium alloy at large deformations, provoked by free end torsion tests. Hot torsion tests using a Gleeble 3800 have been performed at temperatures between 250 °C and 400 °C and for strain rates ranging from 10^{-3}/s to 1/s. The obtained flow curves have shown a strong influence of strain rate and temperature. The flow behaviour has correlated with the microstructure of the deformed material. Due to progressed recovery and recrystallization processes a fine grained structure has occurred at temperatures higher than 300 °C and at low strain rates. The formed larger fraction and homogeneous distribution of recrystallized grains has allowed higher strains. Light optical microscopy and electron backscattered diffraction have provided information about microstructures at differently advanced steps of recrystallization. Prominent indications of continuous dynamic recrystallization by progressive lattice rotation have appeared, as well as the evolution of twins at different strain rates. Furthermore, discontinuous dynamic recrystallization has been observed, which is more likely at higher temperatures for the present alloy.

Detailed knowledge about deformation mechanisms delivers data to predict material behaviour for various forming processes and can be used to optimise microstructure and texture. This objective has been applied to magnesium alloys AM50 and ZK40 in the innovative method of friction stir processing (FSP). The applied process parameters have shown a promising surface appearance especially for ZK40. Intense plastic deformation has resulted in significant grain refinement. Recrystallized grains have been observed with diameters ranging from 1 to 5 µm for AM50. In ZK40 indications of a refined microstructure by continuous dynamic recrystallization have been found in the thermomechanical affected zone. For these microstructural changes an enhancement of mechanical properties and further improvement of the corrosion resistance is expected. The latter is crucial for biomedical application.

Kurzfassung

In den vergangenen Jahren hat Magnesium zunehmend an Bedeutung als Leichtbaumaterial gewonnen. Während bisher der größte Teil der Magnesiumkomponenten wegen hexagonaler Kristallstruktur gusstechnisch hergestellt wurde, ist eine tiefgreifende Untersuchung des Warmumformverhaltens aufgrund besserer mechanischer Eigenschaften lohnenswert.

Diese Arbeit widmet sich dem Umformverhalten der Magnesiumlegierung AM50 bei hohen Dehnungen, die durch Verwindungsprüfung bei axialem Spiel erreicht werden. Experimente mit einer Gleeble 3800 bei Temperaturen zwischen 250 °C und 400 °C verformten die Proben mit Dehnraten zwischen 10^{-3}/s und 1/s. Die gewonnenen Fließkurven wiesen ausgeprägte Abhängigkeiten zu Temperatur und Dehnrate auf, wobei sich deren Verhalten in der Mikrostruktur des verformten Materials wiederspiegelte. Nach Verformung bei Temperaturen über 300 °C mit geringen Dehnraten entstand durch fortgeschrittene Erholung und Rekristallisation eine feinkörnige Struktur. Der damit größere Anteil homogen verteilter rekristallisierter Körner bewirkte eine höhere Dehnbarkeit. In fortschreitenden Stadien konnte die Mikrostruktur mittels Licht- und Elektronenmikroskopie untersucht werden, wobei charakteristische Anzeichen kontinuierlicher dynamischer Rekristallisation durch fortschreitende Gefügedrehung, sowie die Zwillingsneigung bei unterschiedlichen Temperaturen und Dehnraten beobachtet werden konnte. Auch Hinweise diskontinuierlicher dynamischer Rekristallisation, die besonders bei höheren Temperaturen auftreten, traten dabei ans Licht.

Das erlangte Wissen über Verformungsmechanismen liefert nicht nur Daten für verschiedenste Umformvorgänge, sondern vermag auch zur Verbesserung von Mikrostruktur- und Oberflächeneigenschaften beizutragen. Zu deren Erprobung wurde mittels Rührreibverfahren die Oberfläche der Legierungen ZK40 und AM50 modifiziert. Die vielversprechende Oberflächenerscheinung insbesondere bei ZK40 zeugt von einer glücklichen Wahl der Prozessparameter, wobei deren intensive plastische Verformung in eine deutliche Kornfeinung mündete. Die rekristallisierten Körner erreichten in AM50 Durchmesser zwischen 1 und 5 µm. In der thermomechanisch beeinflussten Zone in ZK40 gab es Anzeichen kontinuierlicher dynamischer Rekristallisation, die für die Kornfeinung verantwortlich gemacht werden kann. Eine Verbesserung der mechanischen Eigenschaften wird aufgrund dieser mikrostrukturellen Veränderungen erwartet. Genauso soll die Korrosionsbeständigkeit zunehmen, was einem Einsatz als Biomaterial zugutekommt.

Danksagung

Zuallererst möchte ich mich bei Prof. Maria Cecilia Poletti und Dr. Fernando Warchomicka bedanken, die sich bereiterklärt haben, meine Arbeit zu betreuen, mir eine attraktive Themenstellung zusammenstellten, Wege fanden diese nach meinen Vorstellungen anzupassen und in zahlreichen Unklarheiten rasche Abhilfe leisteten. Außerdem sei dem FWF gedankt, der finanzielle Mittel für die Arbeit im Rahmen des Projekts F35014 Torsion von Metallen - Thermomechanical processing of metals at moderate and large strains bereitstellte.

Des Weiteren danke ich allen Mitarbeiterinnen und Mitarbeitern des Instituts, die an dem Zustandekommen der Arbeit und am Finden von Lösungen für unerwartete Fälle beteiligt waren, insbesondere was Hilfestellungen im organisatorischen Bereich, bei den Gleeble- und Rührreibversuchen, bei der Probenpräparation und den EBSD-Messungen betrifft.

Dem gegenüber möchte ich auch all jenen danken, die auf mich verzichten mussten. Meiner Familie, die für körperliches und seelisches Heil sorgt, den Pfadfindern, denen ich nun in einer neuen Rolle begegne, und allen Freunden, mit denen ich mich schon seit langem treffen wollte. Andererseits danke ich auch einem Menschen, mit dem ich mit dieser Arbeit noch näher zusammenwachsen durfte, in der Hoffnung ihm gleich viel gegeben zu haben, wie ich selbst erfuhr in meinem Glück.

1 Introduction

Magnesium and its alloys are materials with high potential in all kinds of lightweight application. A substantial lower density compared to aluminium alloys makes them attractive, providing a high specific stiffness and a high specific strength. Energy efficient constructions as well as special applications, for instance as biomedical implant, gain importance as a field of research. Taking the present development into account the investigation of this light metal is promising for a wide field of industries.

Due to the hexagonal structure, the larger amount of magnesium has been produced by casting, however better properties can be obtained by plastic deformation. Therefore, a deeper study of the metallurgical phenomena of hot deformation is of large interest. The profit of this research is useful for classical forming processes, but also for friction stir processing (FSP) as an innovative method. This industrial process allows severe plastic deformation. As result the material recrystallizes, which terminates in a significant grain refinement. This characteristic enhances not only mechanical properties but also the corrosion resistance. [1], [2]

The friction stir process changes the microstructure by macroscopic adjustments, which have a complex relationship to their effect on the material. The machine does not have the possibility to measure strain rates and temperatures exerted to the material.

By contrast, torsion tests enable exactly controlled deformations at set temperatures and strain rates. As in torsion tests mainly shear forces act, higher strains can be obtained experimentally compared to compression and tensile tests. Their outcome should help to understand the microstructural development happening during friction stir processing, but can also be the foundation for the investigations of a variety of deformation processes.

This thesis has the following objectives:

- Analysis of the deformation behaviour of AM50 by means of hot torsion tests by calculation of flow curves out of the process data.
- Find correlations between the flow behaviour and the final microstructure of the deformed samples.
- Testing of the principal processability of friction stir processing on AM50 and ZK40.
- Find an attempt to draw parallels between the torsion test and friction stir processing.
- Investigation of the microstructure of Mg alloys to gain knowledge about the restoration mechanisms happening during deformation by torsion and friction stir processing via light optical microscopy and electron backscattered diffraction.

Present developments in the regarding fields of research are summarised in the state of the art. The methodology describes the delivered material, the sequence of torsion testing, the applied friction stir processes and metallographic methods. This section is followed by a summary of the results. In the discussion the results are correlated with the formulated goals of this work. Finally, conclusions can be drawn with an outlook for future research.

2 State of the art

2.1 Magnesium and magnesium alloys

Magnesium is a silver-white light metal, 30% lighter than Aluminium. Its appearance in the earth's crust is with 1.95% at eighth position. Due to its high reactivity, however, it is always bound in compounds as typically silicates, carbonates, sulphides or chlorides. Large amounts of magnesium are also dissolved in sea water. [3]

Magnesium and its alloys are the lightest structural metallic materials. In comparison with aluminium alloys the mechanical properties generally are lower. Nevertheless, values normalised on its density highlight its convincing properties for light constructions. Its hexagonal crystal structure restricts the gliding to three slip systems. Therefore, magnesium alloys are mostly produced cast materials. Due to the few existing slip systems in the hexagonal crystal and the low tendency to twin building, pure magnesium has a low ductility at room temperature and a low strength. Consequently, in most cases it is used in an alloyed form. [4]

The standard potential of pure magnesium is very low in acids and bases, but at normal conditions significantly higher. This signifies a protection by a stable oxidation layer. Nevertheless, the poor corrosion resistance is among to the most important limitations of this materials group. The flammability is an additionally challenging aspect in the progress of alloying. [5], [6]

The atomic diameter enables a wide range of solute elements, as aluminium, zinc, cerium, silver, thorium, yttrium and zirconium in peritectic or eutectic systems. Different types of intermetallic phases form, which have important effects on the mechanical and corrosion properties. The following list contains the most commonly used alloying elements and their properties [6]:

- **Aluminium**: improves castability, solid solution hardening and precipitation hardening
- **Calcium**: grain refinement, improving creep resistance
- **Lithium**: reduces density, solid solution hardening
- **Manganese**: controls the iron content, improves corrosion resistance, refines precipitates
- **Rare earth metals**: reduce microporosity, improve creep properties and corrosion resistance, solid solution and precipitation hardening
- **Zinc**: increases melt fluidity, and strength at ambient temperatures, precipitation hardening
- **Zirconium**: most effective grain refiner

2.1.1 AM50

AM50 is a magnesium alloy containing approximately 5 wt.% Aluminium and 0.15 to 0.5 wt% manganese. The adequate strength and better corrosion resistance compared to other alloys justify the wide use of alloys from the AM-series. The manganese reduces the harmful iron concentration and builds intermetallic particles with aluminium. The AM50 alloy is well castable and well suited for die casting, but research also deals with the formability of the alloy. Table 1 displays its composition. [1], [7], [8]

In general the microstructure contains coarse precipitates of β-$Mg_{17}Al_{12}$ phase and Al–Mn inclusions [9]. It has a quite high ductility and fracture toughness, because of a reduction in the amount of $Mg_{17}Al_{12}$ around grain boundaries [7]. Furthermore, it has a good energy absorption at high strength [1]. The mechanical properties are listed in Table 2.

Table 1: Content of alloying elements in AM50 and ZK40 in weight percent [9], [10], [11], [12], [13].

[wt%]	Al	Zn	Zr	Mn	Fe	Cu	Si	Ni
AM50	4.5…5.5	< 0.2		0.15…0.5	< 0.004	< 0.01	< 0.05	< 0.001
ZK40		3.5…5.0	0.28…0.53	0.003	0.002	0.014	0.007	0.018

Table 2: Mechanical properties of AM50 and ZK40 as cast material at room temperature [9], [10], [12], [13], [14], [15].

	Tensile yield stress [MPa]	Tensile strength [MPa]	Elongation at failure [%]	Compressive yield stress [MPa]	Compressive strength [MPa]	Young's modulus [GPa]
<SAM 50	120…125	195…230	8…15	110	113	45
ZK40	92…108	134…240	3…17	92…125	361…369	64…68

2.1.2 ZK40

ZK40 is an extrusion and wrought alloy with very good deformability for medium and high strength application [1]. Investigations on cast material suggest also an application in this very condition [16], [10], [12]. The alloy contains zinc and zirconium, other alloying elements are restricted to very low amounts (Table 1).

Zirconium acts as nucleation site for grain refinement, while zinc segregates on the solid-liquid interface and restricts the grain growth. In a σ-Mg(Zn-Zr) solid solution MgZn precipitates accumulate at the grain boundaries [12]. By zirconium addition the solubility of zinc increases drastically [17]. Additionally, zirconium has a positive effect on the corrosion resistance of the alloy [10].

The material is strengthened mainly by grain refinement and due to the Orowan mechanism [18]. As the Zn-Zr intermetallic compounds have a very high melting temperature, the creep resistance is enhanced [17]. The mechanical properties for as cast condition are shown in Table 2.

ZK40 as biomaterial

The effects of magnesium, zinc and zirconium on the human body are described as negligible or really beneficial. This circumstance makes it possible, to use the alloy in the human body as so-called biomaterial. A biomaterial mostly is distinguished from any other material by its ability to exist in contact with human tissue, without causing an unacceptable degree of harm [19].

Magnesium is called as macroelement for bones and teeth and has numerous functions in the human body. The risk of toxic accumulation is assessed to be very low. Zinc is a typical trace element, though harmful for growth, development and health in high doses. Zirconium can cause irritations in certain compounds. Nevertheless, it is judged as best biocompatible element. [20] [21]

In contrast to conventional metallic implant materials like titanium alloys or steels, magnesium alloys degrade in the tissue. This has big advantages especially for growing children. No inhibition of the growth is feared also without a secondary operation. [22]

Metallic biomaterials usually are applied as implants in contact with bone. A typical cause for implant failure can be the mismatch of the elastic moduli between human tissue (especially bone) and the implant. A stress shielding effect may arise when some areas of the bone are unloaded, whereas the load in the implant becomes unpleasantly high. This clinical phenomenon triggers the resorption of implant surrounding tissue [23]. Bone has a very low elastic modulus compared

to conventional implant materials. However, with magnesium a quite low elastic modulus can be reached, also as bulk material. [24]

2.1.3 Hot deformation of magnesium

The deformation of magnesium and its alloys is predominantly driven by the hexagonal crystal structure. Figure 1 describes the hexagonal crystal with its possible slip systems and the twin evolution. Basal slip systems have a low critical resolved shear stress to enable deformation. By contrast, a higher resolved shear stress enables twinning, where tensile twins occur at lower stresses than compression twins. Hence, a tension-compression anisotropy develops in the material. However, for higher strains also the activation of non-basal (prismatic and pyramidal) slip is necessary, though this takes place only at elevated temperatures to a relevant amount. [6], [25]

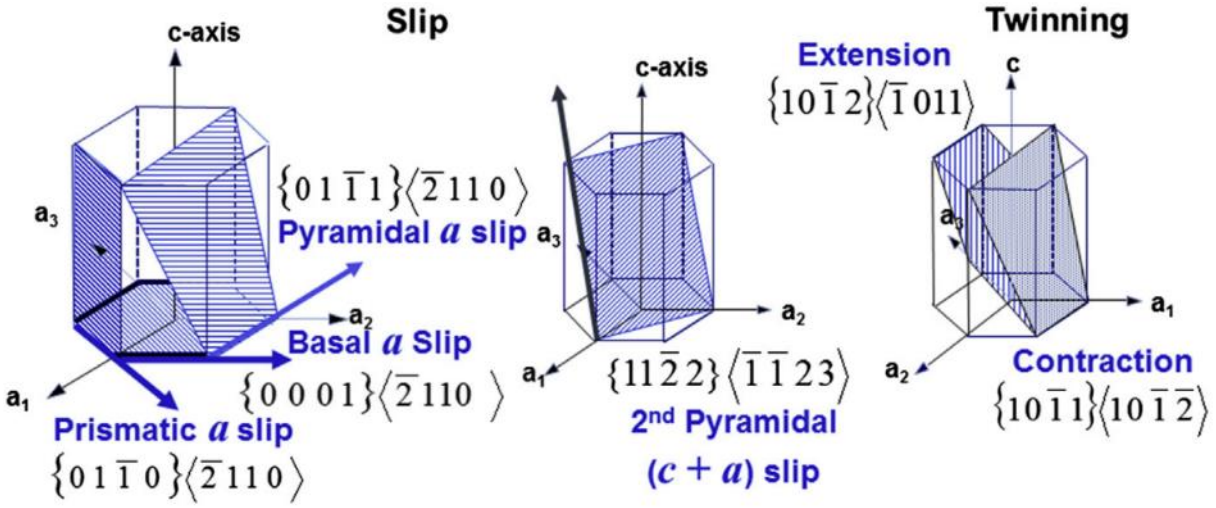

Figure 1: Slip and twinning systems in magnesium alloys [6].

Hot deformations are denoted as thermomechanical processes, which activate dynamic recovery and recrystallization. Due to the thermodynamic instability of deformed materials, there is a tendency to remove defects from the structure to reach ordered states of lower energy. This diffusional process happens only very slow, unless activation energy is supplied for instance by heat. [26]

In materials of high stacking fault energy at high temperatures dynamic recovery is the main occuring restoration mechanism at hot deformation, which causes a rearrangement of dislocations to subgrains. In materials of lower stacking fault energy dynamic recrystallization is more likely to occur. [26]

The evolution of recrystallization textures is related to the nature of the nucleation event, the orientation dependency and the nature, energy and mobility of boundaries between grains of various orientations [26]. A general distinction is made between continuous dynamic recrystallization and discontinuous dynamic recrystallization [27].

Continuous dynamic recrystallization evolves from a recovery process, by the continuous absorption of dislocations at grain boundaries. New grains form in areas of low dislocation content separated by high angle grain boundaries. This type of recrystallization occurs in two different types. The first process is called geometric, when the grain boundaries of severely deformed grains get closeer, until their serrations become comparable in size with their distance. Due to the stable subgrain size, which is independent of the strain, homogeneously sized new grains form, as Figure 2 illustrates. [26], [27]

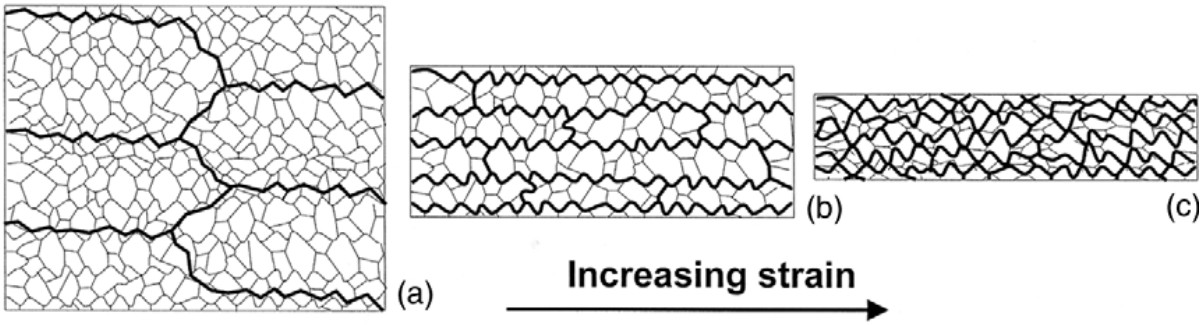

Figure 2: Evolution of geometric dynamic recrystallization by increasing strain [26].

Figure 3 illustrates the second process of continuous dynamic recrystallization by progressive lattice rotation. By strain induction subgrains rotate and boundaries migrate in subordinate amount. Subsequently, from the centre to the edge of a deformed grain, subgrains of increasingly higher misorientation occur. Simultaneously, the amount of high angle boundaries increases. Magnesium is prone to evolve by this recrystallization process thorugh progressive lattice rotation, due to its lack of slip systems and local shearing near to the grain boundaries. However, at higher temperatures the activation of nonbasal slip enables more homogeneous deformation with a preference for discontinuous dynamic recrystallization. [26]

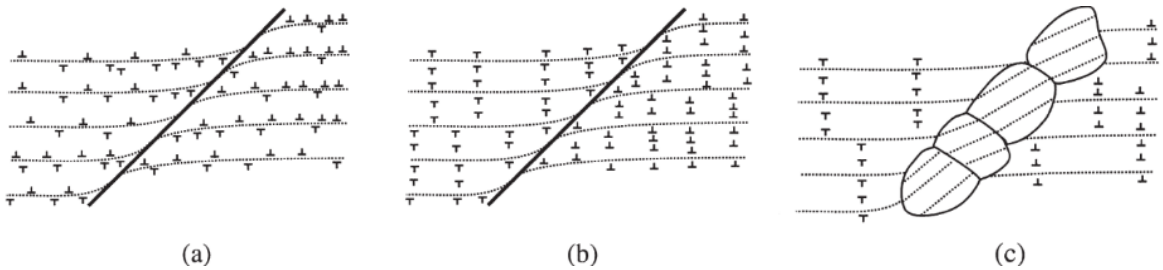

Figure 3: Proposed evolution of dynamic recrystallization by progressive lattice rotation. a) Local shearing, b) recovery, c) new (sub)grains.

Discontinuous dynamic recrystallization has its origin in the nucleation at existing and in advanced stadium also at new grain boundaries. Strain-induced grain boundary migration and bulging are typical introducing events, before the grains grow to alloy-specific extensions, which are depending on the density and distribution of dislocations. A necklace structure forms around existing grains, when the initial grain size is much larger than the size of recrystallized grains (Figure 4 b – c) [26].

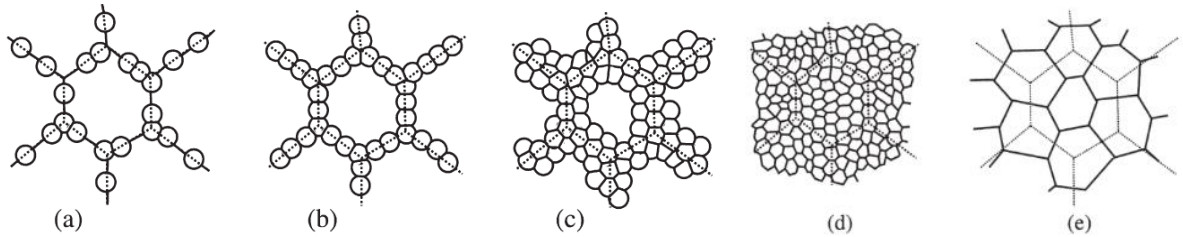

Figure 4: a – d) Evolution of discontinuous dynamic recrystallization. e) result after small initial grain size.

In magnesium alloys continuous dynamic recrystallization is described as the main restoration mechanism, which has also been described for torsion [28]. Contrary at higher temperatures also discontinuous effects have occurred [27] [29]. The mechanisms of dislocation motion for a ZK60 magnesium alloy during hot compression using transmission electron microscopy are described in [30]. Accordingly, the restoration mechanism in the material strongly depends on strain rate and temperature. For a strain rate of 0.001/s and temperatures of 350 °C and 400 °C continuous

dynamic recrystallization was found to progress by the formation of new recrystallized grains along existing grain boundaries. This happens through single gliding dislocations climbing into subgrain boundaries, which increases the misorientation of the subgrain boundaries. This is accompanied by grain boundary migration and results in the successive formation of a necklace of recrystallized grains around a parent grain. If the underlying mechanism is not investigated, however, this could easily be attributed to discontinuous dynamic recrystallization. Also, for high strain rates of 1/s and 350 °C and 400 °C continuous dynamic recrystallization was observed, though with a different mechanism including dislocation pile-ups and their rearrangement by dislocations climbing. Beside these dominant continuous mechanisms, discontinuous dynamic recrystallization was found for a deformation at 400 °C and 0.01/s strain rate. The higher temperature facilitates the migration of grain boundaries. Together with an accumulation of gliding dislocations in front of subgrain boundaries a bulging of these boundaries is caused, which was observed for hot compression of ZK60 only at 400 °C and not at 350 °C. [30]

For AZ31 the domain for discontinuous dynamic recrystallization was above 400 °C too. For the investigated tensile samples discontinuous dynamic recrystallization was identified from processing maps and microscopy at strain rates higher than 0.4/s. For lower temperatures and strain rates solely continuous dynamic recrystallization was observed. [31]

Additionally, also twin aided dynamic recrystallization has been observed in strain hardened AZ31. This phenomenon has its origin in the serration of twin boundaries, at which subsequently new grains build. It is explained by high local stress, which exceeds the critical resolved one at the twin boundaries, activating c + a dislocation slip. [32].

The restoration in the investigated alloys was reported describing different mechanisms. For AM50 new built grains were observed after rolling nucleating at the grain boundaries and in regions of twinning [33]. In friction stir processed AM50 a rearrangement of dislocations, which terminates in a grain subdivition, is reported [2]. This effect is correlated with a continuous recrystallization mechanism.

An investigation on compressed ZK40 compared to rare earth containing alloys showed, that continuous dynamic recrystallization predominantly occurs. Also recrystallization at twins has been observed. By gadolinium addition the continuous effects are less pronounced and are replaced by discontinuous dynamic recrystallization [16].

2.2 Torsion testing

Classical methods for estimations on the deformability of materials are tensile and compression tests. At high strains samples in tensile tests suffer from necking due to strain localisations [34]. Compression tests are restricted to relatively low strains by the expansion of undeformed areas with progressing strains [35]. In contrast, it is possible to achieve large deformations by free end torsion tests. The torsion test supplies torque and torsion, which can be modified to effective values of stress and strain. As the strain within the sample is linearly dependent on the radial position of observation, the torque is the sum of all single stresses over the sample´s cross section. Therefore, effective values for stress and strain are assumed, which describe the flow curves independent of the type of the test. [35], [36] From the experimental flow stresses the deformation behaviour up to high strains can be determinded, which makes hot torsion tests interesting for the investigation of the hot workability of materials [36].

Theoretically, torsion causes pure shear in the sample. Consequently, very high strains evolve. [37] These are responsible for dynamic recovery and recrystallization processes at high temperatures [38].

2.3 Friction stir processing

Friction stir processing (FSP) is a technique similar to friction stir welding, which is applied to modify the microstructure of metallic materials in surface near layers. It is possible to incorporate different elements into the surface to produce alloys or composites, to enhance welding joints or to produce fine grained structures, which is especially interesting for cast material. Additionally, it enhances mechanical properties and the corrosion resistance and reduces existing porosity. The principle of the process is depicted in Figure 5. [39]

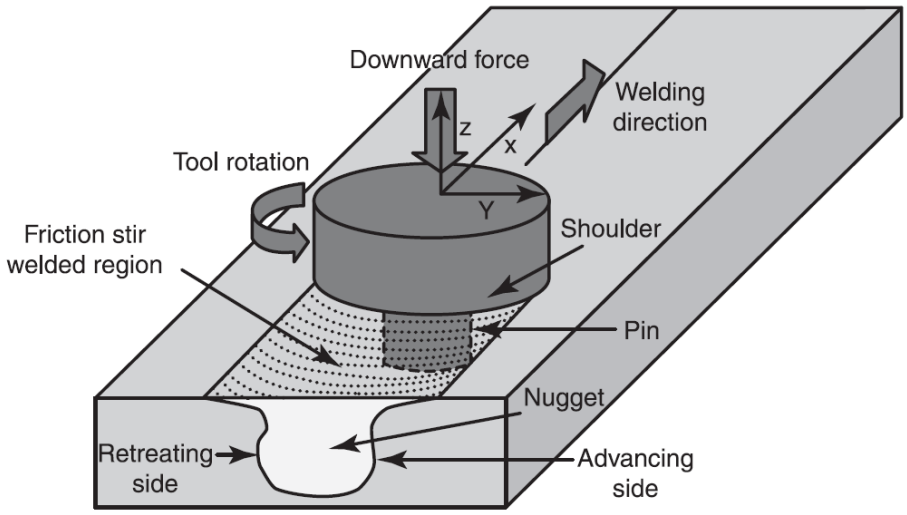

Figure 5: Scheme of friction stir welding [40]. *Friction stir processing differs solely by the application on one single part.*

The process is based on the rotational movement of the cylindrical tool, which causes friction on the sample´s surface and within the processed material. Consequently, heat evolves, which enables the tool to cause plastic flow in the metal. The forwards moving tool leaves a wide stir zone. This zone consists of an advancing side, in which the material is moved forward by the tool, and a retreating side, where the material is pushed backwards. The central part of the stir zone is surrounded by a thermomechanically and a heat affected zone. [39]

The concept of friction stir processing has been applied for cast and wrought aluminium alloys, magnesium alloys, copper and titanium. To respond to the characteristics of different materials, the rotation speed and advance speed can be adapted. The tool can also be tilted and its penetration depth can be adjusted. Tools varying in material and geometry can be applied to different testing materials. Additionally, the sample's temperature can be regulated to a certain extent. Also, the usage of inert atmosphere may influence the process. [39]

FSP is restricted to flat surfaces and plastically deformable materials. Still the variety of processable materials is very large raning from metallic materials to polymers and composites [41]. A big advantage is the low heat input and therefore the lack of a pronounced heat affected zone and correlated problems as for other thermomechanical processes. [39]

As the temperature falls, when friction is decreased by material softening, an equilibrium establishes. Consequently, only as much heat develops as necessary. Thus the process allows rapid phase transformations and a steep gradient of strain, strain rate and temperature in the stirred zone. The sum of these aspects complicates the measurement and the predictability of the reaction of the microstructure on the process parameters. [42]

Friction stir processing or welding has been applied successfully on several magnesium alloys: AM50 [43], [44], AM60 [40], AZ31 [45], AZ61[46], AZ91 [47], ZK60 [48]. Rotational speeds between 600 and 1200 revolutions per minute and advancing speeds between 6 and 600 mm/min

are reported. AM50 has been processed with 2500 rev/min and 6 mm/min, grains of 2 to 10 μm were achieved [2]. A very high rotation speed of 6000 rev/min has been applied to ZK60 resulting in grains of approximately 8 μm [48].

Friction stir processing is particularly interesting for biocompatible alloys. The degradation of an implant should begin, when its task is fulfilled. This happens when the state of healing provides enough mechanical stability. The degradation rate should be as low, that the degradation products do not affect the organism harmfully. When implants degrade, not only the alloying elements dissolve in the surroundings, but also hydrogen gas evolves, with which the tissue has to deal with. [49]

Friction stir processing gives the possibilty to improve the corrosion resistance of different alloys [2]. The method does not cause severe metallurgical defects in the material in contrast to other surface treatments [48]. These numerous methods based on rolling, extrusion or bending have primarily a positive effect on the mechanical properties [22]. Friction stir processing, by contrast, can also reduce the corrosion rate for instance in ZK60 by more than one order of magnitude [48].

2.4 Comparison of torsion and friction stir processing

Table 3 displays the differences between free end torsion and friction stir processing. The parameters of pressure and strain rate are in a different order of magnitude, also the heating system is completely different for both processes, which results in deviating temperatures.

Table 3: Comparison between the carried out torsion tests and friction stir processing for magnesium alloys.

	Free end torsion tests	**Friction stir processing** [47]
Axial pressure	0 N/mm^2	10…100 N/mm^2
Strain rate	0.001…1/s	10…100/s
Heating	electrically by resistance	mechanically by friction
Temperature	250…400 °C	400...600 °C
Shear stress	in one dimension, local	multidimensional, interacting sideways
Process conditions	clearly defined by sample measurements and thermocouple controlling	influenced by physical properties of the material

3 Methodology

3.1 Material

3.1.1 AM50

The AM50 material was delivered as a cuboidally casted ingot. Its composition is listed in Table 4.

Table 4: Content of alloying elements in the delivered AM50 alloy [weight percent] [50].

Aluminium	Zinc	Manganese	Iron	Copper	Silicon	Nickel
4.7%	0.04%	0.3%	0.002%	0.005%	0.037%	0.001%

The first investigational step of the AM50 base material was a macroscopic and light microscopic investigation of the cross section, to find potential inhomogeneities. Subsequently, 24 torsion samples were lathed. The torsion axes of these samples correlated with the torsion axis of the friction stir sample, which was cut out of the material as a 10 mm thick plate.

Different trials of heat treatments (410 °C for 1 h, 2 h, 4 h, 8 h, 24 h) helped to dissolve intermetallic particles in the matrix. Via observation in the scanning electron microscope one single hour was sufficient to dissolve an appropriate amount of intermetallic phases. Therefore, the torsion samples heat treated in the furnace for 1 h at 410 °C.

3.1.2 ZK40

ZK40 was delivered discs of as cylindrically casted ingot with the label “Mg4%Zn0.5%Zr”. The chemical composition of the material was not analysed in more detail. Nevertheless, the content of alloying elements was assumed to be within the limits represented in Table 5.

Table 5: Limits of the content of alloying elements in ZK40 alloy [weight percent] [1].

Zinc	Zirconium	Copper	Nickel	others
3.5…4.5%	≥ 0.45%	≤ 0.1%	≤ 0.01%	≤ 0.30%

After a light microscopic investigation, the discs did not undergo further modifications for the usage in friction stir processing.

3.2 Torsion experiments on AM50

3.2.1 Experimental procedure

A Gleeble 3800 carried out free end torsion tests with AM50 alloy. Figure 6 shows the geometry of the manufactured samples. In the present case the gauge section in the centre of the samples had a length of A = 20 mm and a diameter of B = 10 mm. The sample was clamped on long hollow shafts. The clamps also served as contacts for the resistance heating, which heated the sample in axial direction. Figure 7 shows the welding position of three J-thermocouples, which measured the temperature during the experiments. Due to the low temperature gradient in the sample proved in a first trial, the signal of thermocouple 1 was able to control the heating in an appropriate way.

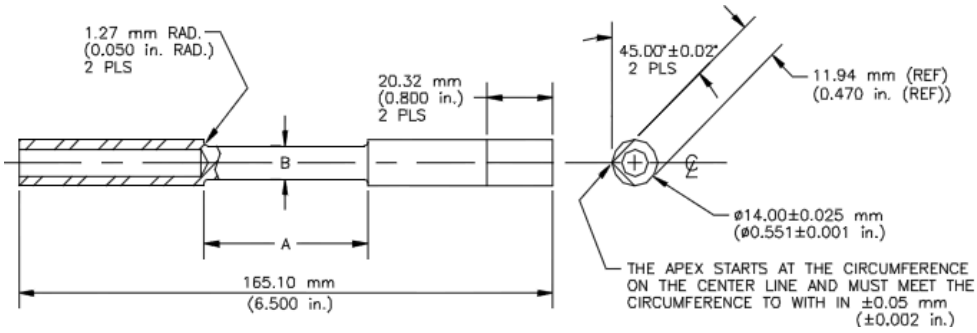

Figure 6: Geometry of the torsion samples [51]. *The measurements of A and B are displayed in Figure 7.*

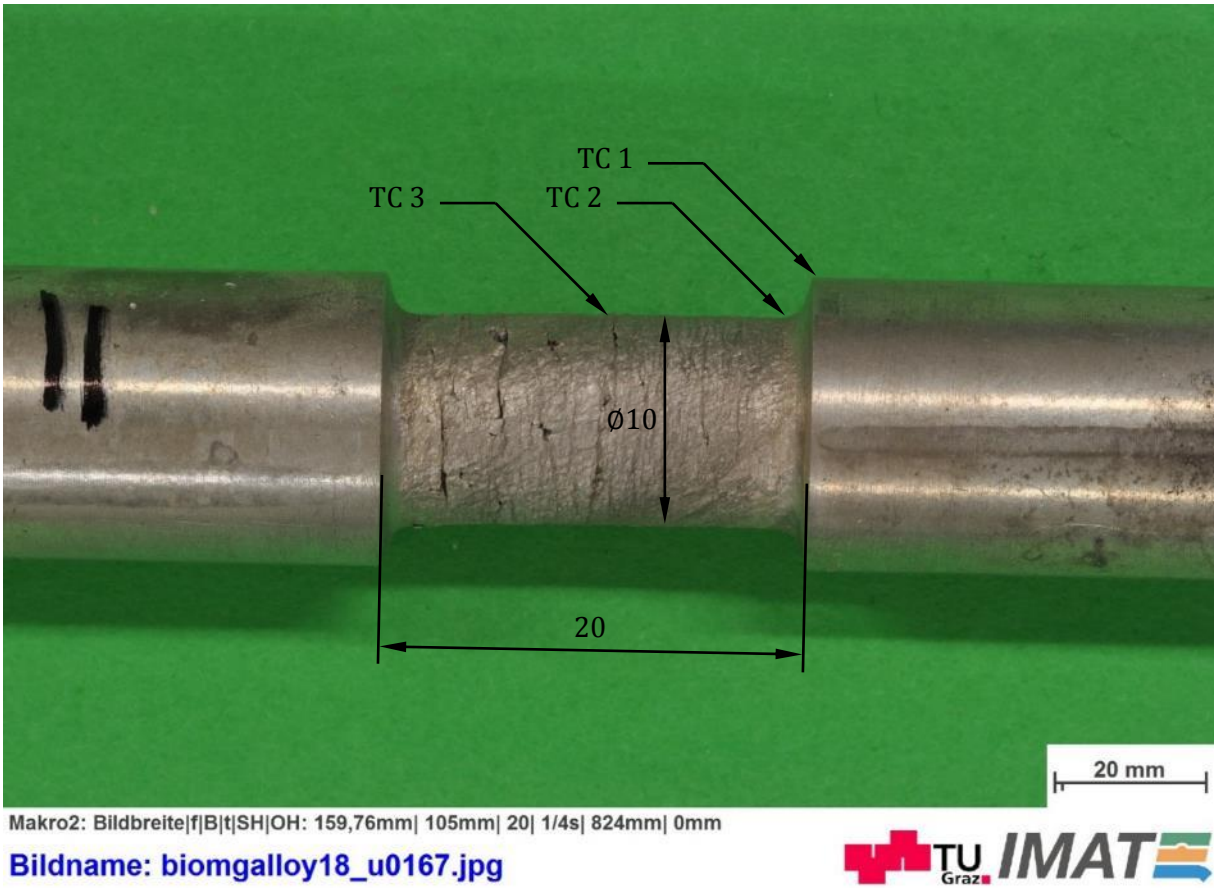

Figure 7: Central part of a torsion sample showing the location of the thermocouples, diameter and gauge length.

The following formula calculated the time of the experiment in which the machine wound the sample for N revolutions with a given strain rate $\dot{\varepsilon}$.

$$t[s] = \frac{N\pi}{2\sqrt{3}\dot{\varepsilon}} \qquad (1)$$

N was selected as high as possible for the present material. Unfortunately, this value could only be estimated by experience of preceding tests. Due to large variations in the achievable strains, some samples broke during testing after too many revolutions. By repetition of certain tests, questionable information could be completed.

Every experiment followed the same pattern, starting with a heating step to the required temperature with 2.5 K/min. In the next step the temperature was constant for 30 s, to guarantee its homogeneity over the whole sample. Then, the deformation took place, which terminated in an immediate water quenching. A scheme of the temperature program is shown in Figure 8.

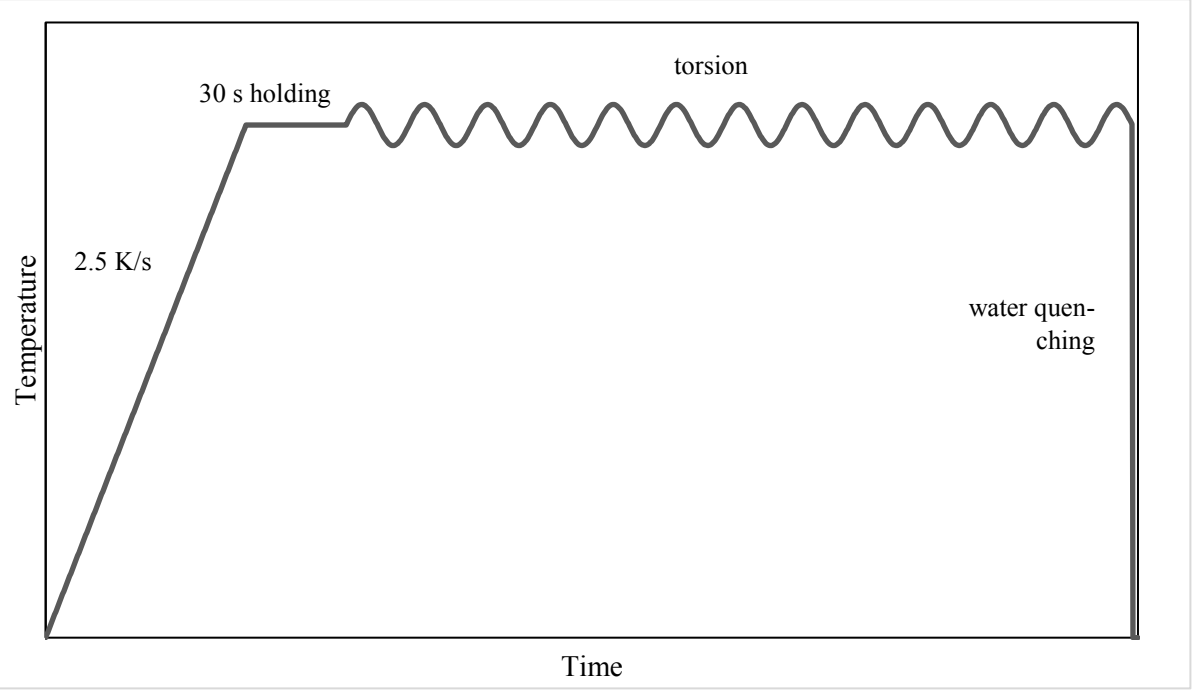

Figure 8: Temperature program for the torsion experiments in AM50.

The achievable strains during torsion are strongly depend on the test parameters. Table 6 shows the experimental conditions for all carried out torsion experiments.

Table 6: Torsion experiments and their achieved revolutions.

strain rate $\dot{\varepsilon}$	250 °C	300 °C	350 °C	400 °C
1	ε = 0.17	ε = 0.28	ε = 0.40	ε = 0.40
0.1	not performed	not performed	ε = 0.50	ε = 0.55
0.01	ε = 0.33	ε = 0.40	ε = 0.66	ε = 1.40
0.001	ε = 0.33	ε = 0.50	ε = 1.20	ε = 1.50

3.2.2 Flow curve calculation

During the experiments the testing machine recorded revolutions and torque of the process, as well as the temperatures of the welded thermocouples and data from the power supply.

In order to draw of flow curves torsion had to be transferred into the effective strain ε. The calculation considers the geometry of the sample with r as the radius and l as the gauge length. The divisor $\sqrt{3}$ has its origin in the von-Mises criterion. Then ε is calculated as follows:

$$\varepsilon[-] = \frac{N\ 2\pi\ r}{\sqrt{3}\ l} \qquad (2)$$

The effective stress σ mainly depends on the torque M, but its linear relationship is disturbed by the strain rate sensitivity m and the hardening coefficient n. The formula of Fields and Backofen calculates the effective stress σ, using the following terms for the calculation of n and m [37]:

$$\sigma\ [N/mm^2] = \frac{M\ \sqrt{3}\ 1000\ (3+n+m)}{2\pi\ r^3} \tag{3}$$

$$n = \frac{\partial log\sigma}{\partial log\varepsilon} \tag{4}$$

$$m = \frac{\partial log\sigma}{\partial log\dot{\varepsilon}} \tag{5}$$

Due to the dependency of n and m on the final effective stress, an iterative process is necessary, which requires starting values for n and m. In the first step a value of $n + m = 0.3$ was assumed by a rough estimation at intermediate temperatures, strain rates and strains. n was taken as constant over ε and m assumed to be constant over ε and $\dot{\varepsilon}$. Thus, each flow curve contained an individual constant value for n, whilst every m was valid for one temperature. Iteration steps were carried out, until the fifth decimal remained stable.

Figure 9 shows n estimated as the slope of a linear fit of the middle points of the *log σ/log ε* curve. The fit does not consider errors in the beginning of the curves and the softening occuring at higher strains.

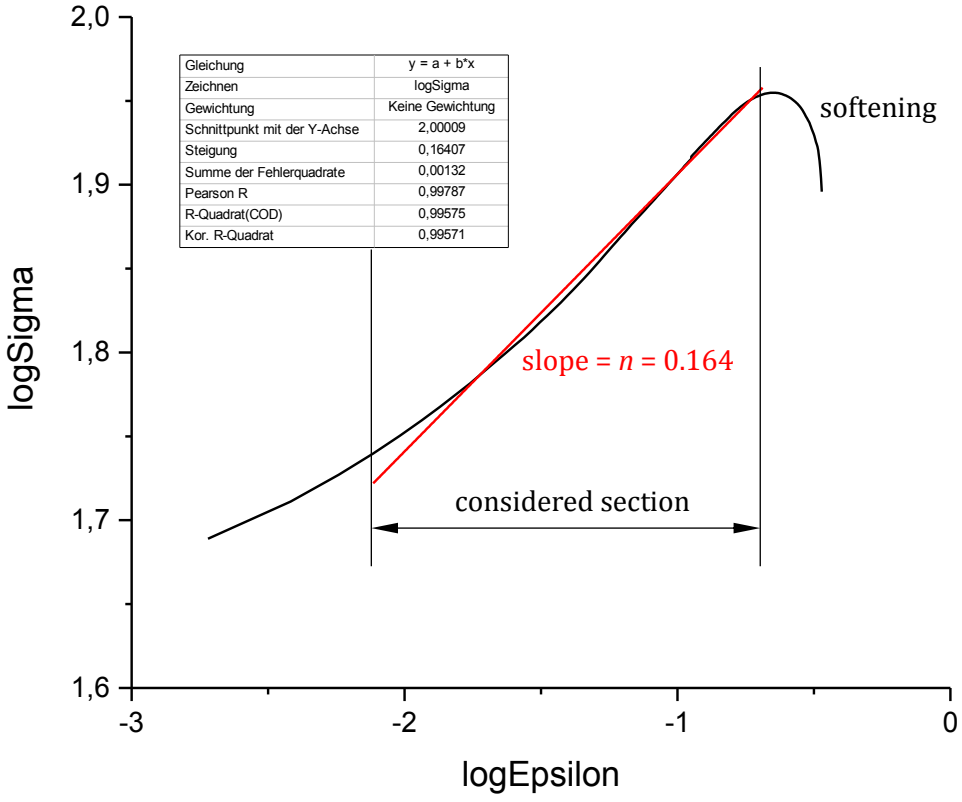

Figure 9: Example for the log σ/log ε curve at 300 °C and ε = 0.01. Linear fit of the central part of the curve. The softening at high ε is not considered.

Figure 10 illustrates the calculation of m. Single values of *log σ* at different strains ε were taken into account and plotted. m was obtained as an average value for every temperature out of the corresponding slope versus different strain rates.

Gleichung	y = a + b*x				
Zeichnen	logSigma	logSigma	logSigma	logSigma	logSigma
Gewichtung	Keine Gewichtung				
Schnittpunkt mit der Y-Achse	1,93755	2,00009	2,00009	2,00009	1,93755
Steigung	0,10547	0,13282	0,14063	0,16407	0,13282
Summe der Fehlerquadrate	0,00115	0,0021	0,00268	3,67984E-4	0
Pearson R	0,9905	0,98941	0,98789	0,99688	1
R-Quadrat(COD)	0,9811	0,97893	0,97593	0,99377	1
Kor. R-Quadrat	0,97165	0,9684	0,96389	0,98754	--

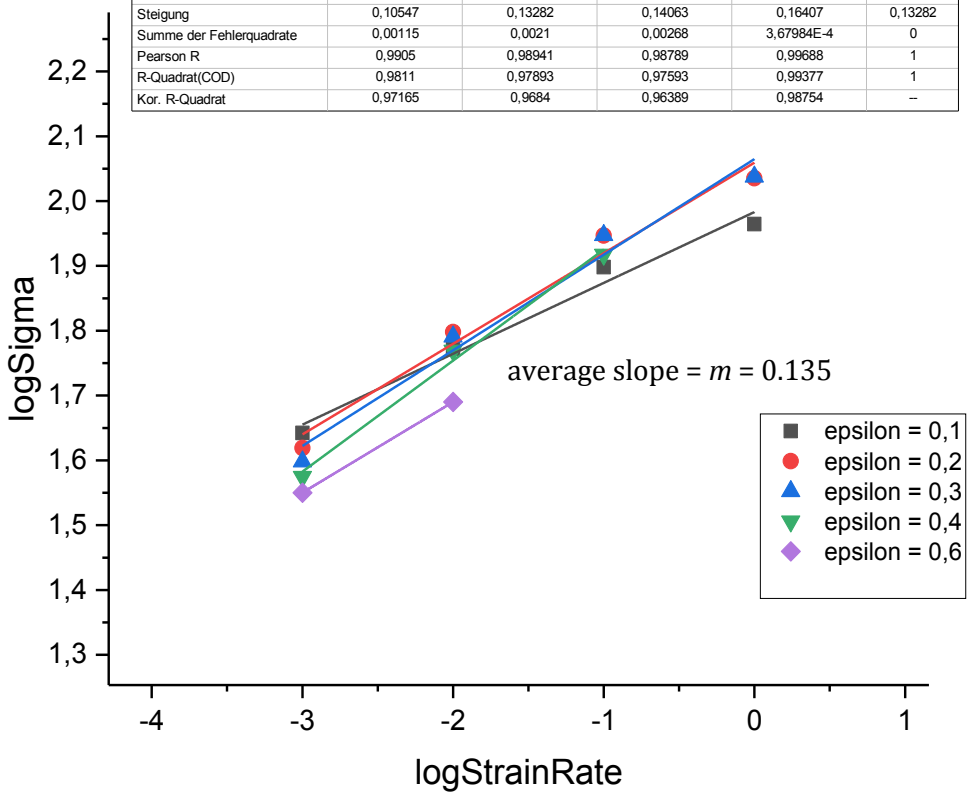

Figure 10: Linear fits of the log σ/log ε̇ curve at 350 °C and different strains. The m value is the average of the slopes.

Due to the low mechanical heating at strain rates smaller than 10/s, no temperature correction was applied.

3.3 Friction stir processing

A previous project of friction stir processing on a magnesium alloy suggested a tool with a concave shoulder (Ø18 mm) and a pin with a left hand thread [52]. This tool was applied also in the present case. The pin had a diameter of 10.4 mm and an adjustable length, which was adjusted to 3.3 mm. Figure 11 shows the geometry of the tool. The pin was extended to 5 mm, to make one out of three helical channels visible.

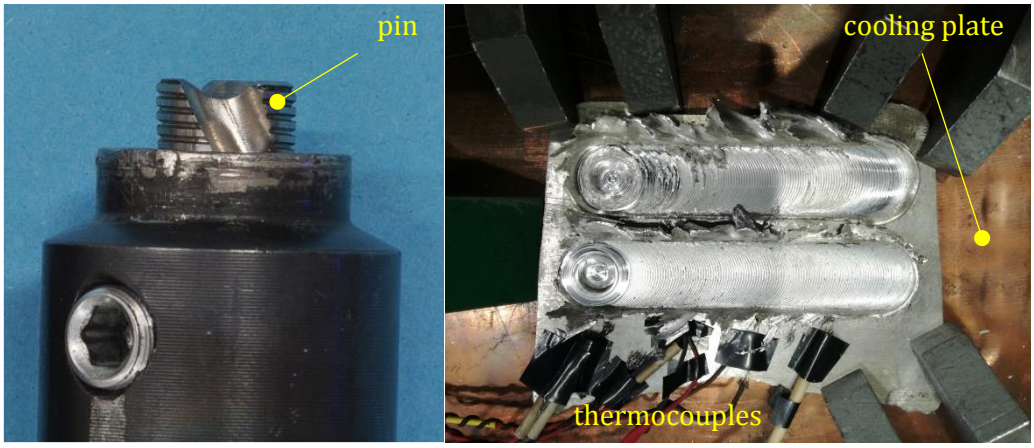

Figure 11: Left: FSP tool, pin length 5 mm [52]*. Right: clamped AM50 sample on the cooling plate.*

A cooling plate, supplied with 15 °C cooling water, reduced the samples temperature to avoid static recrystallization. Consequently, the sample´s bottom did not exceed temperatures which are prone to cause relevant lattice transformation. Figure 11 illustrates the clamping on the cooling plate. Seven K-thermocouples measured the temperature during the process in experiments 1 and 2 (AM50) according to Figure 12.

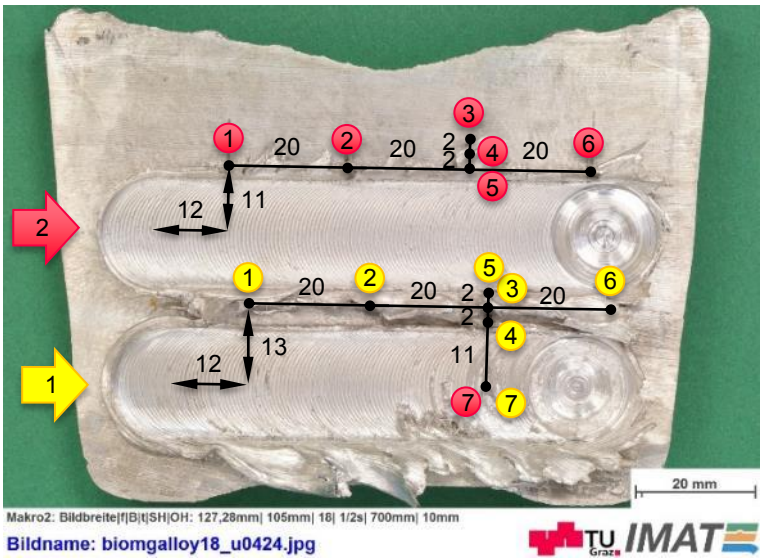

Figure 12: Positions of the thermocouples on AM50 for experiments 1 (yellow) and 2 (red). No. 7 is located on the bottom side of the sample and measures the temperature of the cooling plate in both experiments at the same position.

The friction stir process started with a cleaning of the tool by a dot weld with 100 rev/min in a piece of aluminium. After a manual positioning of the tool on the surface and a rotating submerging into the material the program started to perform a weld with 300 rev/min and an advance speed of 200 mm/min. During the whole process the tool was tilted 3 ° off the vertical direction.

3.3.1 Estimation of the process temperature

In different distances from the weld three thermocouples measured the temperature of the sample. A simple calculation was used to enlarge the knowledge about the temperature during the stir process. Therefore, an exponential equation was fitted into the existing measured temperatures. The equation contained the following assumptions:

- The temperature of the sample far from the weld is 15 °C.
- The temperature function is smooth with one maximum in the centre.
- The function is symmetric to the weld axis.

$$T[°C] = 15\ °C + e^{a+br+cr^2} \quad (6)$$

3.4 Metallography

3.4.1 Sample preparation

The first step of sample preparation was cutting the torsion and FSP samples to an appropriate size for metallography, see Figure 13. The torsion samples were cut in order to get a section through their axis that contains the maximum information regarding the deformation gradient within the sample. The plates tested in FSP were cut at different positions to investigate the stir zone over the progressing process.

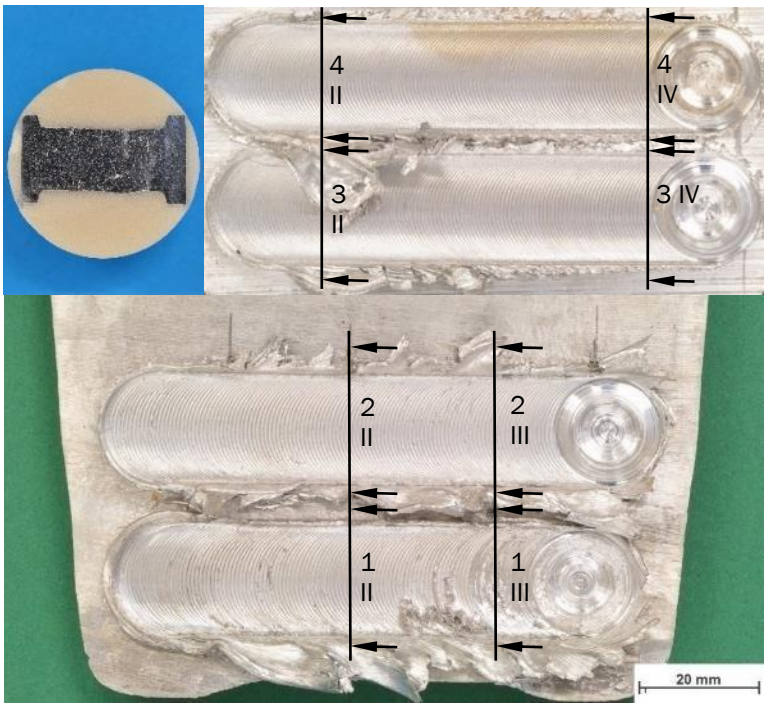

Figure 13: Samples prepared for metallography: AM50 embedded torsion sample (top left), FSP samples sections in ZK40 (top right) and AM50 (bottom).

Cold embedding resin was used for all samples, to avoid a modification of the microstructure. Struers LevoCit was suitable for this purpose, but had the drawback of high electrical resistivity, which is unfavourable for electron microscopy.

AM50

The sample preparation for metallography of magnesium alloys is associated with a lot of difficulties due to the low hardness and poor corrosion resistance. Table 7 describes grinding and polishing steps of the cylindrical samples with 30 mm diameter. As AM50 alloy is especially prone to rapid corrosion when contacted with water, water free polishing became apparent as the appropriate way for a surface quality adequate for light optical microscopy.

Table 7: guideline for the sample preparation of AM50 magnesium alloy.

	step description	**products**	**time**	**Force**	**speed**
1.	grinding on SiC foil, grits 800, 1200 and 2000	conventional water lubrication	2 min each grit	5 N (≙ 7073 Pa)	150 rpm (≙ 1.2 m/s)
2.	water free polishing with monocrystalline diamonds on Taffeta woven wool	DP-Paste M, 3 µm MD-Mol DP-Lubricant Yellow	20 min	5 N (≙ 7073 Pa)	50 rpm (≙ 0.4 m/s)

3.	water free polishing with polycrystalline diamonds on short synthetic nap	DP-Paste P, 1µm MD-Nap DP-Lubricant Yellow	20 min	5 N (≙ 7073 Pa)	50 rpm (≙ 0.4 m/s)
4.	manual polishing with a non-drying colloidal silica suspension (0.04 µm) on porous neoprene	OP-S NonDry MD Chem	30…60 s	powerful with one hand	100 rpm (≙ 0.8 m/s)

The listed grinding and polishing steps should help as a guideline for the preparation of AM50 samples, but do not represent an ideal sample preparation yet. The success and reproducibility varied strongly and was depending on meticulously hygienic working conditions. In the present study only the use of individually deviating methods and repetitions of the single preparation steps led to good results. As the last step, manual preparation of the samples enabled to polish each sample suitably to its needs. Now high pressure was put on the samples by hand to increase wear and hinder the growth of a corrosive layer. In spite of the low to intermediate stacking fault energy of the alloys, also for polishing with high force no preparation twins were observed.

After polishing, the samples were cleaned by rinsing with water and wiping off remaining dispersion by hand as fast as possible, followed by immediate flushing with a generous amount of ethanol. Every contact with water was be kept as short as possible. Drying was always carried out with cold air to prevent corrosion.

To enhance visibility of microstructural features in the light optical microscope, different methods were tested for AM50. The usual way to make grain boundaries visible by etching did not succeed, because selective attack of grain boundaries by the etchant always occurred simultaneously with significant surface corrosion. This corrosion appeared as irregular structure in the light optical microscope and hindered the observation of grains. Typical etching solutions for magnesium with picric or nitric acid were tested, but always caused serious surface damage by corrosion, before the grain structure was made visible (Figure 14). Finally, it was observed that the silica suspension used for polishing affected the superficial layers harmfully. Accordingly, after successful polishing with the steps of Table 7 a grain differentiation by polarised light was possible for AM50.

The second most important issue for sample preparation of magnesium after corrosion was scratching (Figure 15). To avoid this kind of damage, electrolytic preparation was tested. This contactless method removed effectively surface material with hardly any mechanical force applied on the sample. Electropolishing was performed with an electrolyte of 300 ml phosphoric acid (85%) in 225 ml ethanol (96%) and 188 ml distilled water at 10 V DC and achieved the complete removal of grinding scratches in one to three minutes. The electropolished samples showed a relatively rough surface due to the selective removal of different phases. While the matrix was worn off quite homogenously, undissolved intermetallic particles were sticking out of the surface. Accordingly, the electropolished samples were suitable for topographical analysis in the scanning electron microscope but did not permit a successful documentation in the light optical microscope due to the low depth of field of this method (Figure 14 right).

To enhance contrast for the electron backscattered diffraction analysis in the scanning electron microscope, etching with nital was used. Contrary to light optical microscopy, etched samples of AM50 gave remarkable results in EBSD analysis. The samples were etched with 1% nital solution (100 ml ethanol and 1 ml nitric acid) by rinsing for 20 seconds.

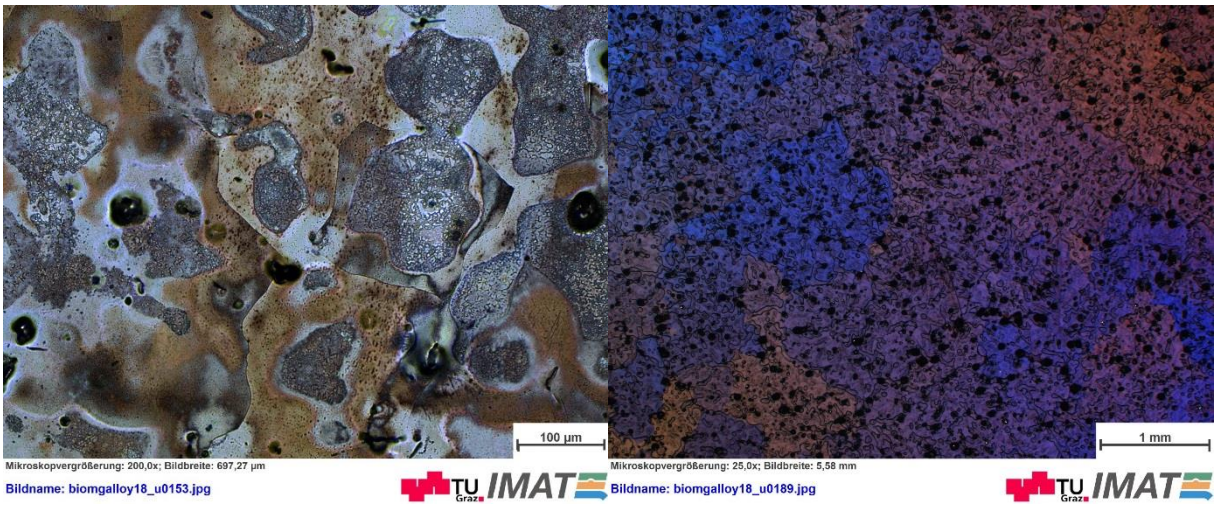

Figure 14: AM50 in the light optical microscope: left: corrosion after etching with picric acid; the surface corrodes, grain boundaries hardly come into appearance; right: after electropolishing, using polarised light; stains appear due to the low depth of field, a substructure occurs.

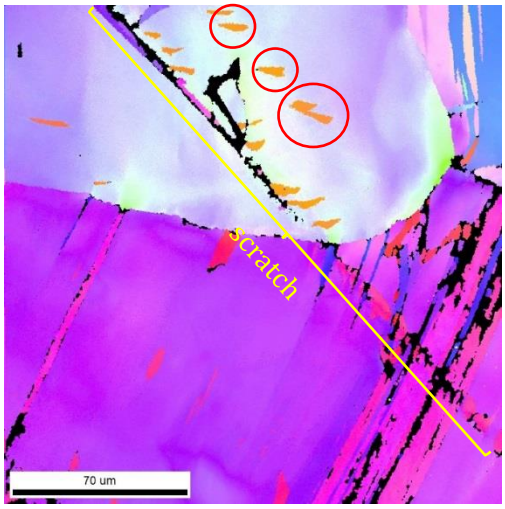

Figure 15: EBSD measurement in a AM50 torsion sample deformed at 250 °C with 1/s. Scratch caused by polishing accompanied by small twins (orange) directly at the scratch, but also parallel in the light blue grain.

ZK40

The grinding and polishing for ZK40 alloy was performed similar to AM50, see Table 7. The same method was successful and delivered a better reproducibility of preparation results compared to AM50. Exposure to the polishing silica suspension enhanced the visibility of different grains in the light optical microscope also without using polarised light.

Sample preparation for the scanning electron microscope showed only little success for ZK40 especially in the stir zone of the FSP samples. Electropolishing lead to severe corrosion. Etching with 1% nital solution for 20 seconds showed some success within the base material but did not succeed for the EBSD analysis of the stir zone of the FSP samples. Best results for the EBSD analysis of the ZK40 base material were obtained via extensive polishing. A short polishing step with standard OPS and high force was followed by polishing with pH-neutral silica suspension and without force on neoprene for 2h.

3.4.2 Light optical microscopy

Concerning the light optical microscopy, the applied methods were different for AM50 and ZK40. The grains of ZK40 were quite well visible in conventional bright field, displaying the grain structure of AM50 required polarised light in the used Zeiss Axio Observer Z1m microscope. The applicability of polarised light was restricted to magnifications of 100 to 200 times. Thus, for higher resolutions a scanning electron microscopic analysis was necessary.

3.4.3 Scanning electron microscopy

Two different methods in a TESCAN MIRA 3 scanning electron microscope revealed additional information to the purely optic of light microscopy. Energy dispersive X-ray analysis (EDX) supplied the composition of the different phases in the base material, which was used to calculate occurence of intermetallic compounds. Detailed evidence about the history of single grains was gained from electron backscattered diffraction measurements (EBSD). This data contained information about the deformation characteristics like deformation twins and deformed grains, as well as about features of the recrystallization processes. An EDAX Metek equipment measured the EDX and the EBSD data.

For EDX typically a voltage of 15 kV and a beam intensity of 12 was applied, to measure with a spot size of 10 nm. A TEAM software processed the EDX data.

For EBSD with voltages up to 30 kV and beam intensity 19 quite high confidence indices could be attained. These achieved on the average 0.6 in the best measurement (350 °C, 0.001/s), but were lower at low temperatures and high strain rates (0.2 at 250 °C, 0.001/s).

The EBSD measurements were carried out in windows of 500 x 1000 µm with 1 µm step size. The views of details had step sizes of 0.3 µm in areas of 200 x 200 µm.

For the evaluation of EBSD data the OIM analysis software was applied. The first adaptive step consisted of a standardisation of the confidence indices. As a preparation for the second step now larger areas of identical confidence index existed. A neighbour confidence index correlation altered the orientation of lower indexed points, to delate trustworthy grains to sharp boundaries. By an exclusion of remaining low indexed parts intermetallics, scratches and insecure measured points appeared black.

Grains were differentiated by a tolerance angle larger than 15 °. Boundaries with misorientations higher than 2 ° were indicated as low angle grain boundaries. This is in correlation with values from the literature [53].

4 Results

4.1 Materials microstructure

4.1.1 AM50

A first investigation of a base material plate through the cross section of the ingot shows a similar structure in wide ranges. Solely near to the surface a different appearance can be found, which is typical for the inhomogeneous cooling of cast products. Figure 16 displays the corresponding cross section. The macroscopic image contains areas of different appearance. A profounder investigation shows, that most of these differences occur due to inhomogeneous corrosion of the surface. In wide ranges grains of the same characteristics appear, pictured in detail (c). In the sections (a) and (b) large pores with diameters of 100 to 1200 µm occur.

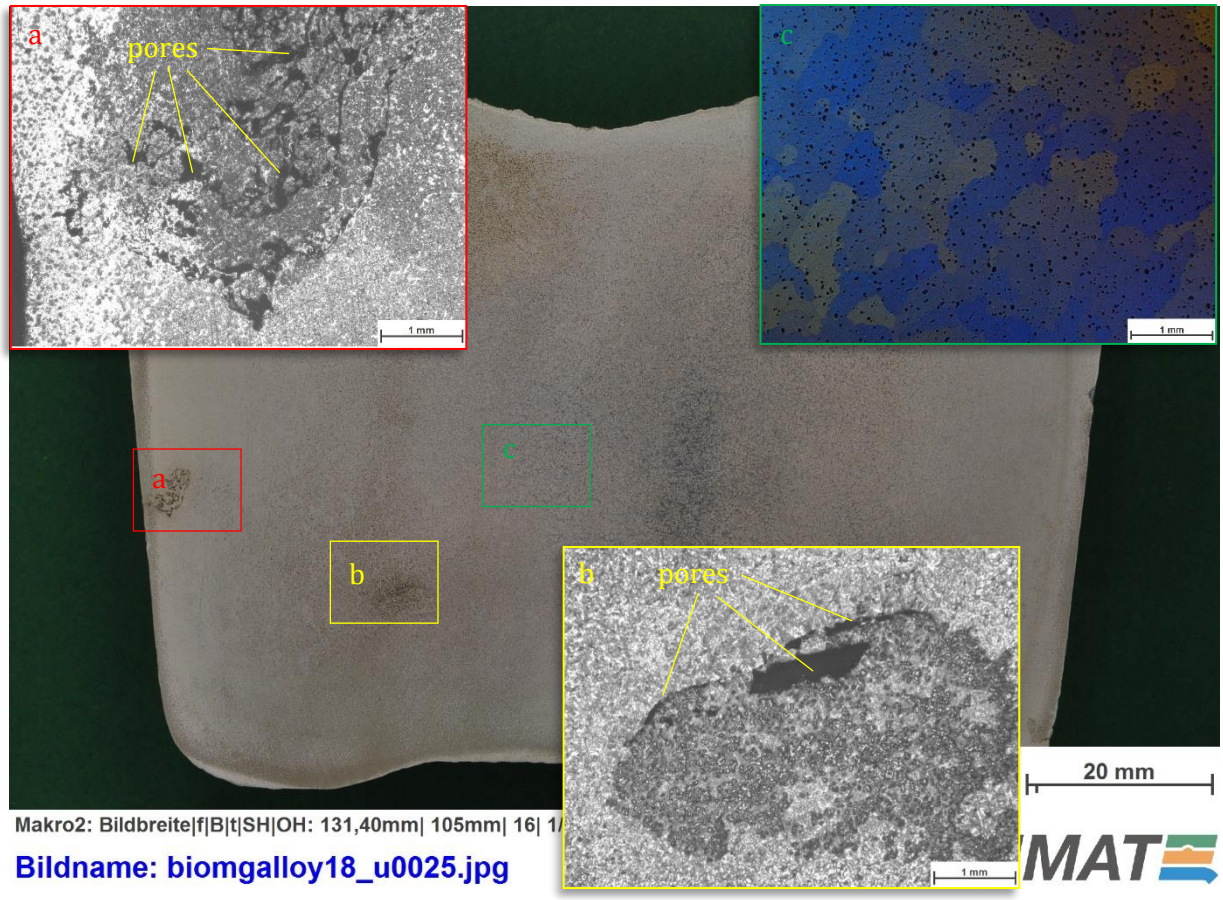

Figure 16: Cross section of the AM50 ingot. Most inhomogeneities are caused by sample preparation. Detail of the typical microstructure (c) and pores (a & b).

Figure 17 depicts the microstructure in as cast condition and after heat treatements at 410 °C. The AM50 alloy in as cast condition is characterised by large grains and a large amount of intermetallic particles, appearing as dots on the surface. A heat treatment at 410 °C dissolves most of the intermetallic compounds in the matrix in 24 h. A similar result can be obtained after one single hour. In the scanning electron microscope the visibility of intermetallic particles is enhanced (Figure 18).

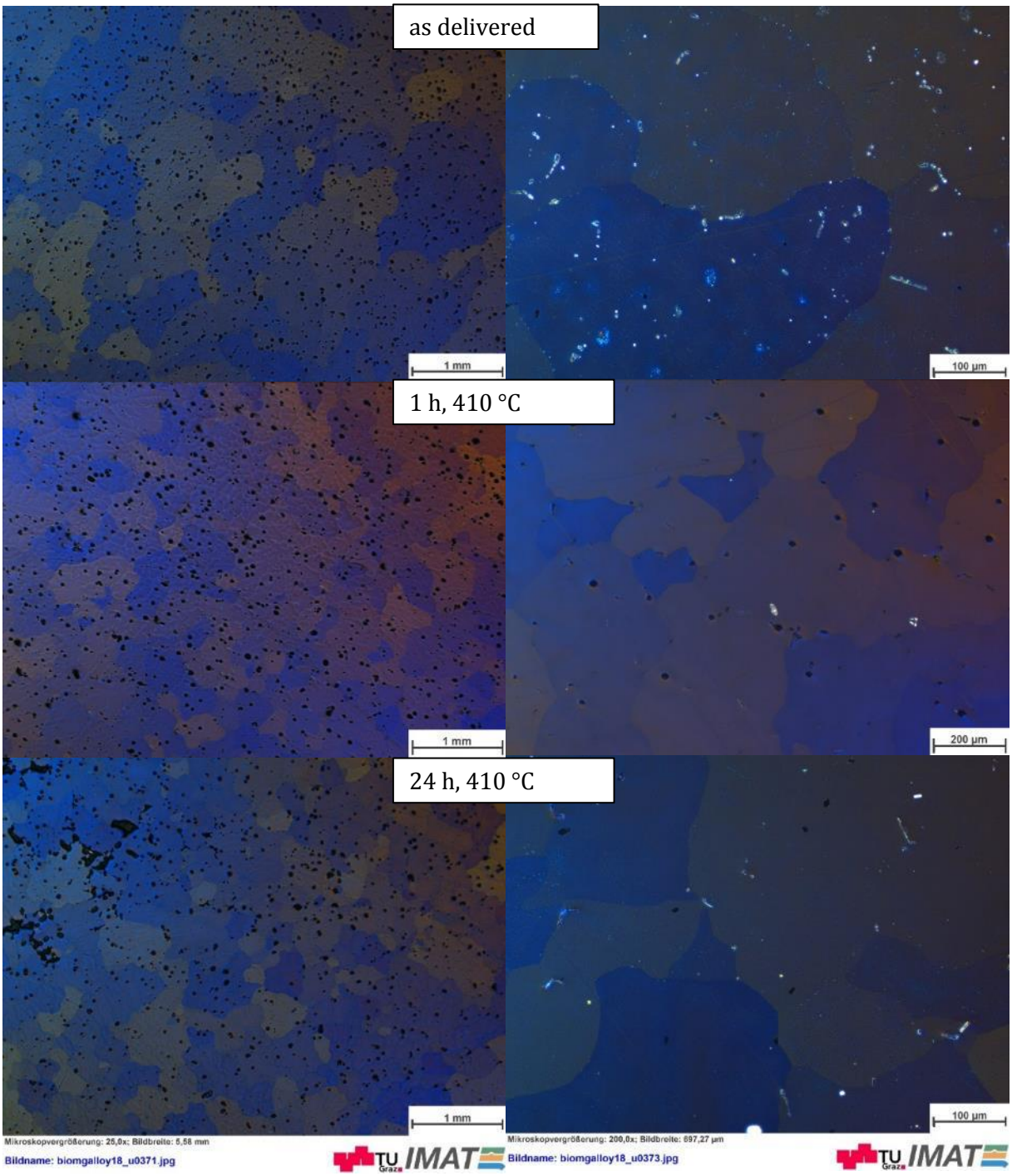

Figure 17: Microstructure of AM50 using polarised light. As delivered (top), after a 1 h, 410 °C (middle) and a 24 h, 410 °C heat treatment (bottom).

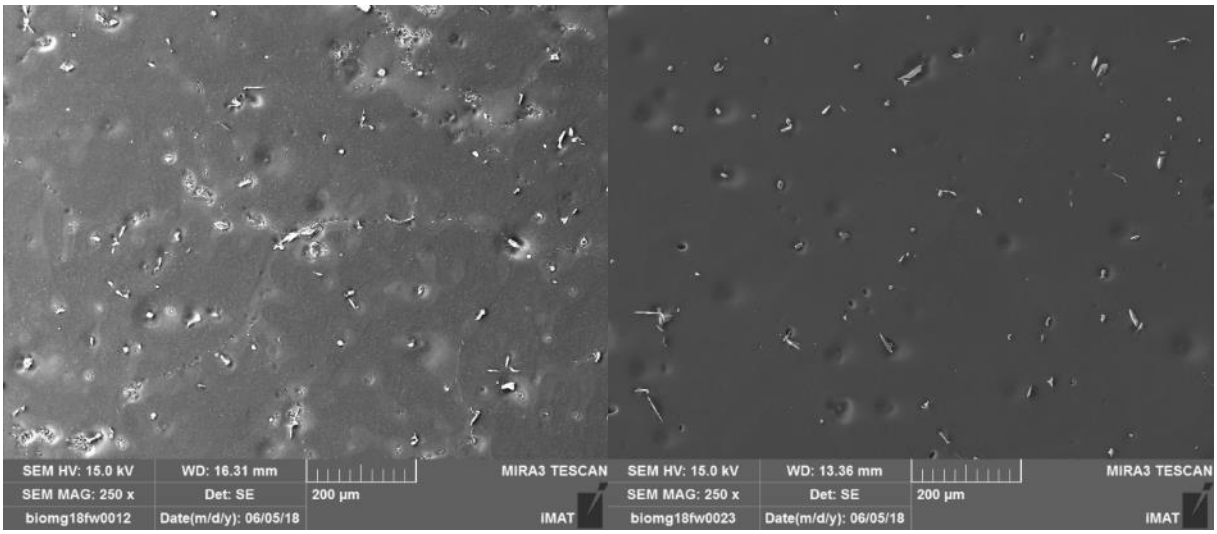

Figure 18: Scanning electron micrographs of the delivered AM50 (left), compared to a 24 h, 410 °C heat treated sample (right).

Energy dispersive X-ray spectroscopy gives evidence of the success of the heat treatment. Figure 19 displays the main components in the AM50 alloy. Whilst in the heat treated sample the surface appears smooth with singular clearly seperated particles, the sample in the as delivered condition is marked by a secondary phase, which appears near the grain boundaries. The spectroscopic analysis shows $Mg_{17}Al_{12}$ β-phase surrounded by a needle like α+β-eutecticum. After the heat treatment the α+β-eutecticum does not occur anymore, whilst β-particles remain in the material. The dissolution of this eutectic phase causes an acceptable homogenisation within the α-matrix. Remaining intermetallics in the structure cannot be avoided with a heat treatment of this kind, because the dissolution temperature of the Al_8Mn_5 phase is higher than the eutectic temperature of the alloy [54].

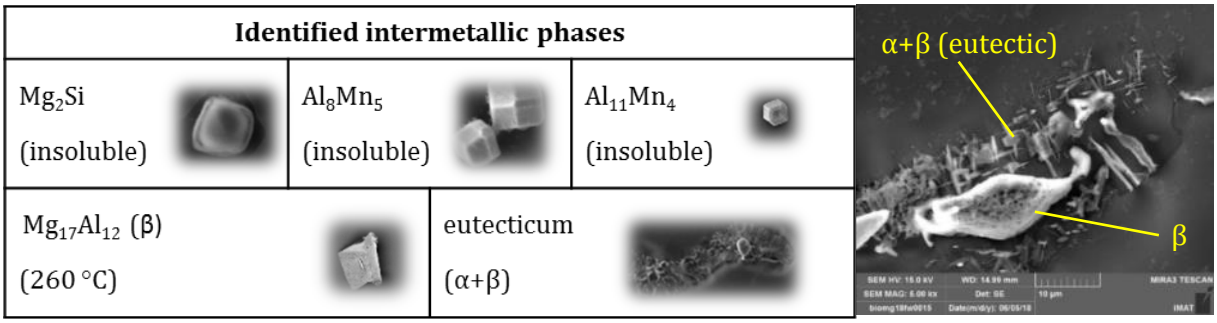

Figure 19: Identified intermetallic phases in the AM50 alloy. Solution temperatures in brackets [54], [55]. *Detail of the $Mg_{17}Al_{12}$ β-phase surrounded by the α+β-eutecticum (right). This eutectic α+β-phase dissolves in the heat treatment.*

4.1.2 ZK40

In a light optical microscopic investigation of the ZK40 base material homogeneously distributed small grains appear (Figure 20). Only at the outer edge of the ingot the structure is finer and grains are about half of the grain size of the centre. A second phase is mainly concentrated at the grain boundaries.

This second phase is identified via EDX as MgZn. The roundish particle in Figure 21 is a precipitate of zirconium. Even though the zinc rich phase is concentrated at the grain boundaries, the matrix contains up to 5 wt.% zinc.

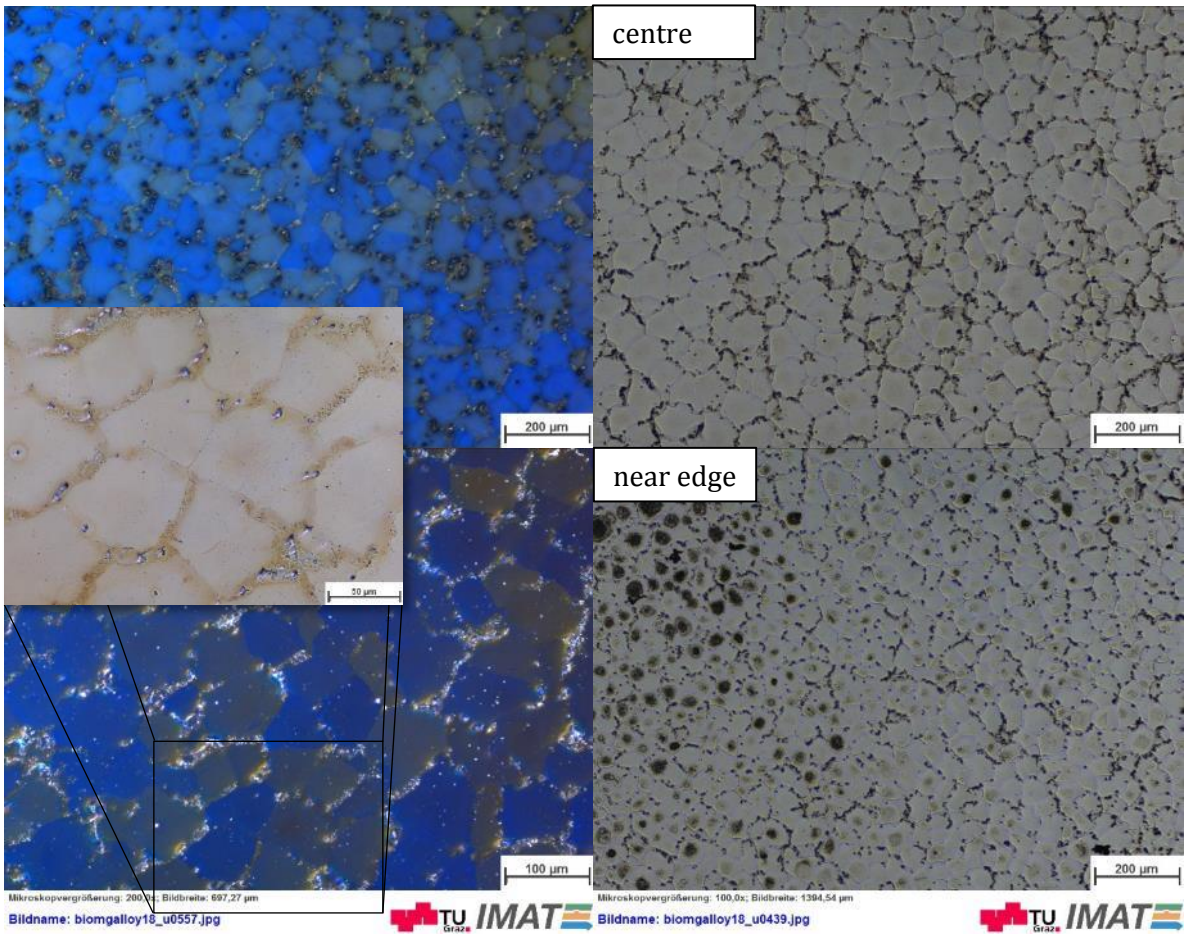

Figure 20: Light optical micrographs of the ZK40 alloy in as delivered condition. Left pictures using polarised light. Bottom left structure was taken approx. 5 mm off the edge.

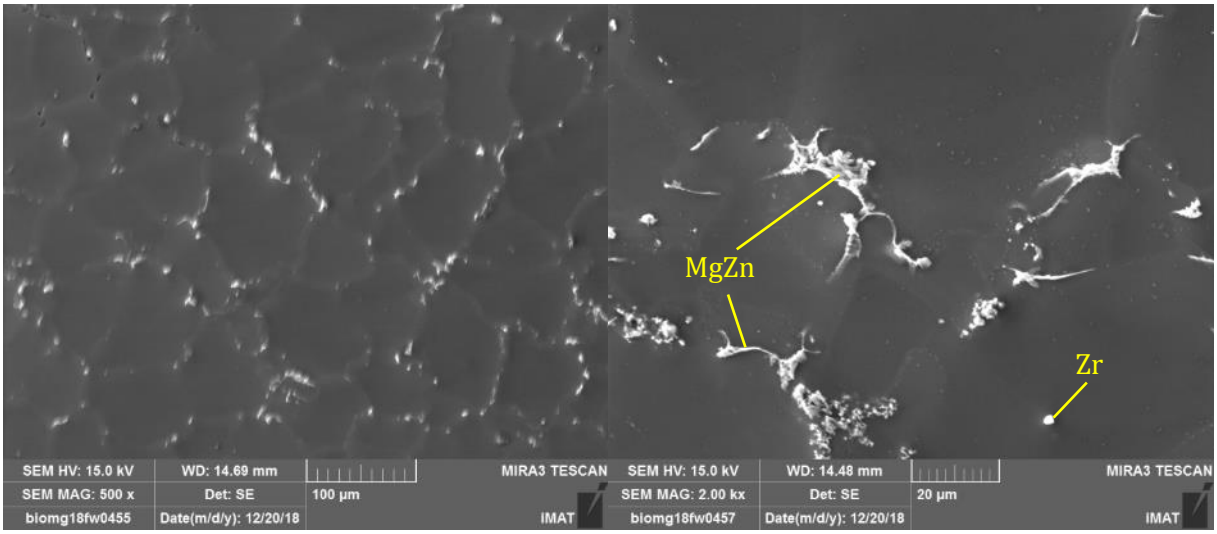

Figure 21: Scanning electron micrographs of the delivered ZK40 alloy. Detail (right) shows the typical MgZn intermetallic phase and a zirconium precipitate.

4.2 Torsion experiments

The temperature measurements of the torsion experiments show, that the heat distributes very homogeneously within the sample. The variances between the different located thermocouples do not exceed 9 °C. Figure 22 shows the curves without larger inaccuracies during the heating step

and the holding step at the lowest temperature and the highest strain rate (250 °C, 1/s). The temperature increases during the deformation, but does not rise more than 10 °C. The increment in temperature for the other experiments is similar or smaller as for the shown example. Large deviations can usually be correlated with the loss of thermocouples during deformations. This can also be observed in Figure 22, where thermocouples 1 and 2 fell off at the end of the deformation, which caused the sudden final increment.

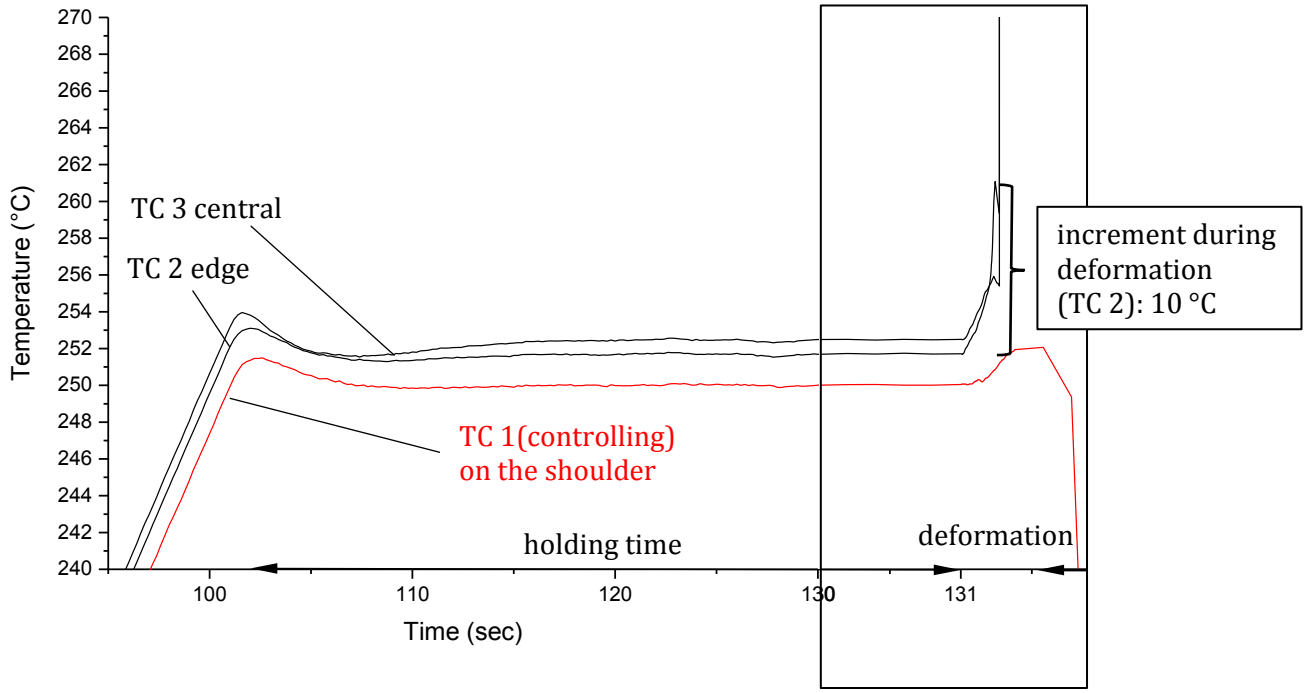

Figure 22: Measured temperatures of the $\dot{\varepsilon}$ = 1/s torsion experiment at 250 °C. The highest signal comes from the thermocouple 3 located in the middle of the sample. The signal of thermocouple 2 (at the sample´s edge) is approximately 3 °C lower. The lowest signal comes from the controlling thermocouple 1 located on the shoulder of the samples. Detail of the deformation showing increments between 3 and 10 °C.

4.2.1 Flow stress

The iterative process of flow curve calculation required three steps to gain stable values of the strain hardening coefficient *n* and the strain rate sensitivity *m*. The final values are listed in Table 8.

Table 8: Exact values after successful iteration for the strain hardening coefficient n and the strain rate sensitivity m of all torsion tests (calculation method described in methodology).

strain rate $\dot{\varepsilon}$	250 °C	300 °C	350 °C	400 °C
1	n = 0.25578 m = 0.06149	n = 0.26971 m = 0.09023	n = 0.28097 m = 0.14156	n = 0.14694 m = 0.17406
0.1	not performed	not performed	n = 0.1816 m = 0.14156	n = 0.13758 m = 0.17406
0.01	n = 0.19426 m = 0.06149	n = 0.1653 m = 0.09023	n = 0.08427 m = 0.14156	n = 0.04765 m = 0.17406
0.001	n = 0.17489 m = 0.06149	n = 0.10349 m = 0.09023	n = 0.00000 m = 0.14156	n = 0.00000 m = 0.17406

The plot of these values in Figure 23 shows that *m* increases with the temperature, whilst *n* decreases. At higher strain rates the hardening coefficient *n* is higher. This effect is less pronounced at 400 °C.

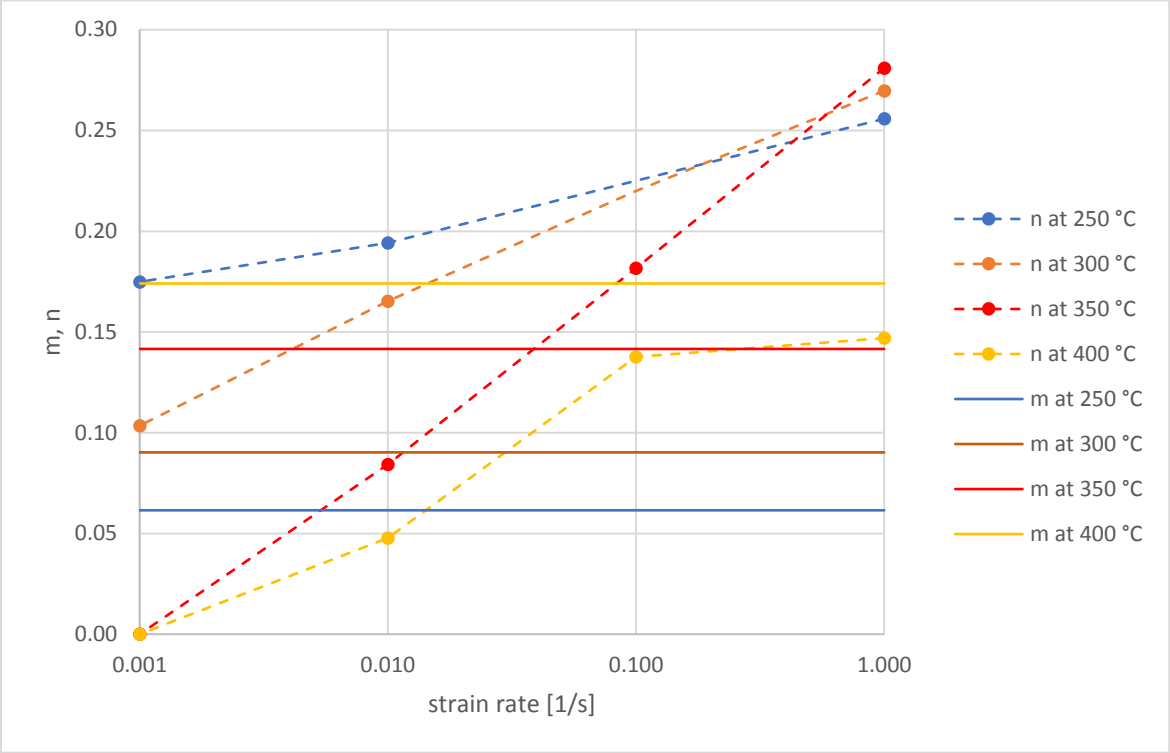

Figure 23: Trends of final strain hardening coefficient n and strain rate sensitivity m of all torsion tests plotted with strain rate and temperature.

Figure 24 demonstrates the flow curves of all carried out torsion experiments. For better lucidity the following graphs (Figure 25) compare the flow curves behaviours for different strain rates at different temperatures.

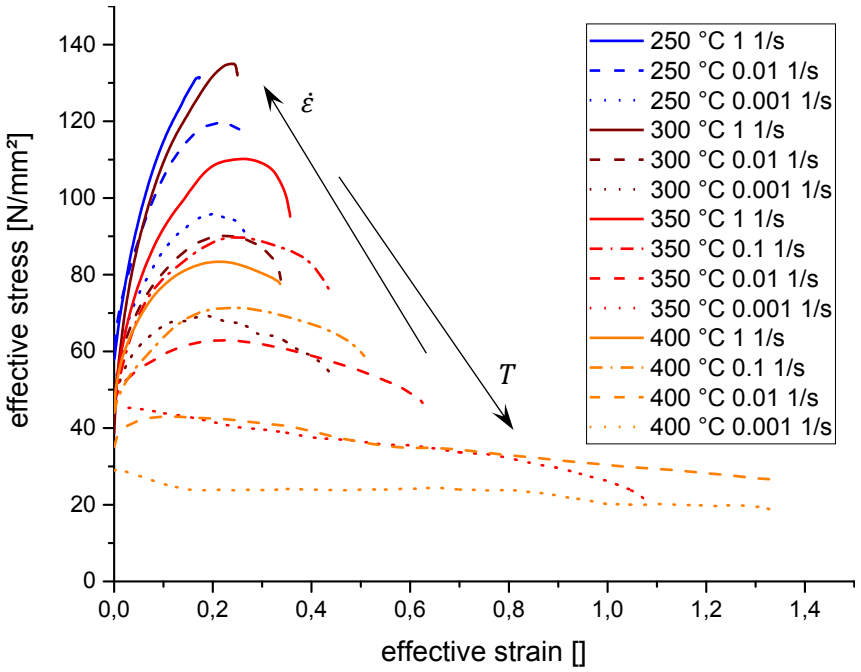

Figure 24: All measured flow curves of the AM50 torsion experiments. Temperature and strain rate strongly affect the characteristics of the graphs.

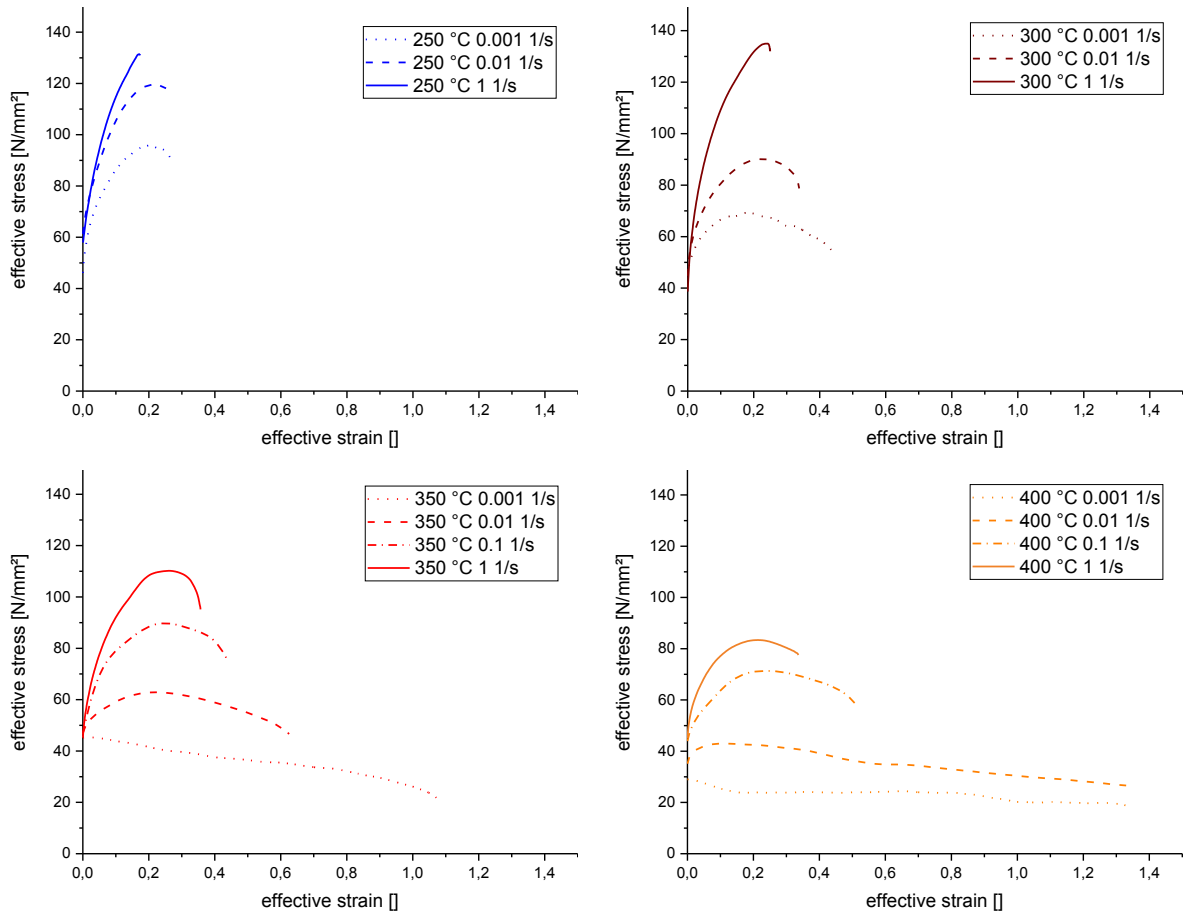

Figure 25: All measured flow curves, comparing the effects of the strain rate at each temperature.

As expected the obtained stresses increase with the strain rates. At low strain rates high strains can be achieved. The yield strengths within the temperatures show good correlations. Also, the repetition of some tests produces flow curves of high similarity. The peak stress rises for high strain rates and low temperatures. For high temperatures (350 and 400 °C) and low strain rates a steady state can be obtained, achieving strains up to 1.3.

4.2.2 Macroscopic investigation

Particularly at low temperatures and high strain rates the samples tended to brake. After large deformations the samples were damaged on their surfaces. Figure 26 shows the damage of a torsion sample after deformation. Due to severe deformation the sample is broken. The surface is rough and many small cracks can be found. The surface layer begins to scale off in certain regions.

Figure 26: Sample deformed at 400 °C with $\dot{\varepsilon}$ = 0.001/s. Crack and surface damage.

4.2.3 Microstructure

The strains in the torsion sample depend on its radius. Thus, the microstructure of one sample always contains effects of different strains. Figure 27 shows a cross section of a wound sample and the enlarged microstructure in the typically analysed areas after a deformation with 300 °C and 0.1/s. At the edge the deformation is clearly visible by grains of varying size and the occurance of twins. In the sample´s centre the strain should be approximately zero. Hoewever, a change of the initial microstructure can be found and twins show up.

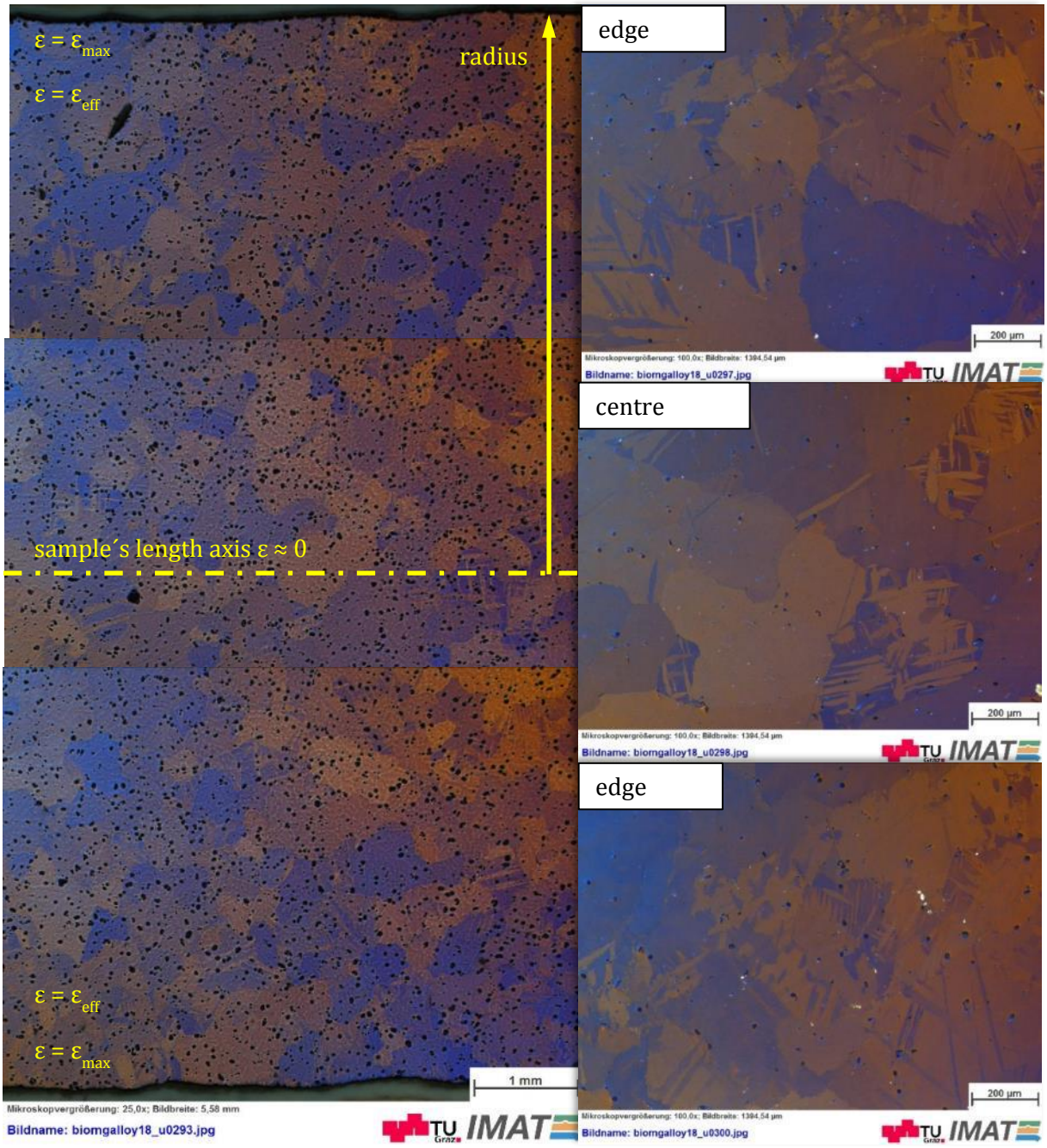

Figure 27: Microstructure through the cross section of the 300 °C 0.1/s sample using polarised light showing details from different radii.

The following light optical images (Figure 28 to Figure 31) demonstrate the evolution of the microstructure at different temperatures. They show for each set of parameters an area of large deformation, where the strains correspond to the effective values (near to the surface), and an area from the low deformed centre. The noted strains give an impression on the possible development of recrystallization, which is further developed at low strain rates and high temperatures.

At a low strain rate (0.001/s) deformation at 250 °C does not stimulate a clearly visible formation of new grains. The sample contains twins over the whole cross section. At 300 °C the original grains still contain twins, but locally very small grains appear near to the surface. These small grains are predominant at 350 °C in the larger deformed part of the sample. The features of the microstructure deformed at 400 °C are similar to 350 °C but with larger grain sizes in general.

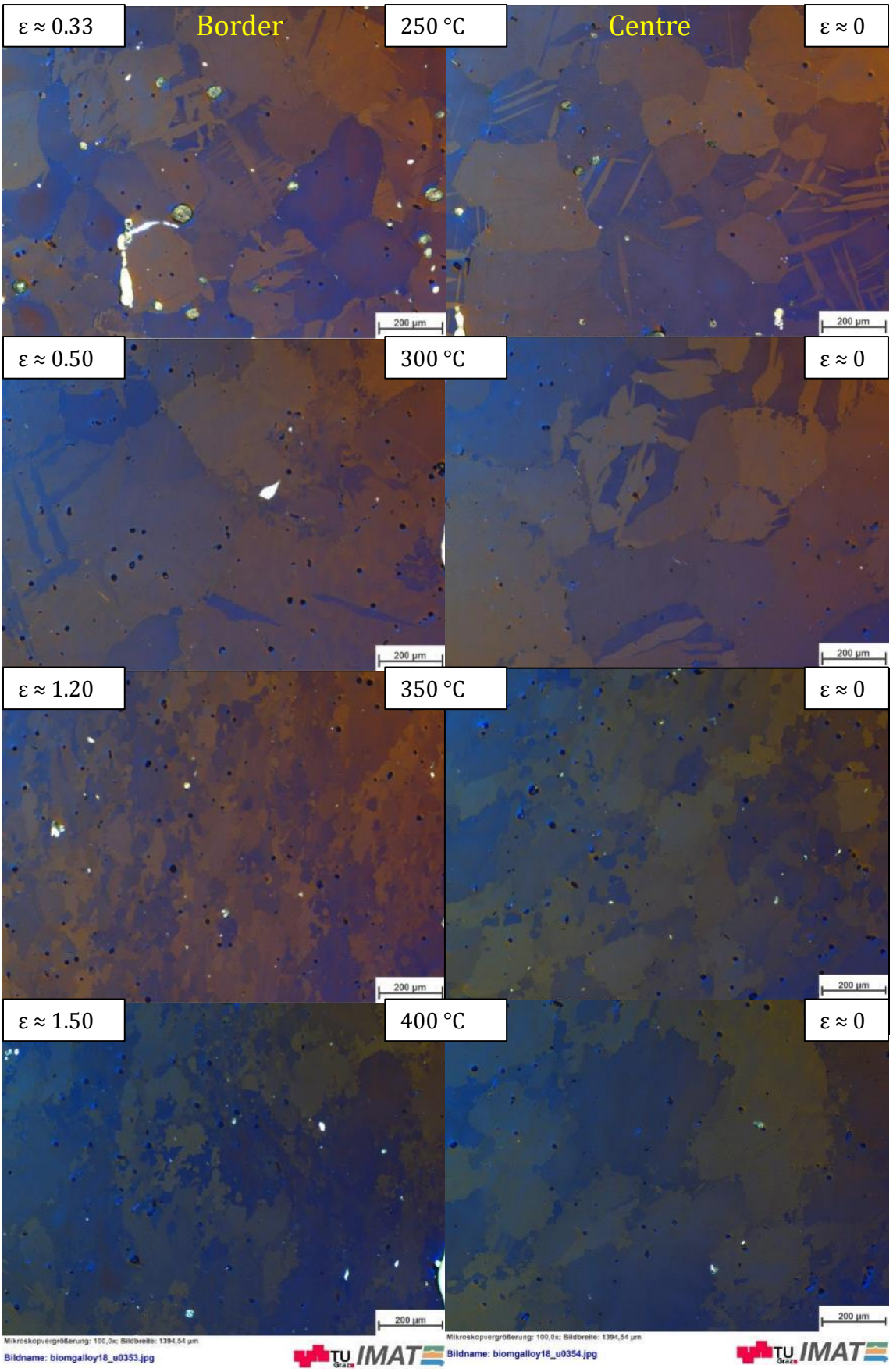

Figure 28: Light optical micrographs of the torsion samples wound with $\dot{\varepsilon}$ = 0.001/s. The left hand pictures show the microstructure near to the samples surface, the right ones are taken in the centre of the samples.

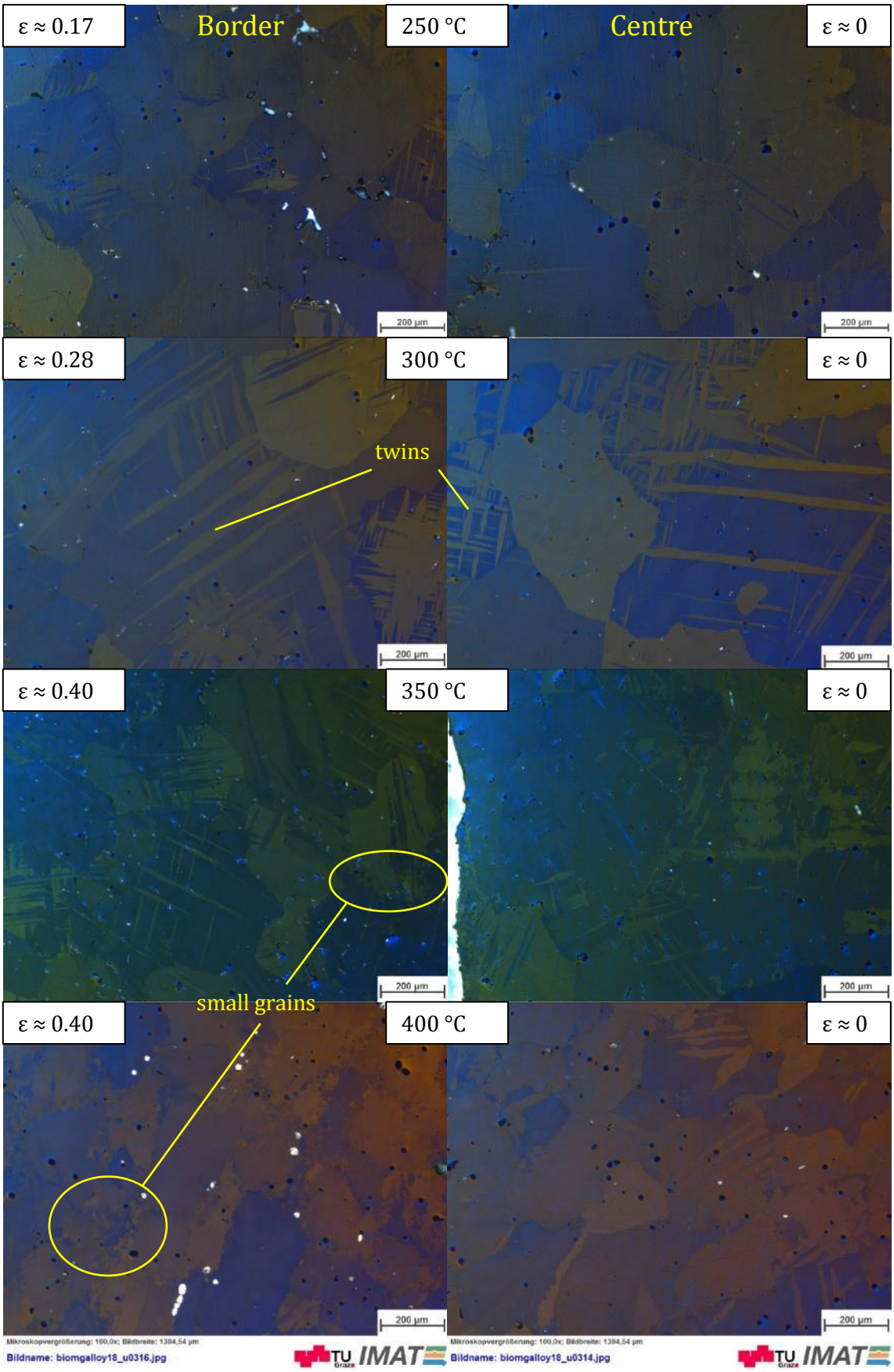

Figure 29: Light optical micrographs of the torsion samples wound with $\dot{\varepsilon}$ = 1/s. The left hand pictures show the microstructure near to the samples surface, the right ones are taken in the centre of the samples.

After fast deformation with a strain rate of $\dot{\varepsilon}$ = 1/s twins appear in every sample (Figure 29). These appear within one grain also in different directions, which is especially pronounced at deformations at 300 and 350 °C. At 350 and 400 °C also very small grains exist in the samples, though their occurrence is limited only to small areas.

Figure 30 a) and b) show the development of the microstructure during progressive deformation. a) displays the microstructure after ε = 1.4 at 400 °C and $\dot{\varepsilon}$ = 0.01 1/s. Small grains fill most of the surface in contrast to b) after ε = 0.23 at the same conditions. Twin effects can have a similar appearance, as visible in d). c) shows the structure in an undeformed area at the shoulder of sample a).

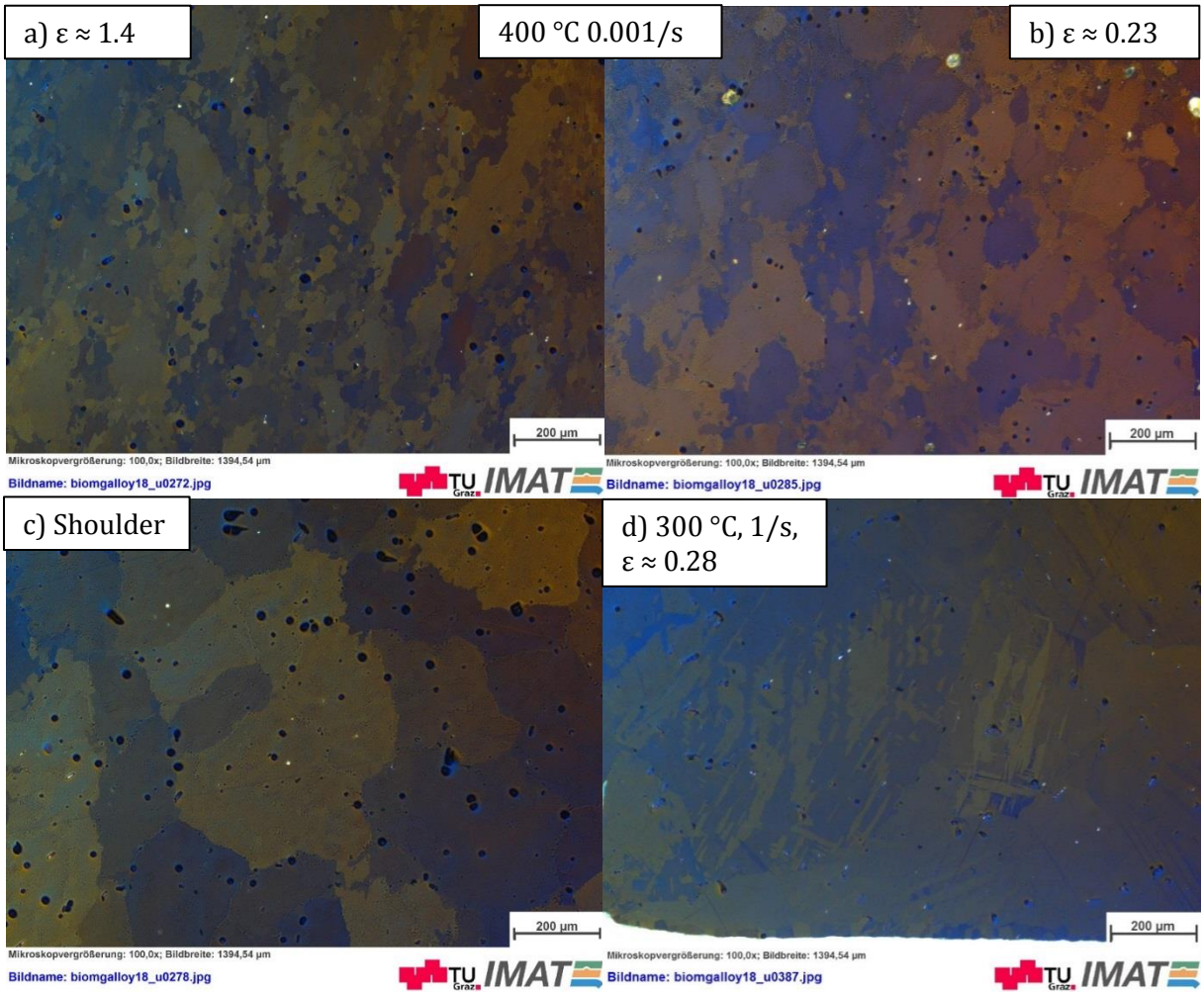

Figure 30: Microstructural features under polarised light: a) Sample deformed at 400 °C with $\dot{\varepsilon}$ = 0.01/s. Microstructure near the surface after ε ≈ 1.4. b) After ε ≈ 0.23 at the conditions of (a). c) Undeformed microstructure at the shoulder of sample (a), d) Twins near the surface after a 300 °C 1/s deformation (ε = 0.28).

A comparison within one temperature (350 °C, Figure 31) over the strain rates shows, that twins develop only at the highest strain rate of 1/s. Even though small grains occur at every strain rate, their amount is locally restricted at 1 and 0.1/s strain rate. Their amount seems to grow only for slow deformation (0.001/s) , where a larger spreading is observed. In any case, for grains of such small sizes an accurate determination of their dimension cannot be expected using polarised light.

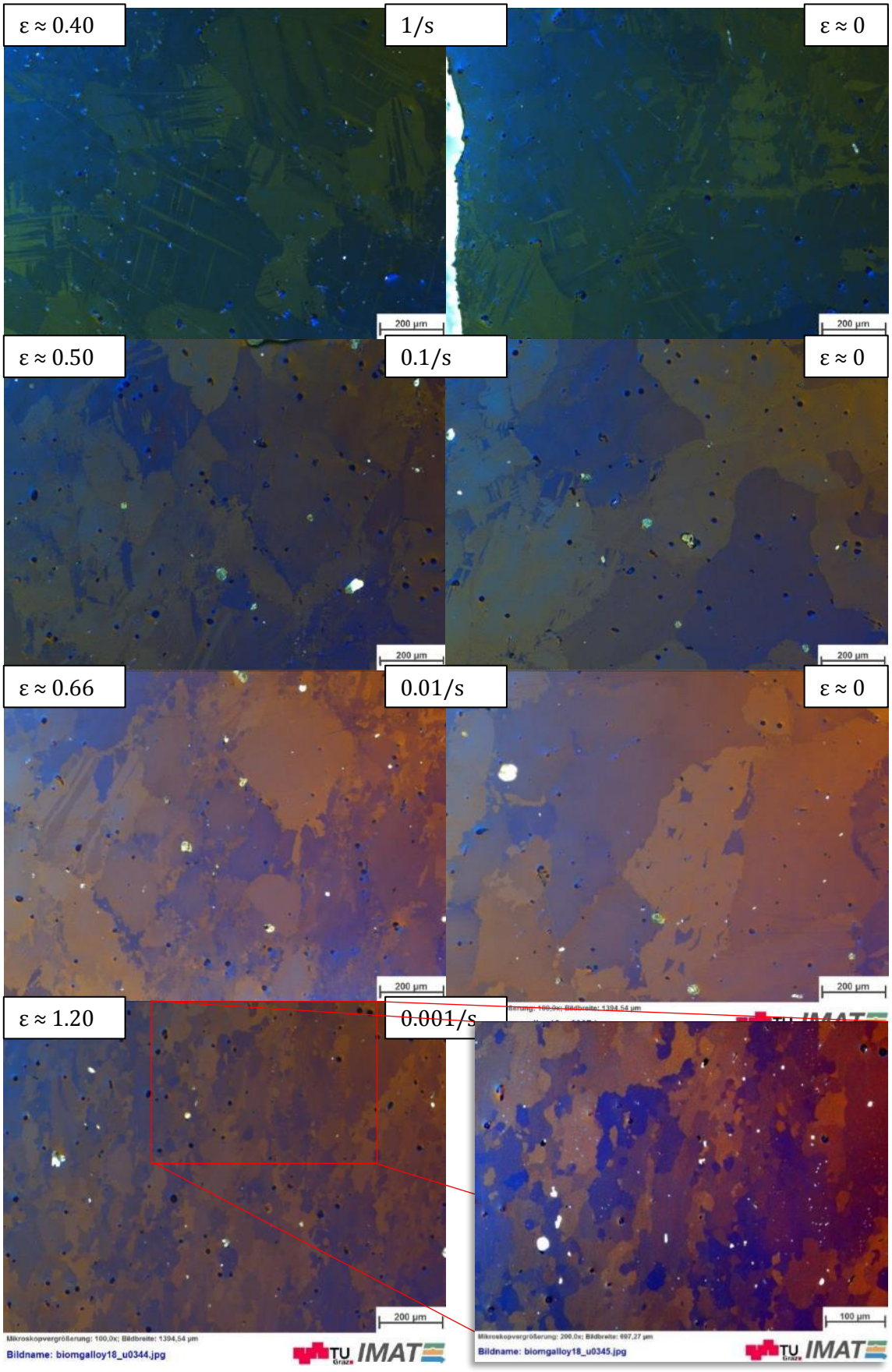

Figure 31: Light optical micrographs of the torsion samples wound at 350 °C with different strain rates. The left hand pictures show the microstructure near to the samples surface, the right ones are taken in the centre of the samples.

On the following pages the microstructural development by torsion with $\dot{\varepsilon}$ = 0.001/s and 1/s is depicted (Figure 33 to Figure 36 and Figure 38 to Figure 39). The electron backscattered diffraction measurements show a segment of the microstructure near to the sample´s surface. The pictures bottoms are taken approximately 300 µm from the edge. This part of the image is closer to the sample`s surface than the top.

The large images on the left hand side (a) are inverse pole figure maps. The four images on the right provide additional information. In the images (b) the grain orientation spread in every grain is represented. In lighter areas the orientation differs more than in the dark zones. In the images (c) the kernel average misorientation maps illustrate, in which amount the neighbouring points differ in their orientation. The bottom pictures are image quality maps containing information about twins (d) and grain boundaries (e). Different types of twins and boundaries are summarized in Figure 32. The Figure also shows the legend for kernel average misorientation and inverse pole figure maps.

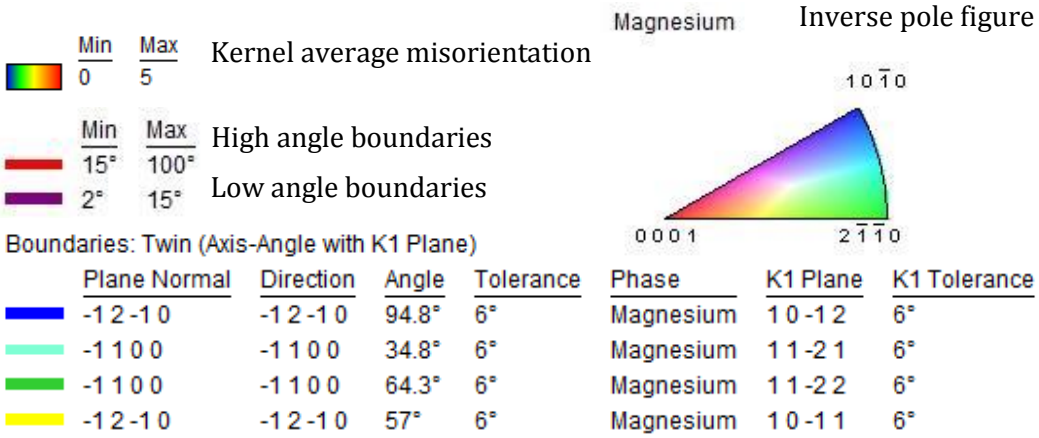

Figure 32: Legend of the EBSD measurements for Figure 33, Figure 34, Figure 35, Figure 36, Figure 38 and Figure 39.

As observed by the light optical microscope, the deformation at 250 °C causes numerous twins (Figure 33 d). These are identified by the software as 94.8° tensile and to smaller extend as 57° compression twins. With similar appearance also low angle grain boundaries occur (e). In contrast to twins, no pronounced change in orientation can be observed along these low angle grain boundaries according to the inverse pole figure maps. In small areas at the grain boundaries small grains occur. Due to the low image quality it is not possible to clearly identify them as recrystallized grains.

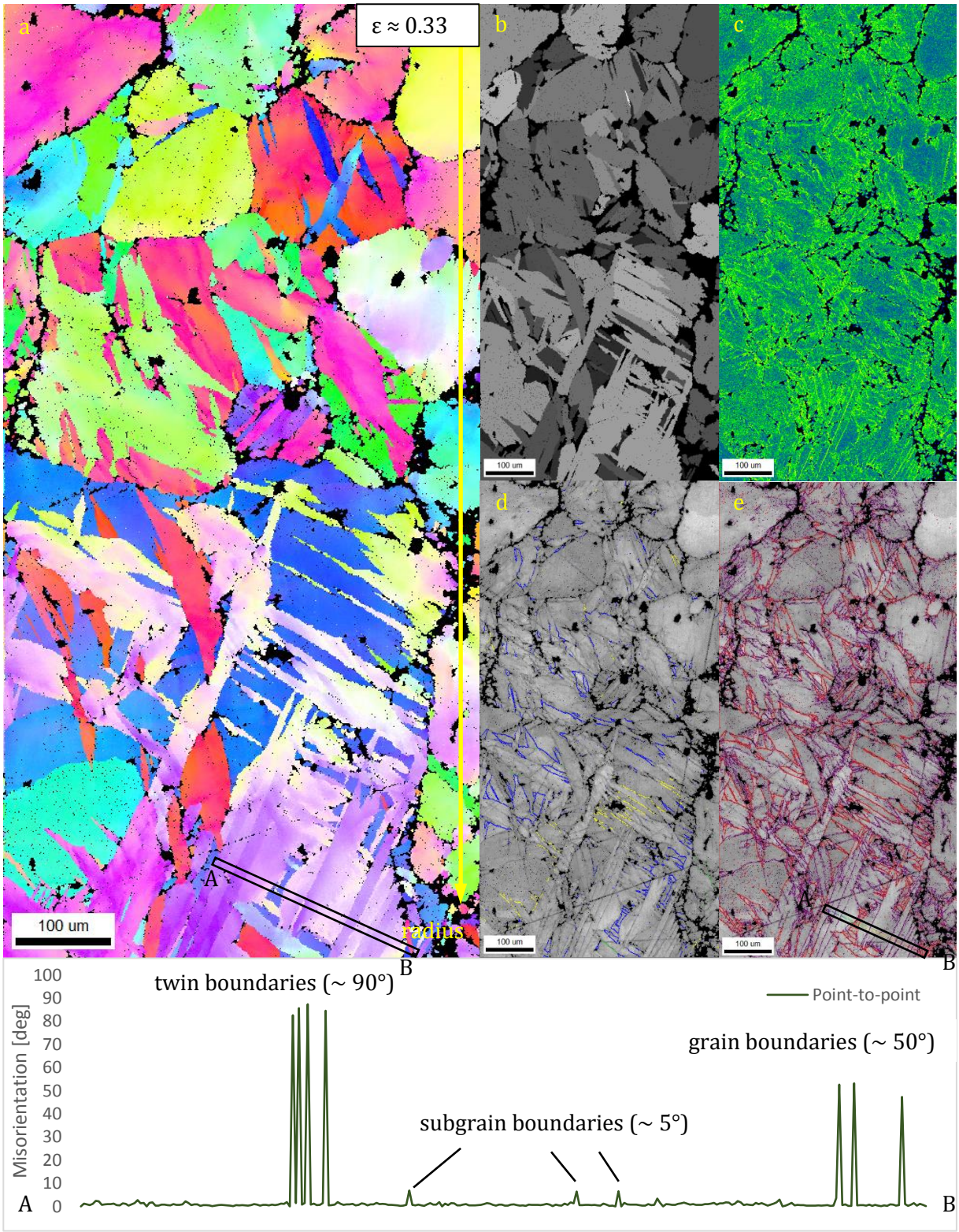

Figure 33: EBSD measurement after deformation at 250 °C with $\dot{\varepsilon}$ = 0.001/s. (a) Inverse pole figure map, (b) grain orientation spread within single grains, (c) kernel average misorientation, (d) twins and (e) grain boundaries in image quality maps. Misorientation profile of the section displayed in (a) and (e). Legend in Figure 32.

Considering the grain orientation spread of Figure 34 (b) after a deformation at 300 °C, the pictures contain grains with very large grain orientation spread, which appear bright, but also very small grains with a very low gradient in their orientation. These are restricted to the grain boundaries, which are mostly formed serrated (g). In few grains singular twins arise.

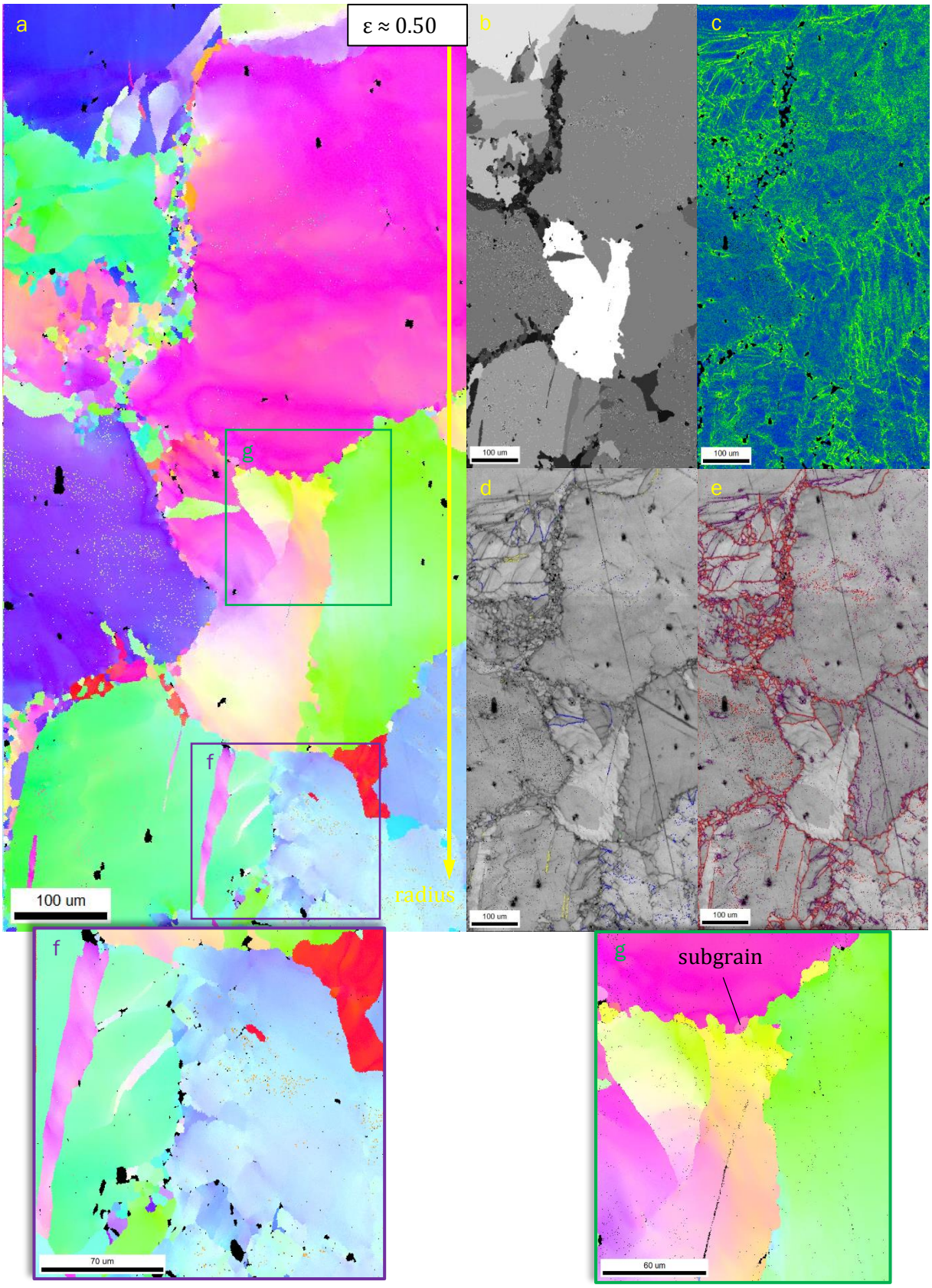

Figure 34: EBSD measurement after deformation at 300 °C with $\dot{\varepsilon}$ = 0.001/s. (a) Inverse pole figure map, (b) grain orientation spread within single grains, (c) kernel average misorientation, (d) twins and (e) grain boundaries in image quality maps. Legend in Figure 32.

At a temperature of 350 °C more of the small grains of low internal misorientation are observed (Figure 35). These are larger than at 300 °C, whilst the grains of high orientation spread are

smaller. The microstructure does not contain a significant amount of twins. The marked boundaries in (d) may also have the specific twinning angle by coincidence.

The graph in Figure 35 shows the misorientation within a large deformed grain from point to point and also compared to the starting orientation (point to origin). The misorientation increases in direction to the centre of the grain and decreases again. Low angle boundaries can be observed as small peaks in the point to point line. Larger peaks are identified as high angle boundaries. An alteration of the point to origin line, which changes back to the former level, is indicated as a twin.

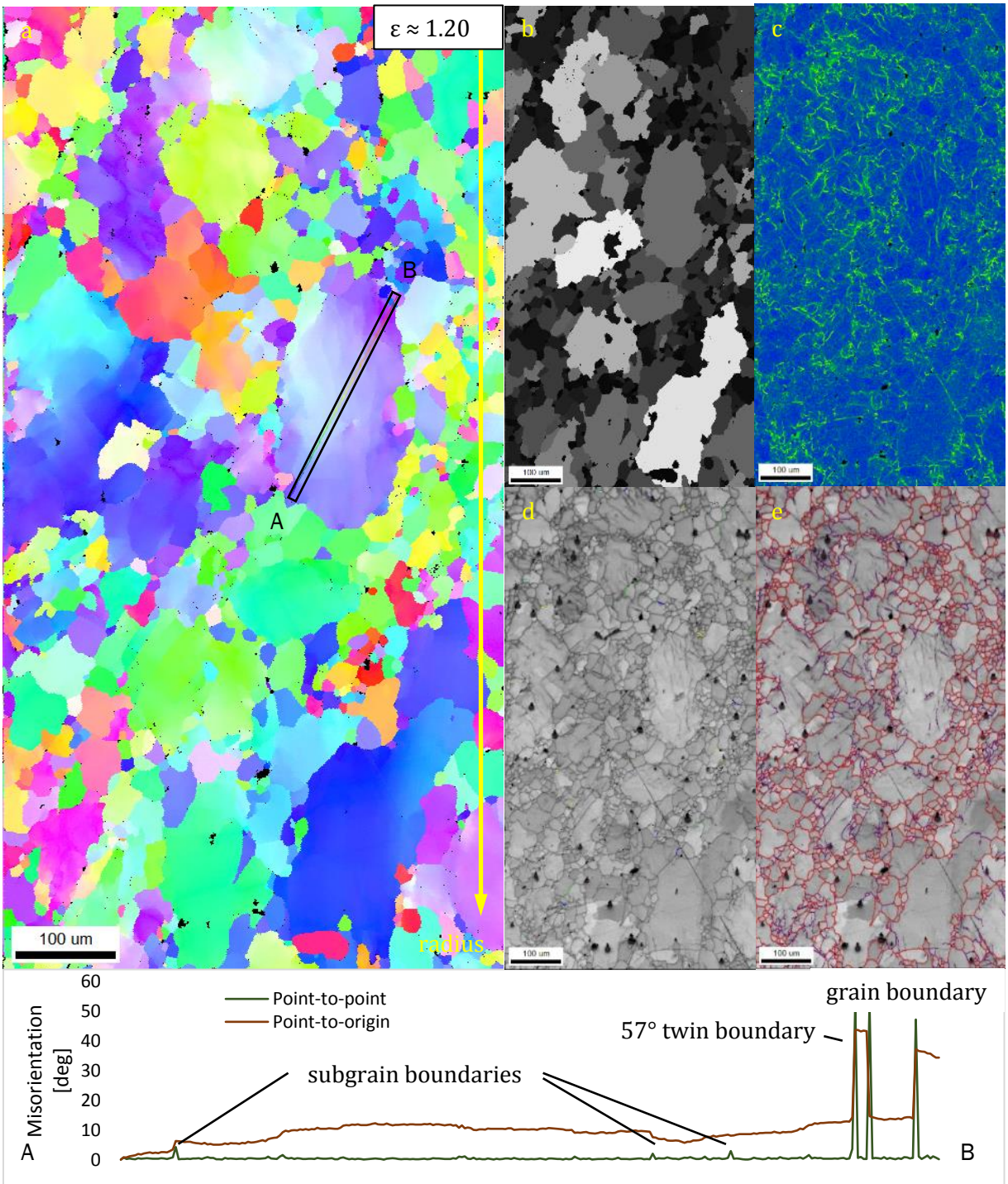

Figure 35: EBSD measurement after deformation at 350 °C with $\dot{\varepsilon}$ = 0.001/s. (a) Inverse pole figure map, (b) grain orientation spread within single grains, (c) kernel average misorientation, (d) twins and (e) grain boundaries in image quality maps. Legend in Figure 32. Misorientation profile of the line in the central large violet grain of the inverse pole figure.

Most of the microstructure of the sample deformed at 400 °C consists of small new-build grains (Figure 36). In between also large grains occur. These have remained in the sample during the deformation and have a large grain orientation spread. Within them no twins can be found. The few indicated twin boundaries in (d) show no comprehensible correlation.

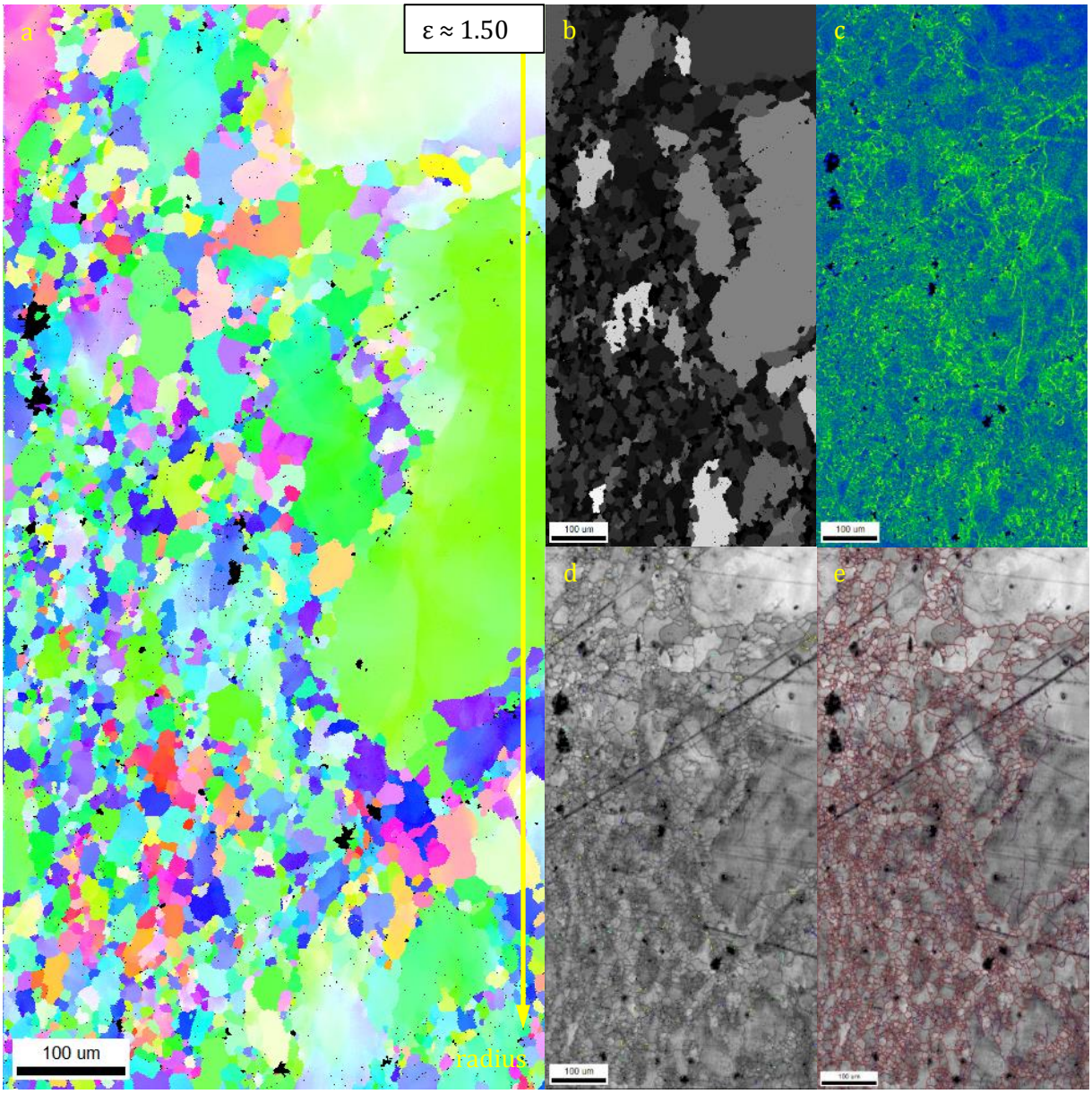

Figure 36: EBSD measurement after deformation at 400 °C with $\dot{\varepsilon}$ = 0.001/s. (a) Inverse pole figure map, (b) grain orientation spread within single grains, (c) kernel average misorientation, (d) twins and (e) grain boundaries in image quality maps. Legend in Figure 32.

In Figure 37 a detail of Figure 36 illustrates the evolution of very small grains, which are examined at a deformation at 400 °C with $\dot{\varepsilon}$ = 0.001/s.

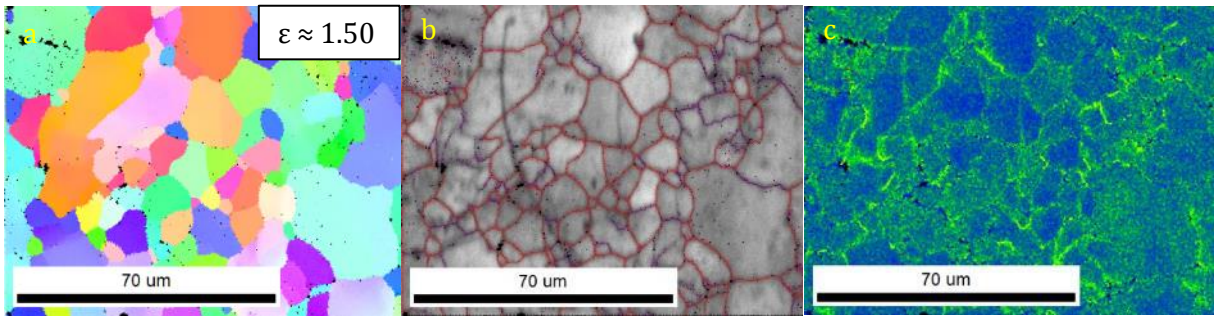

Figure 37: Detail of Figure 36 (T = 400 °C, $\dot{\varepsilon}$ = 0.001/s). (a) Inverse pole figure map, (b) grain boundaries in image quality map, (c) kernel average misorientation. Legend in Figure 32.

In a sample deformed at 400 °C with $\dot{\varepsilon}$ = 1/s, (Figure 38) the development of very fine grains and the evolution of twins, can be observed, too. The fine graines are restricted to the grain boundaries. The twins are wider than twins formed at 250 °C and 0.001/s and show up only in few of the large original grains. The misorientation profile through a severely deformed grain does not contain subgrains as observed at low strain rate (Figure 35), rather a quite smooth behaviour of the point-to-origin line can be observed.

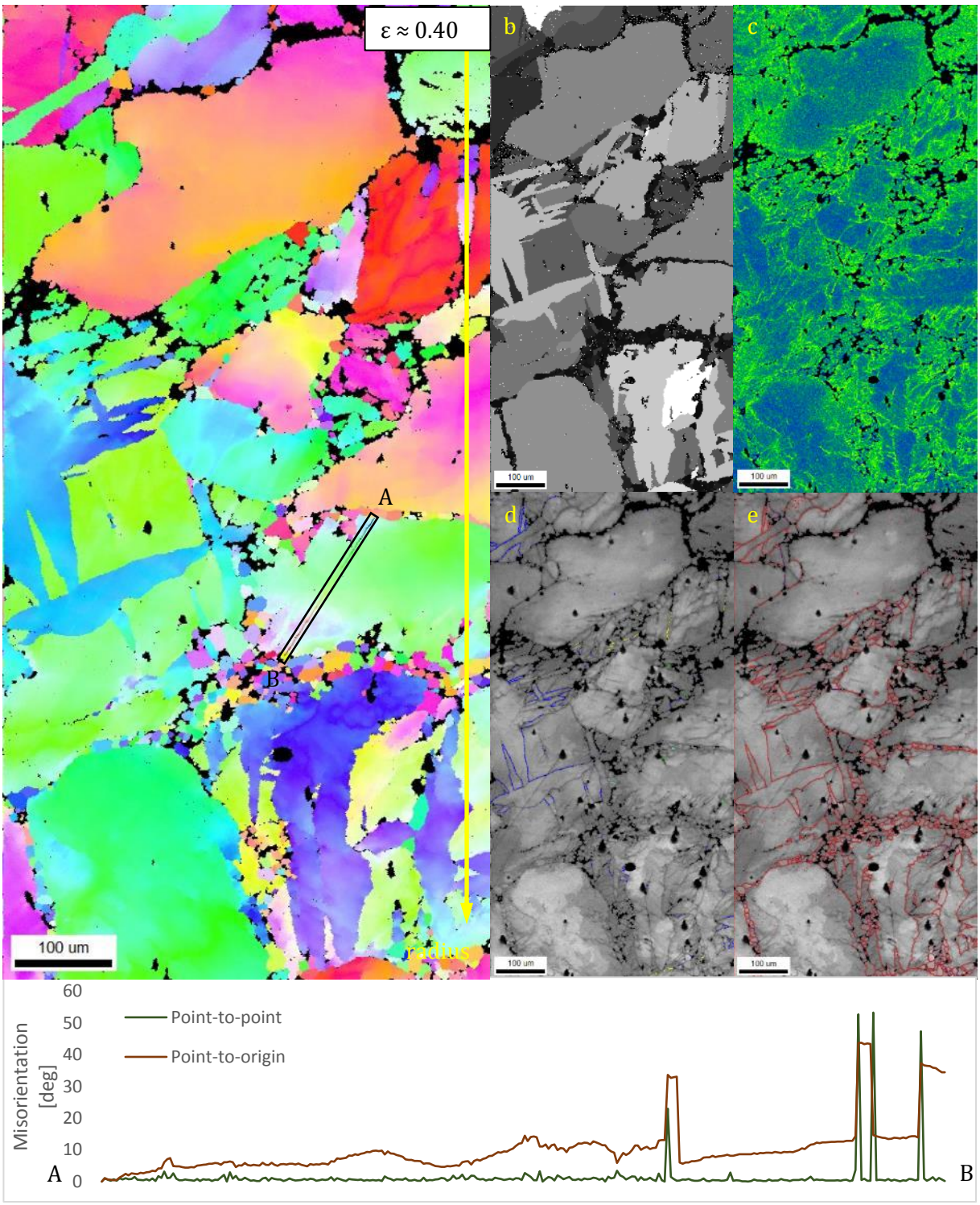

Figure 38: EBSD measurement after deformation at 400 °C with $\dot{\varepsilon}$ = 1/s. (a) Inverse pole figure map, (b) grain orientation spread within single grains, (c) kernel average misorientation, (d) twins and (e) grain boundaries in image quality maps. Misorientation profile of the section displayed in (a). Legend in Figure 32.

After a fast deformation at 250 °C (Figure 39) most of the material has a quite homogeneous grain orientation spread and multiple twinned grains can be found. Like at 400 °C also at 250 °C 94.8° tensile twins are predominant. Some of the twins near to scratches may also originate from this surface damage. In the microstructure no indicators of new-build grains could be observed.

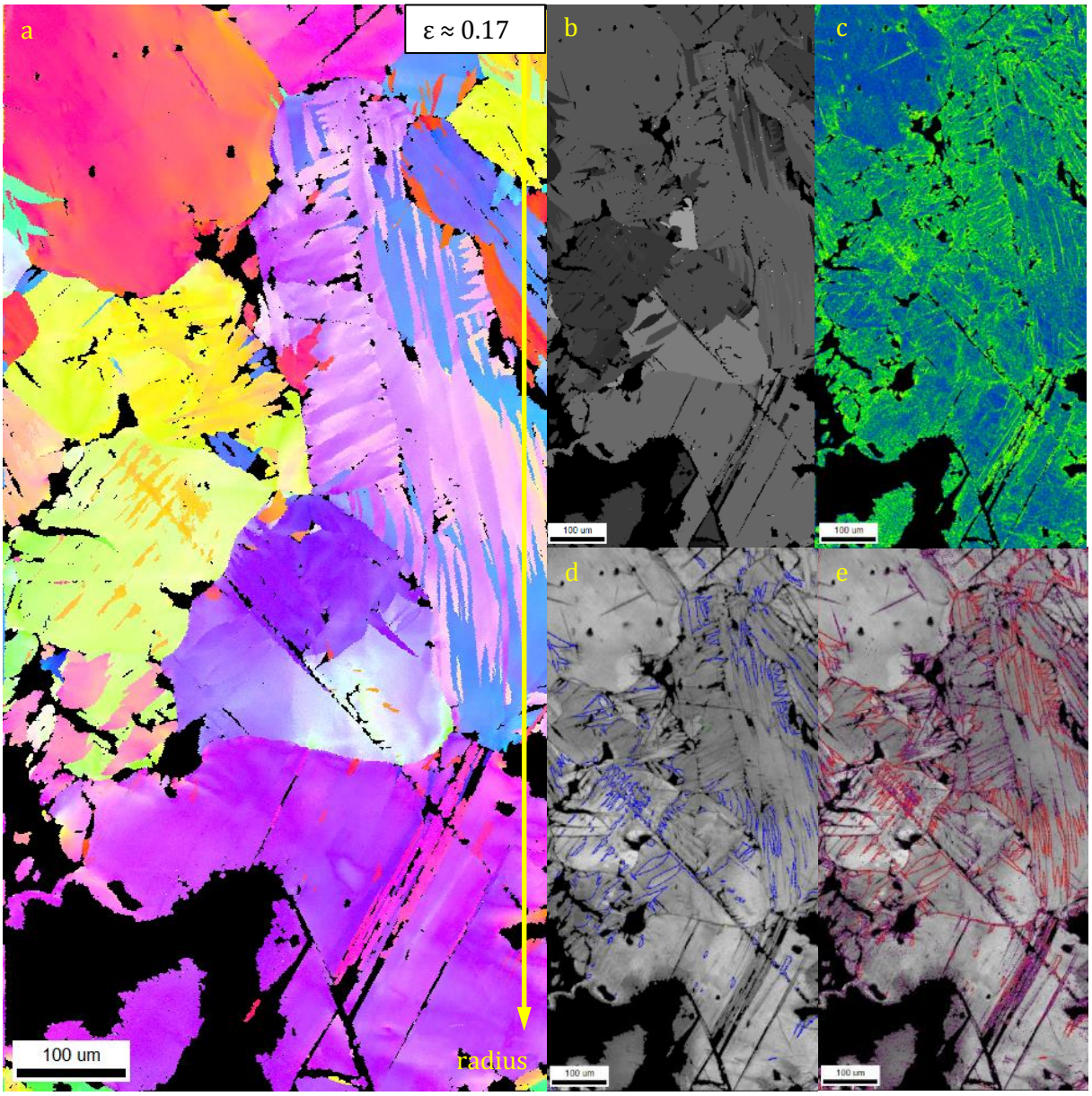

Figure 39: EBSD measurement after deformation at 250 °C with $\dot{\varepsilon}$ = 1/s. (a) Inverse pole figure map, (b) grain orientation spread within single grains, (c) kernel average misorientation, (d) twins and (e) grain boundaries in image quality maps. Legend in Figure 32. Scratches appearing as straight black lines.

4.3 Friction stir processing

4.3.1 Macroscopic examination

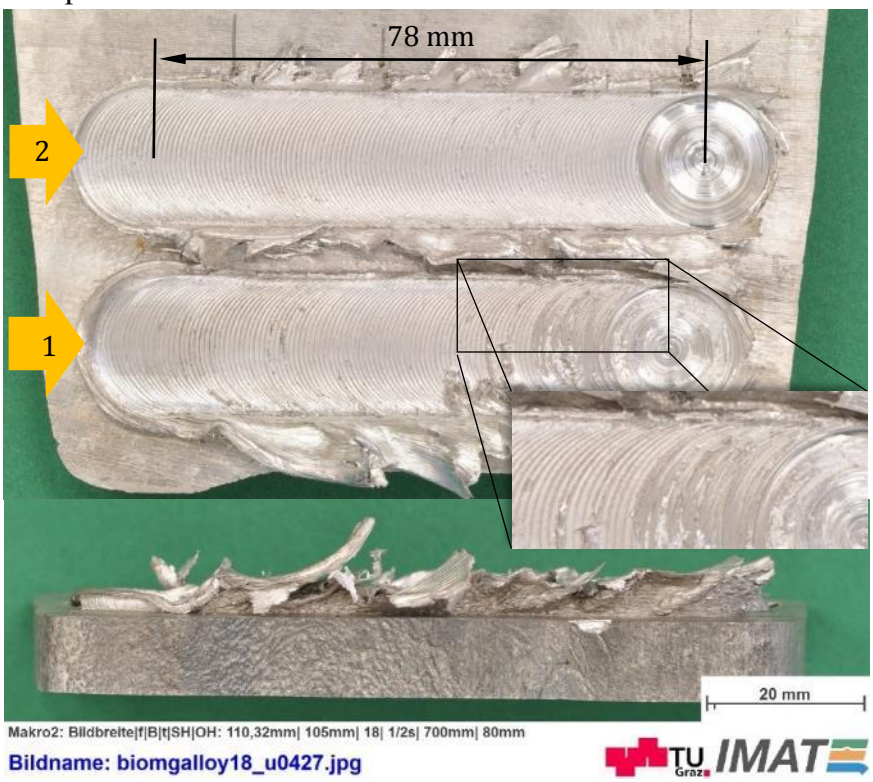

Figure 40: Macroscopic view on friction stir processed AM50.

A macroscopic examination of the friction stir processed material gives a first impression of the success of the procedure. Whilst especially in experiment 1 in the AM50 alloy (Figure 40) some parts of the weld are inhomogeneous, the ZK40 alloy has a very regular surface after the applied process (Figure 41). In both cases thin layers of material stick out several millimetres of the surface at the edge of the stir zone.

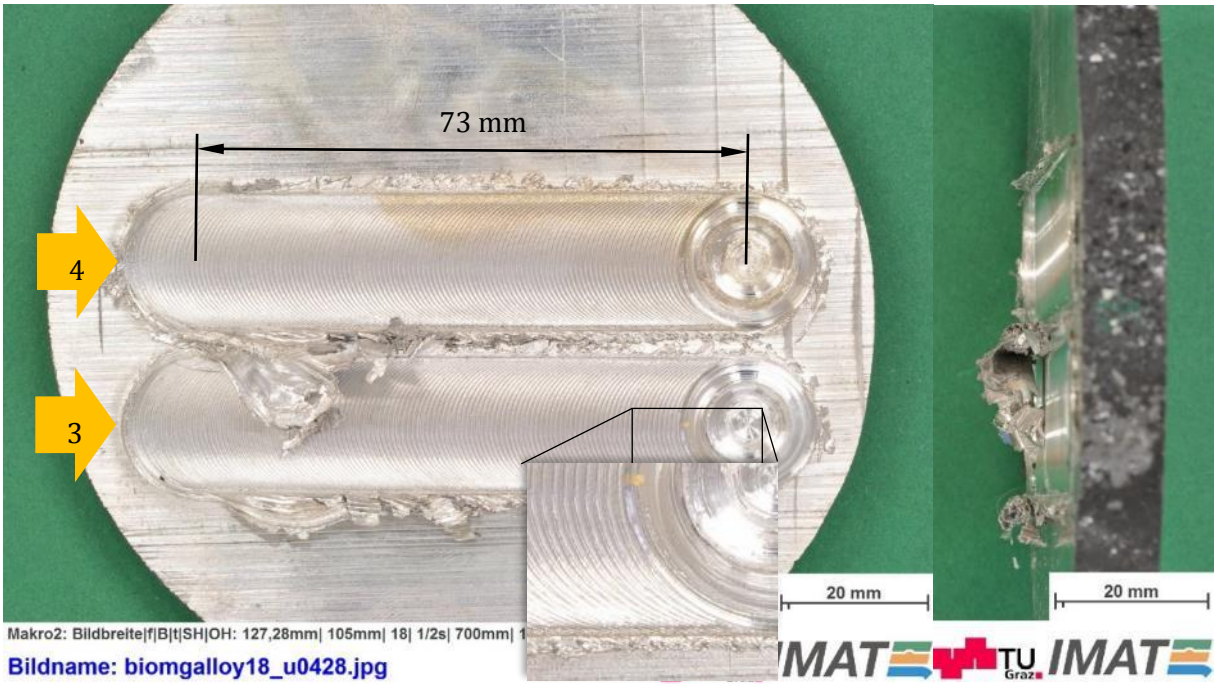

Figure 41: Macroscopic view on the friction stir processed ZK40.

4.3.2 Process data

Figure 42 shows the measured forces and spindle torques of all friction stir experiments. All curves have the feed start as their common starting point of the process. The first signal is the acceleration of the spindle. It is followed by the submersion into the material, during which force and torque fluctuate strongly. This effect stabilises after reaching the complete forge depth. Along with the feed of the tool completely different characteristics occur in AM50 and ZK40. In ZK40 torque and force increase after a short drop rapidly to a very stable and high level. In AM50 the shoulder force falls strongly and fluctuates subsequently. Also, the spindle torque varies significantly. As soon as the feed stops, in all cases the force drops to zero. The torque remains at a low level until the rotation is turned off.

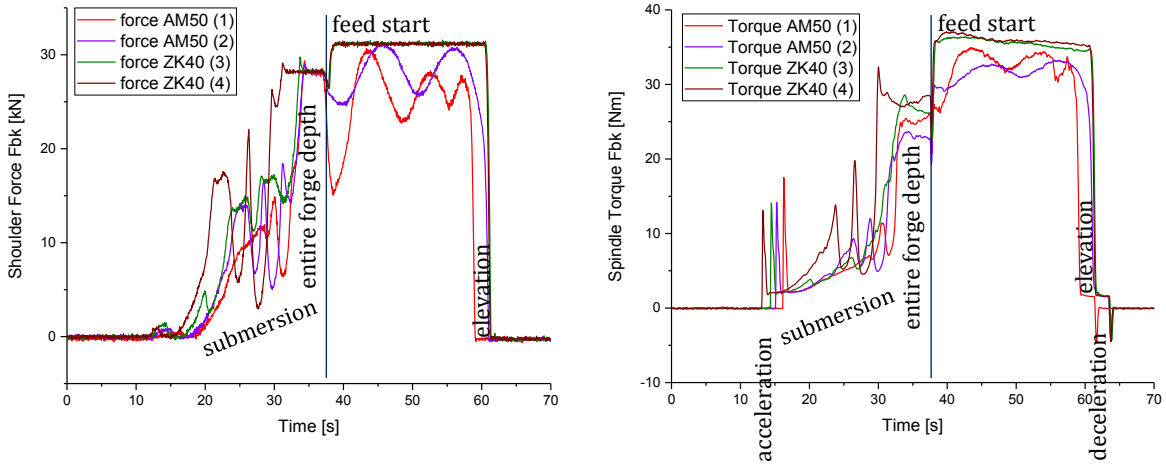

Figure 42: Measurements of shoulder force and spindle torque of all FSP experiments over the time. The two trials with ZK40 (3 & 4) seem more stable than the two AM50 experiments (1 & 2).

The temperature measurements along the weld show good correlations in both AM50 tests (Figure 43). In test 2 the curves of the similar distanced thermocouples 1, 2, 5 and 6 have nearly the same characteristics, only affected by a general heating of the sample. The largest difference occurs in features of the process start measured by thermocouple 1. These can also be observed in test 1. Here thermocouple 6 reaches a comparatively low temperature, caused by its remote position (Figure 12). Thermocouple 7 on the back side of the sample verifies the functionality of the cooling plate. Its maximum temperature is 103 °C. The same thermocouple measures the temperature far away from the weld in test 2. There the samples bottom side reaches a maximum tempertaure of 72 °C. The temperature peaks are very narrow, which ensures, that after passing of the tool the material cools down immediately.

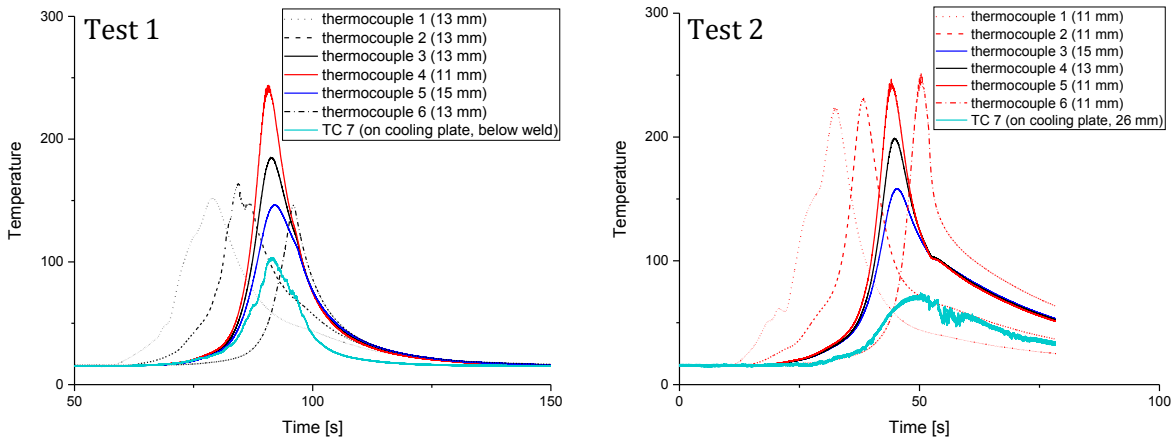

Figure 43: Temperature courses of the AM50 friction stir processes. Thermocouples locations according to Figure 12.

With the values of Table 9 and the formula from section 3.3.1 a welding temperature of approximately 440 °C is calculated (Figure 44).

Table 9: Maximum temperatures of the thermocouples 3, 4 and 5 (Figure 12). These values helped to estimate the welding temperature.

Distance from the centre of the weld	Temperature exp. 1	Temperature exp. 2
11 mm	243,83 °C	246,65 °C
13 mm	185,17 °C	199,08 °C
15 mm	146,52 °C	158,09 °C

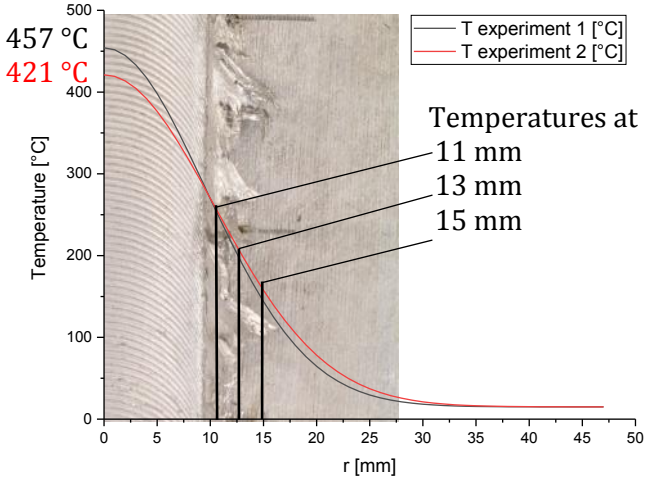

Figure 44: Temperature calculation of AM50 friction stir processes. Position of temperature measurements and exponential fit achieving maximum temperatures of approximately 440 °C.

4.3.3 Microstructure

After polishing of the section through the stirred sample the different characteristics of the stir zone in comparison to the base material are clearly visible macroscopically in both alloys. For each alloy the stir zone reaches approximately 3 mm beneath the surface. In every case left the advancing side is displayed and right the retreating side.

Figure 45 displays a weld in AM50 in its whole width. The interface between the stir zone and the thermomechanically affected zone is suggested, even though not clearly possible to identify.

Intermetallic particles appearing as black dots are homogeneously distributed over the stir zone and the base material in the bottom corners of the figure. At the left hand side, the advancing side contains some roundish pores, whilst in the retreating side at the right hand side, pores are much larger and follow in their shape the contour of the stir zone. In weld 1, which surface is of less quality, also pores within the sample are larger.

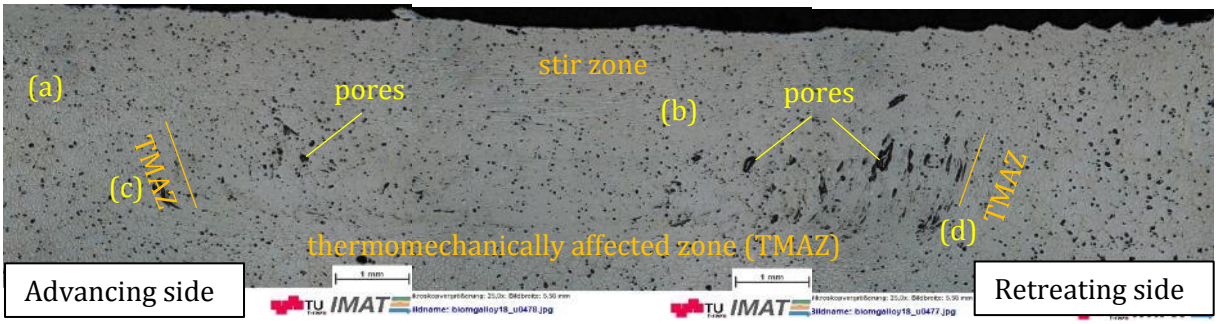

Figure 45: Light microscopic view of the whole stir zone in weld 2 (AM50) at position III. Pores and presumed position of the thermomechanically affected zone. (a), (b), (c) and (d): positions of images of Figure 46.

The microstructure of friction stir processed AM50 is shown in Figure 46. Laterally off the stir zone many narrow twins fill large grains (a). A similar structure can be found below the stir zone. With the light optical microscope the microstructure within the stir zone is not distinguishable. Also, polarised light cannot show grains (b). (c) shows large grains of the base material and a narrow transition zone to the retreating side of the stirred material. In (d) (advancing side) the interface is wide with progressing smaller grains.

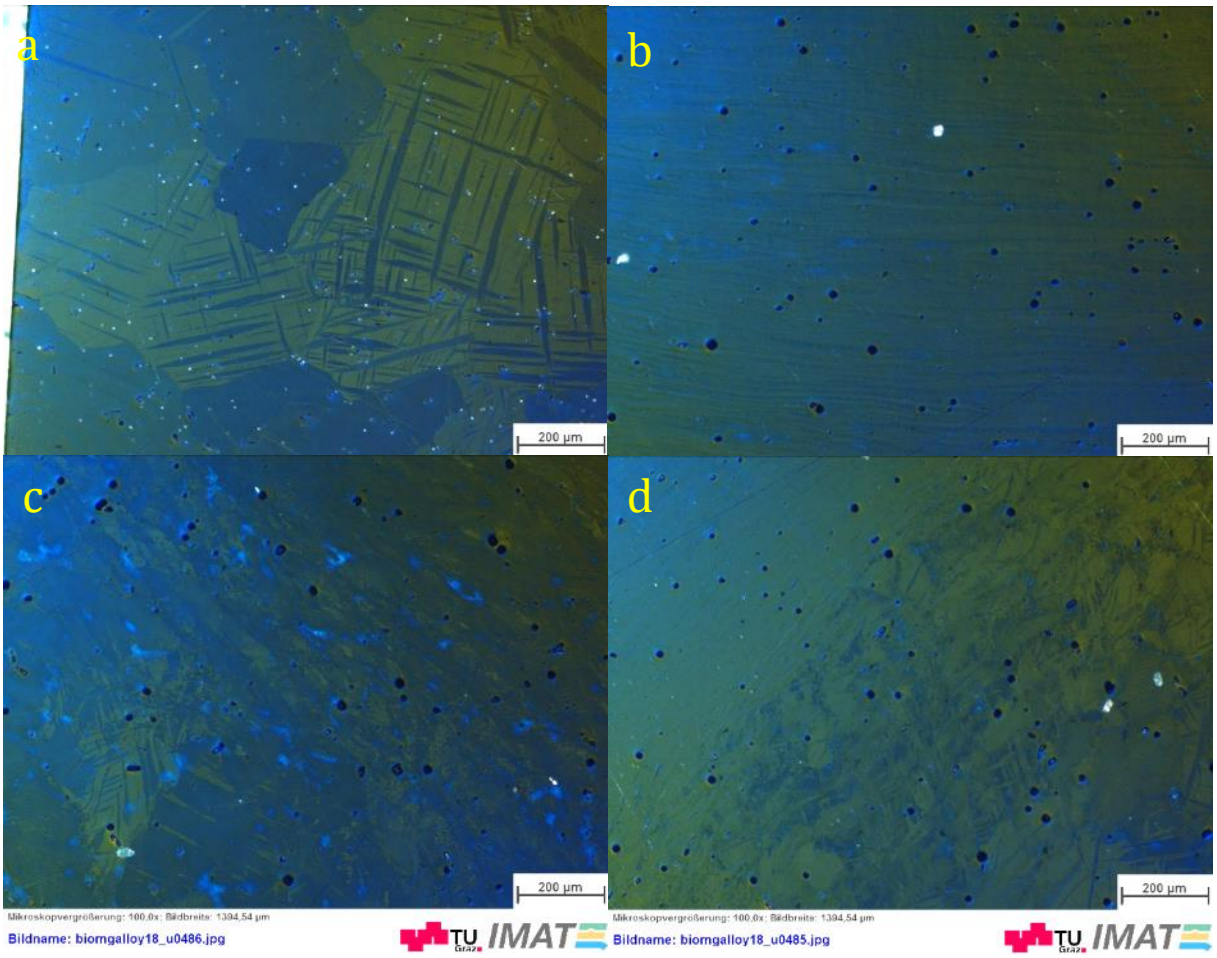

Figure 46: Light microscopic images using polarised light nf AM50 FSP sample 2/III: a) microstructure next to the weld, b) blurry information within the stir zone, c) interface to the advancing side of the stir zone, d) interface to the retreating side of the stir zone. Image positions in Figure 45.

In the weld brighter zones appear resembling a second phase (Figure 47). An energy dispersive X-ray analysis confirms the expectation, that leftovers of aluminium from the cleaning process of the tool were worked into the magnesium alloy during the process.

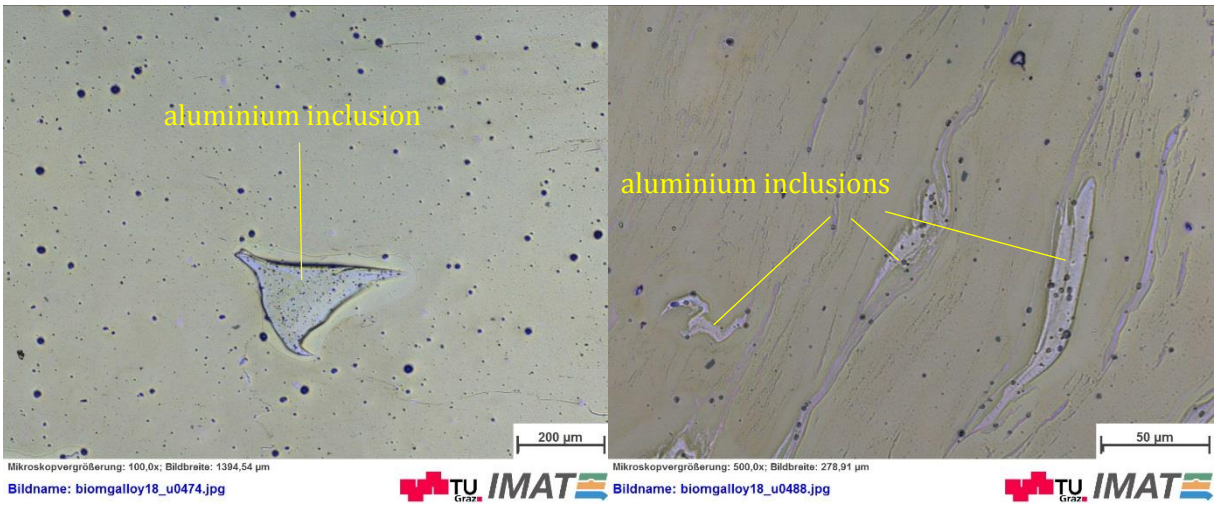

Figure 47: Contamination with aluminium in the middle (left) and at the bottom right (right) of the stir zone in AM50.

Figure 48 shows an EBSD measurement of the stir zone in AM50. Even though the image quality and the confidence indices are quite low, grain sizes between 1 and 5 µm can be estimated.

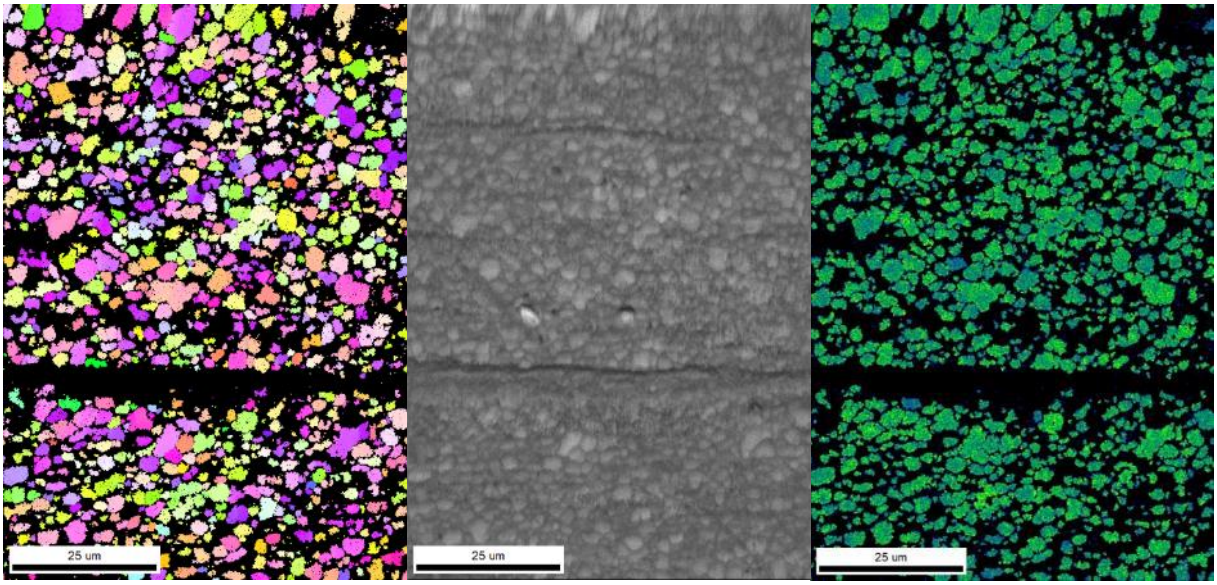

Figure 48: EBSD measurement at the stir zone of AM50.

In the beginning of the welds in ZK40 also pores and aluminium inclusions can be found (Figure 49). With the progress of the process these inhimogeneities dwindle (Figure 50).

As in AM50 the advancing side consists of deformed grains, which become smaller within the stir zone. At the retreating side a clear border separates the stir zone from the base material (Figure 49, Figure 50). This effect is more pronounced in ZK40 than in the AM50 alloy.

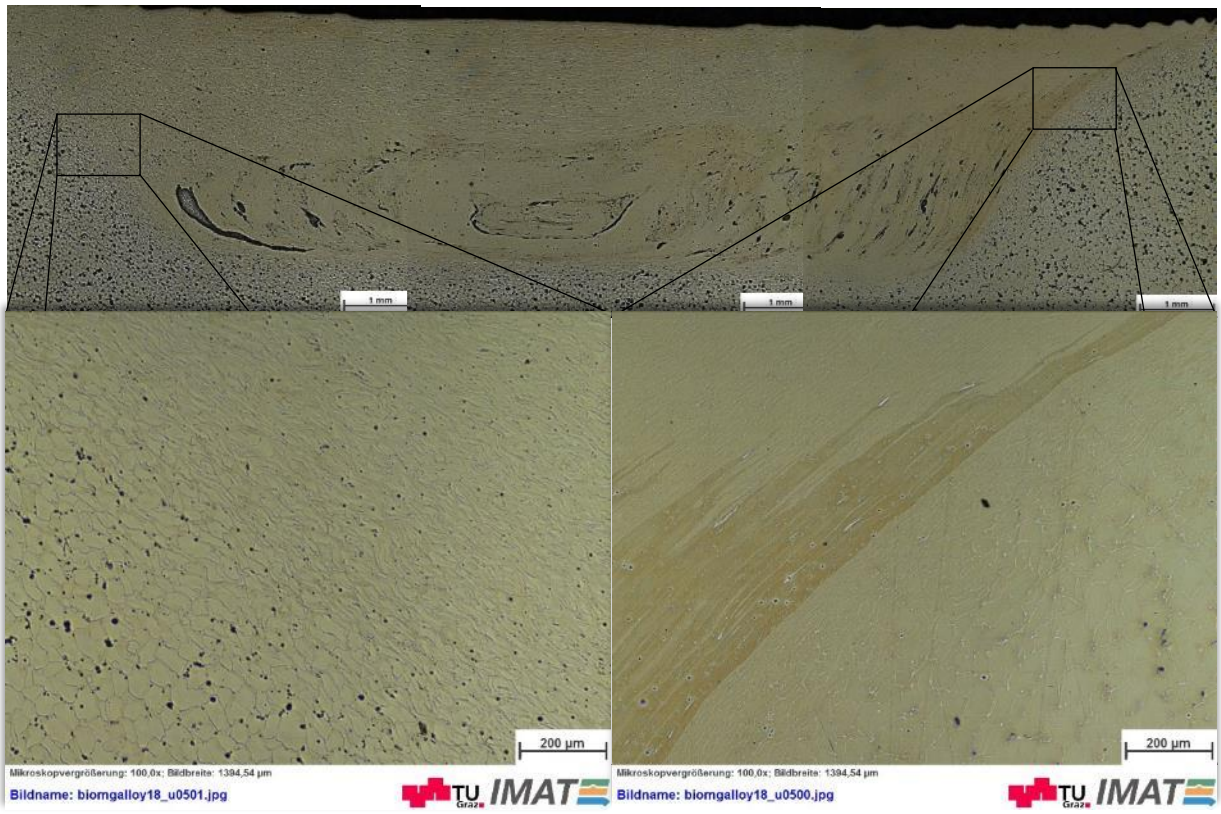

Figure 49: Friction stir processed ZK40. Cross section through weld 3 at position II. Detail of the advancing (left) and the retreating side (right).

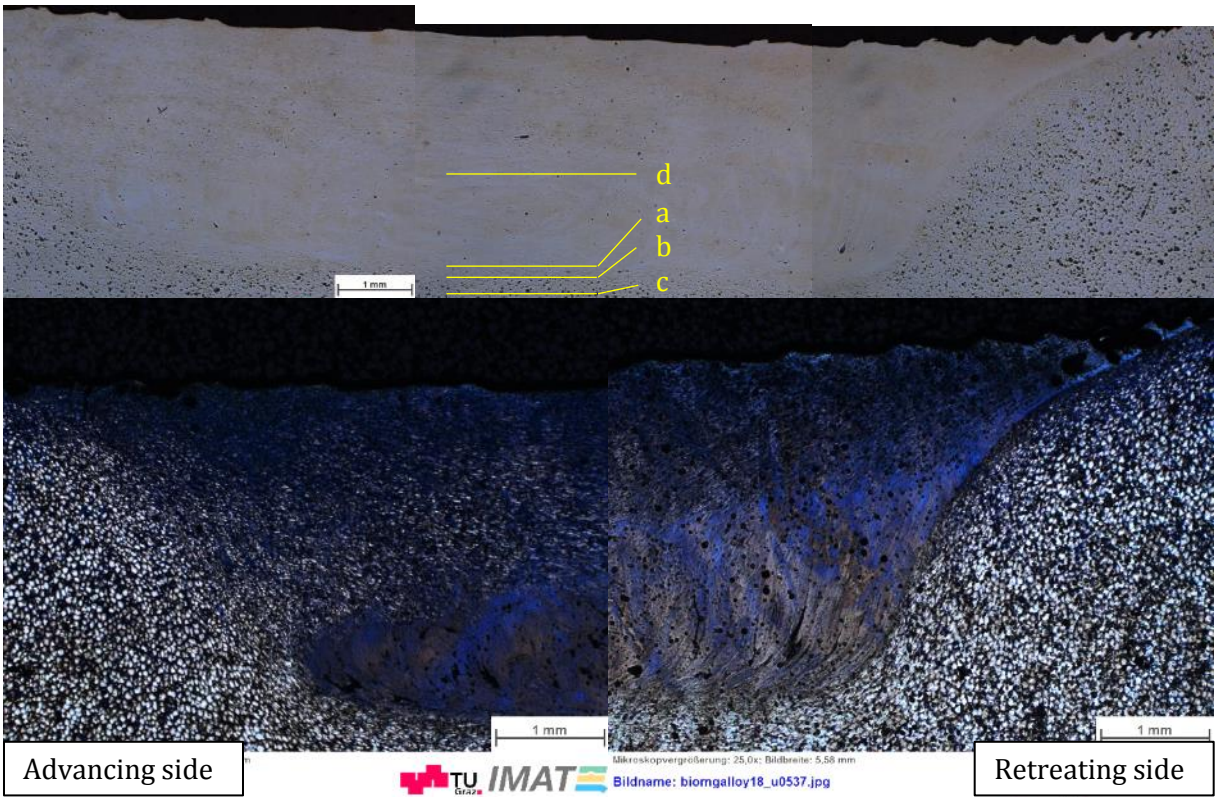

Figure 50: Friction stir processed ZK40. Cross section through weld 3 at position IV. Detail of the advancing (left) and the retreating side (right) using polarised light. (a), (b), (c) and (d): vertical positions of images of Figure 51.

.

Grains at the bottom of the sample are slightly affected by the friction stir process (Figure 51 c), but with polarised light twins appear in most of the grains (e). Closer to the stir zone in the thermomechanically affected zone the grains are elongated (b), more stripes appear progressively at the interface to the stir zone despite of elongated grains (a). These stripes delay any investigation on the grain structure within the stir zone (d) and may also be interpreted as artefacts developing by selective corrosion during sample preparation.

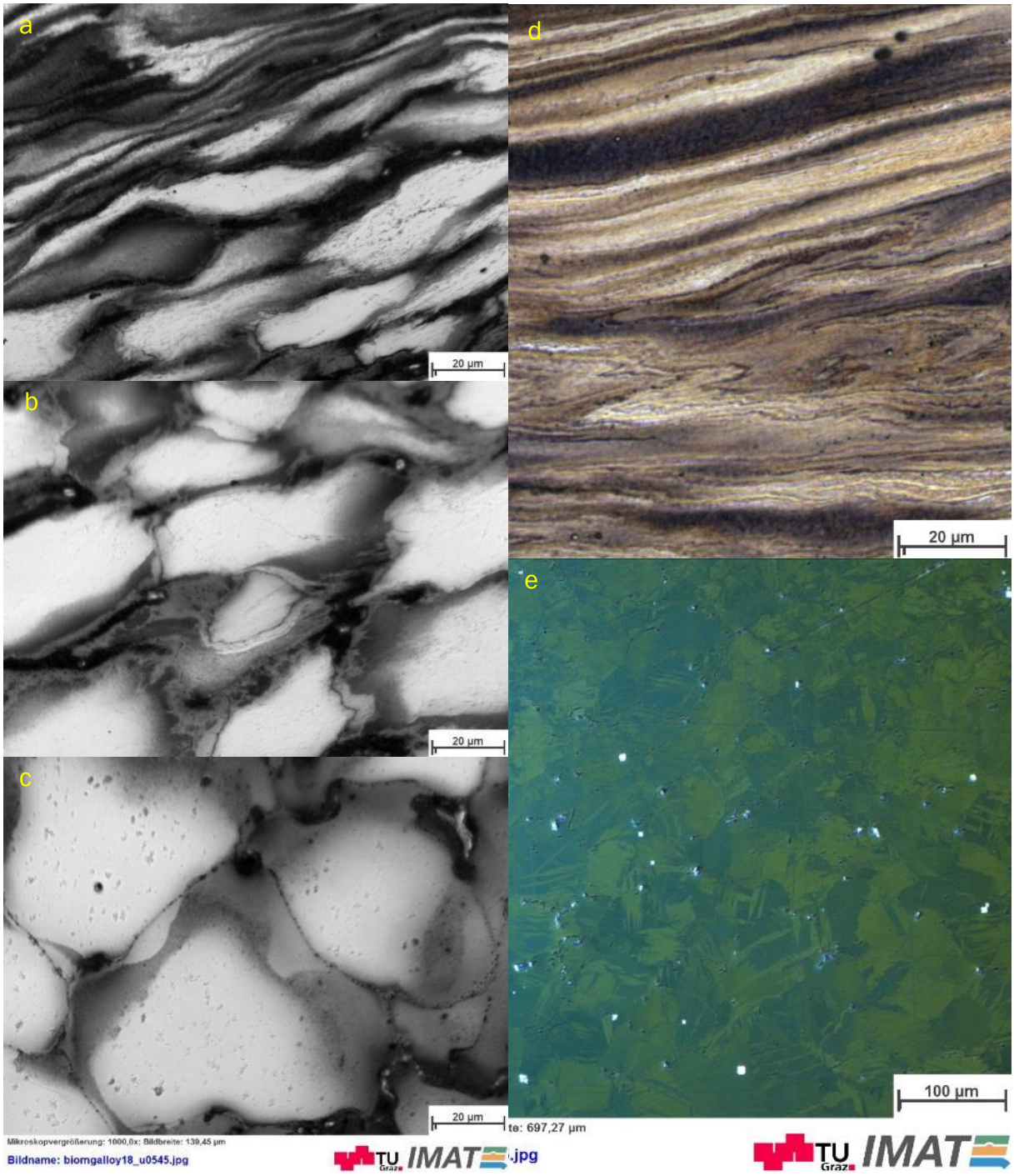

Figure 51: Left: grain structure of the thermomechanically affected zone in weld 3 of ZK40 at position IV, (a) near to the stir zone (c) near to the base material. Right: Detail of the stir zone (d), material below the stir zone near to the samples bottom (e). Image positions (a…d) displayed in Figure 50

At the advancing side a finer structure fills some grains. Unfortunately, these features hardly come into view in the highest possible magnification. Also, the differentiation between artefacts and grains is difficult here, therefore no clear statement is possible.

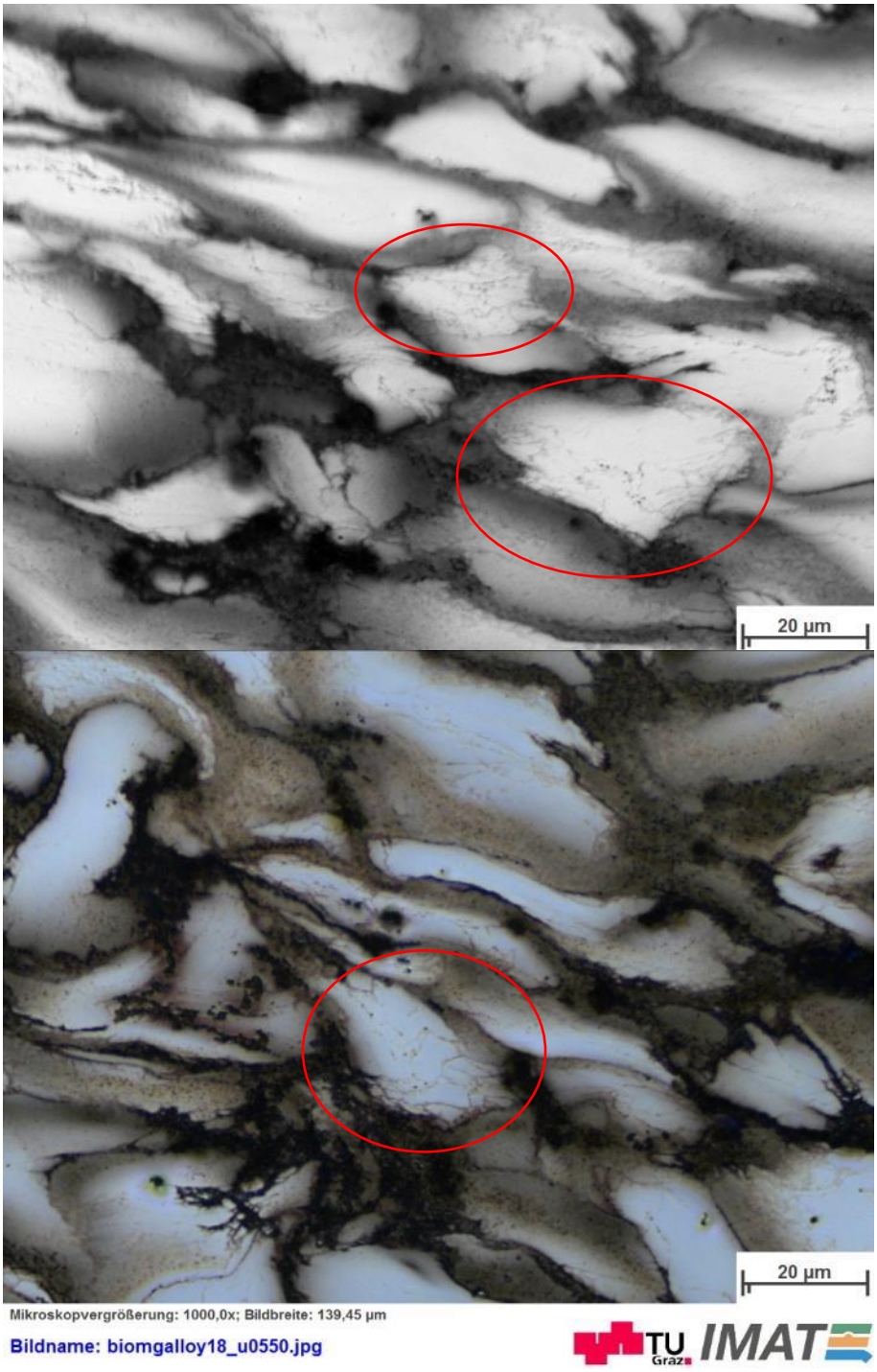

Figure 52: Details of the advancing side of weld 3 at position IV: very fine lines can be found within the grains.

5 Discussion

5.1 Torsion on AM50

The investigation of the base material AM50 shows that larger pores and inhomogeneities occur within the material in the as-delivered condition (Figure 16). These defects can cause deviating flow curves, but can also effect the micrographs. In most cases the results of repeated experiments correlate well, apart from a sample shown in Figure 53. It shows the flow curves of two tests carried out at the same conditions (400 °C, 1/s), of which one achieves unexpected high strains before fracture. This difference may have its origin in heterogeneities of the microstructure.

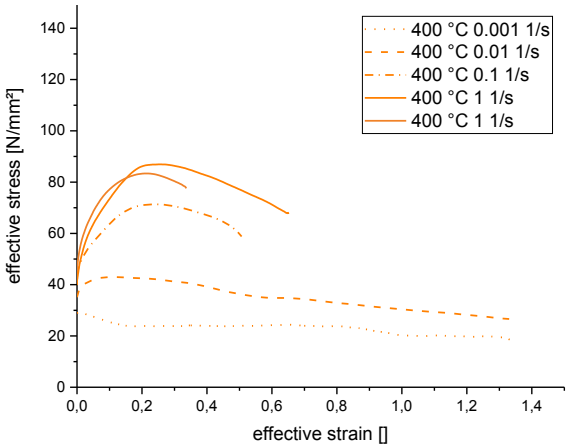

Figure 53: Flow curves at 400 °C. Deviating result at 1/s.

The applied heat treatment at 410 °C for 1 h correlates well with results reported in the literature for this temperature [8]. Also, in the present study incomplete dissolution of the $Mg_{17}Al_{12}$ β-phase has been obtained. The occurance of β-particles is similar, whilst solely the α+β-eutecticum has reduced significantly to an unmeasurable level. The present treatment was carried out shorter than suggested in the literature, as the microstructure after 1 h does not differ noticeable from a 24 hours' treatment. Also high-melting Al-Mn compounds and better soluble intermetallics as Mg_2Si remain in the material. Thus also long heat treatments can cause only an incomplete dissolution. Considering this aspect time consuming long-term heat treatments may be shortened drastically, as after 1 h similar results occur.

Figure 22 displays the temperatures during deformations at the highest strain rate. The graph shows the condition, at which most mechanical power is induced into the sample, whilst due to the low temperature gradient only little heat is conducted to the surroundings. The occuring temperature elevation does not exceed 10 °C. At lower strain rates a larger loss of heat is expected due to thermal conduction and has also been proved. Therefore, the mechanical heating seems to be negligible. Also, the power supply of the heating, which is reduced only by few percent during the deformation confirms this theory.

The flow curves were calcualted with the formula of Fields and Backofen (3.2.2). This method causes an inadequate result for materials with non-monotonic strain hardening behaviour [56]. Nevertheless, it was applied with constant values for every flow curve. Notwithstanding this approach Figure 54 shows the strain rate sensitivity as the slope of the stress versus the strain rate. At high strain rates a flattening can be observed. In the literature this tendency has been observed as a sigmoidal behaviour for tension after high pressure torsion of ZK60 [57], [58]. However, this flattening above $\dot{\varepsilon}$ = 0.1/s can be correlated with superplasticity at intermediate strains [58], which is unlikely to happen in the present case, because only quite low strains were achieved. As Figure 10 shows, the linear fit of the strain hardening coefficient correlates only in the central field of strains. The values at low strains are not crucial due to the logarithmic scale, whereas at high strains the total softening of the material is not considered, which has a significant influence on

the final flow curve. As this softening may also be influenced by the accumulating damage of the material, individualism of the samples complicates the application of a method of higher accuracy.

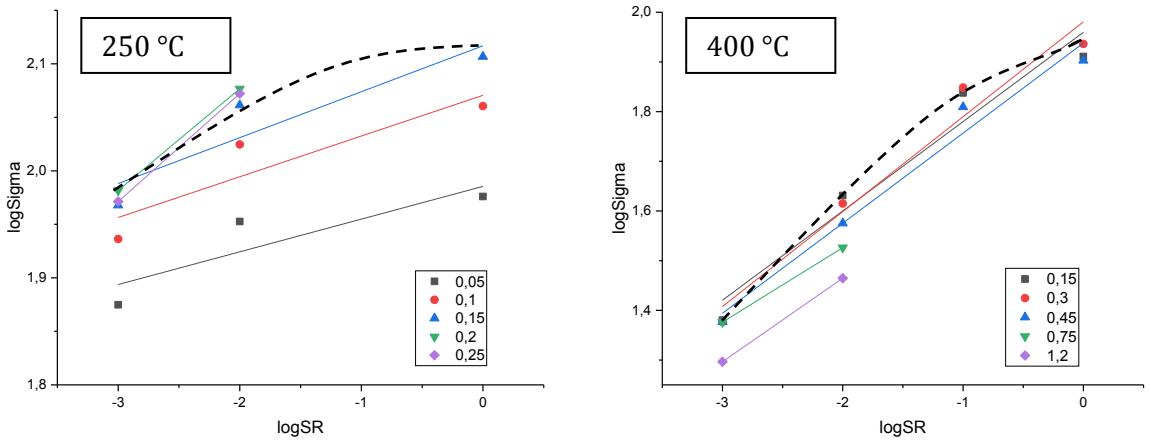

Figure 54: Strain rate sensitivity as slope of log σ / log ε̇ curves. 250 °C (left), 400 °C (right). The legend marks the revolutions at which the strains were recorded. The dashed lines represent a sigmoidal behaviour as described in [58].

Figure 55 demonstrates two different types of flow curve behaviour. At 250 °C the material hardens until it reaches an effective strain of 0.2 and breaks proximately after a very short softening. Similar behaviours show up in all of the flow curves in (a). Experiments at temperatures higher than 300 °C and up to moderate strain rates show low softening on steady state by lower strain rate (b).

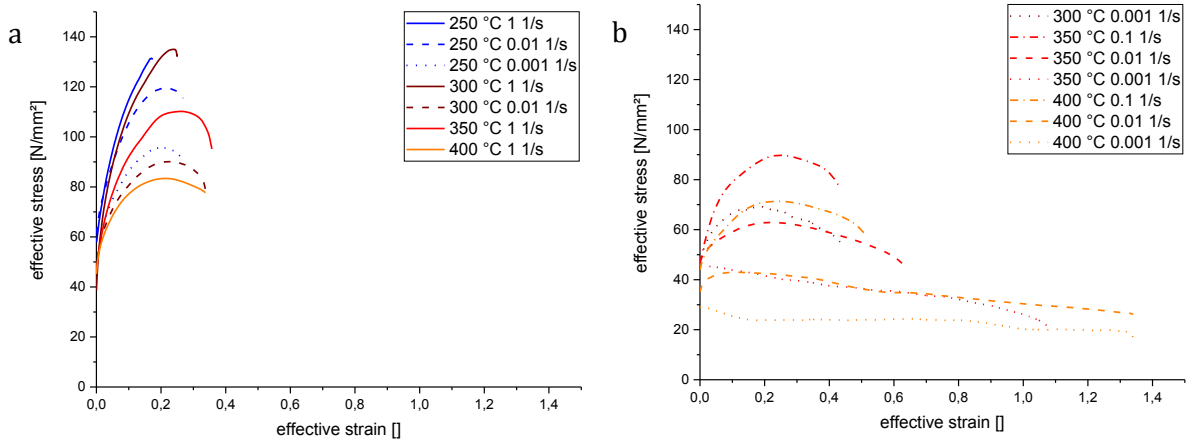

Figure 55: Flow curves with immediate softening (a) and a regime of stable stress (b).

The plot of the maximum stresses of the flow curves over the logarithmic strain rates in Figure 56 demonstrates linear correlations with similar slopes. A deviating result was obtained only at 250 °C. Considering the flow curve the reason seems apparent. The sample broke brittle before the flow curve reached the expected maximum.

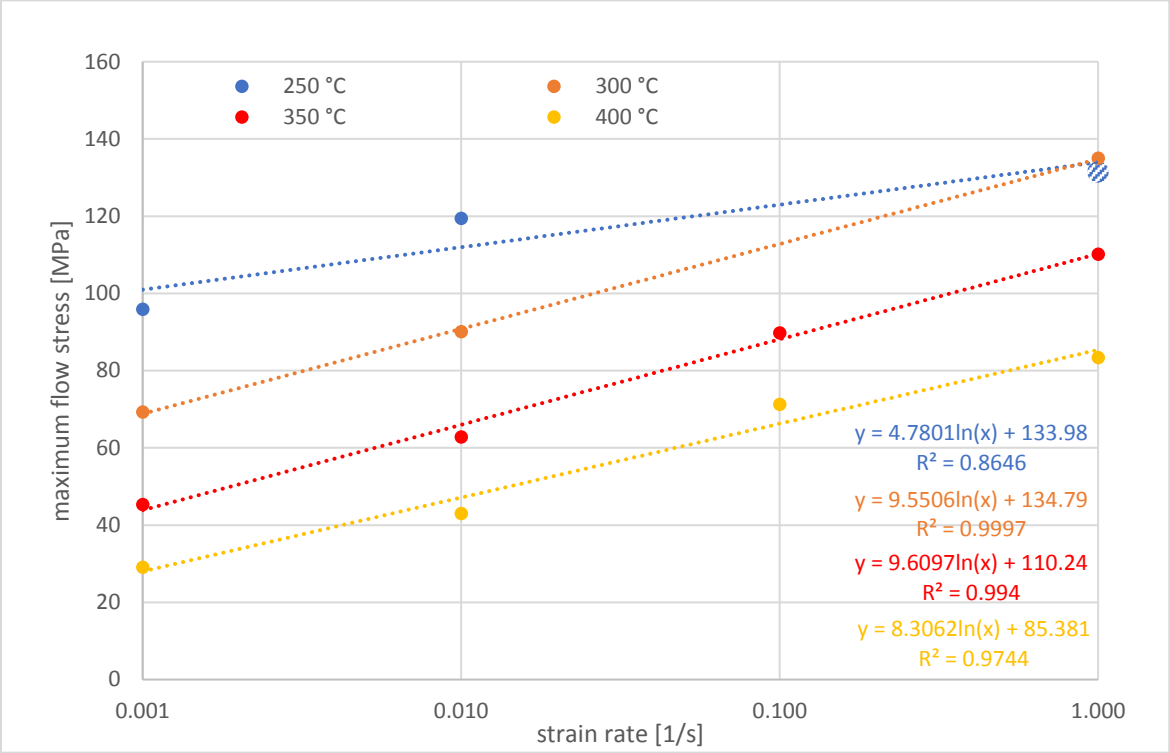

Figure 56: Maximum flow stress of all tested torsion conditions. Measurements fitted logarithmic. Measurement data of broken sample marked by dashed point.

When these results are correlated with the microstructure, it is remarkable, that a stable stress during deformation and therefore also a stable deformation happens only, when newly build grains occur. In the samples deformed at 300 °C with 0.01/s and at 400 °C with 1/s very large similarities appear. The two images in Figure 57 are especially comparable, due to their similar strains. In both samples twins as well as very fine grains can be found locally restricted to the grain boundaries. This similar microstructure also reflects in the flow curves.

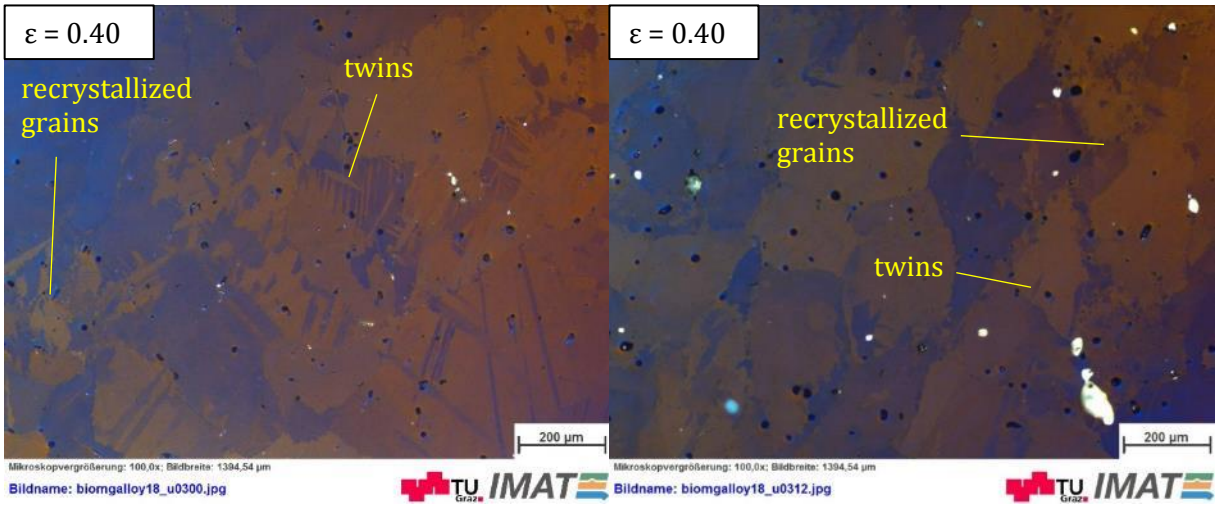

Figure 57: Light optical micrographs of torsion samples deformed at 300 °C with 0.01/s and at 400 °C with 1/s.

Small grains coming from recrystallization allow the material to achieve high strains, as the stresses remain stable and the material softens little. At high temperatures and low strain rates (350 °C, 400 °C, 0.001/s) a total lack of the hardening is noticeable and the flow curve softens from its beginning slightly. The material has enough time to recrystallize which enables deformations under low stresses.

At 250 °C after a deformation with 0.001/s recrystallization occures only in a very small amount (Figure 33). The tendency is detectable by twins, the changing misorientation and the occurence of small grains. However, these are in areas of low confidence index. Therefore their building mechanism is difficult to determine. In AM30 wrought material after torsion at 250 °C and strain rates of $7.5 \cdot 10^{-4}$/s continuous dynamic recrystallization has already been observed [34].

Another interesting detail of Figure 33 are the low angle grain boundaries. These occur at similar conditions as twin boundaries. Looking at the detail illustrated in Figure 58 an explanation for these low angle grain boundaries can be found: during deformation twins expand over the microstructure [16]. When one twin meets another, which originates from the same grain, its orientation is very similar. Consequently the twin boundaries annihilate and between the twins a boundary of low angle occurs.

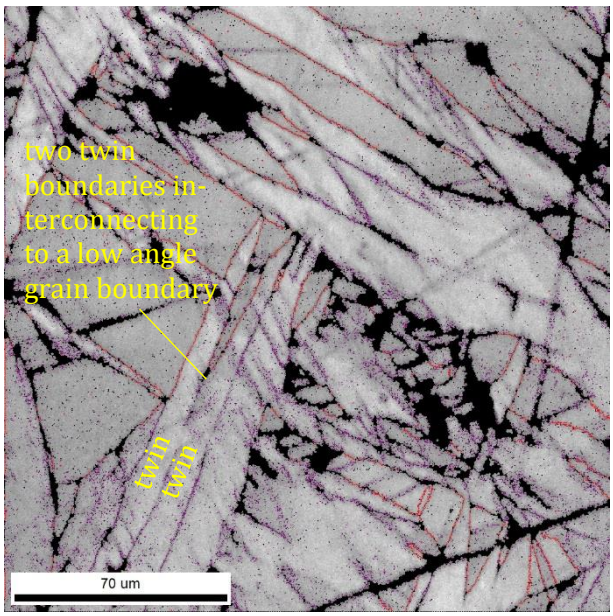

Figure 58: Image quality map of a detail of the sample deformed at 250 °C with 0.001/s. Grain boundaries highlighted.

What always has to be kept in mind, is that not only stress and strain are treated as effective values but the strain rate, too. These effective values provide a tendency about the situation within the material, though the circumstances in one single point of the sample are depending on its radius. The flow curves, however, contain the sum of all these single effects. Therefore, a change of the characteristics of a flow curve means always that the contributions of single microstructural features overtake others in large regions of the sample.

The micrographs show always the situation at the end of the experiment, which is often near to the strain at failure. The near-edge images are kept usually at a position in the material, which experienced the calculated effective values. As the strain decreases near to the sample´s centre, also the strain rate does. Therefore, an investigation of the microstructure within one sample at different radii gives no satisfying information about the evolution during the deformation. This knowledge can be gained only out of single experiments to different strains as Figure 59 demonstrates. Here dynamic recrystallization obviously took place, despite the low strain of 0.23.

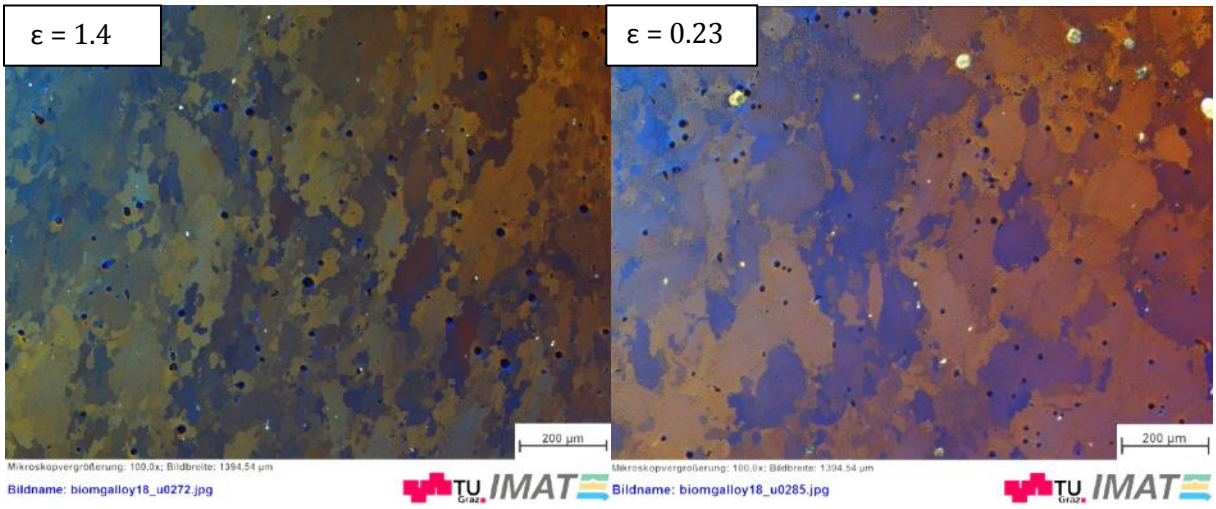

Figure 59: Microstructure at 400 °C under polarised light after a deformation with 0.01/s to different strains.

In the mostly recrystallized structure it is very difficult to identify previous restoration steps (Figure 38, Figure 39). An observation of microstructures in different samples revealed that recrystallization can originate at different features of the microstructure. Figure 60 (a) illustrates, that at 300 °C at the grain boundary a necklace structure forms, from which successively new grains grow into the deformed original grains.

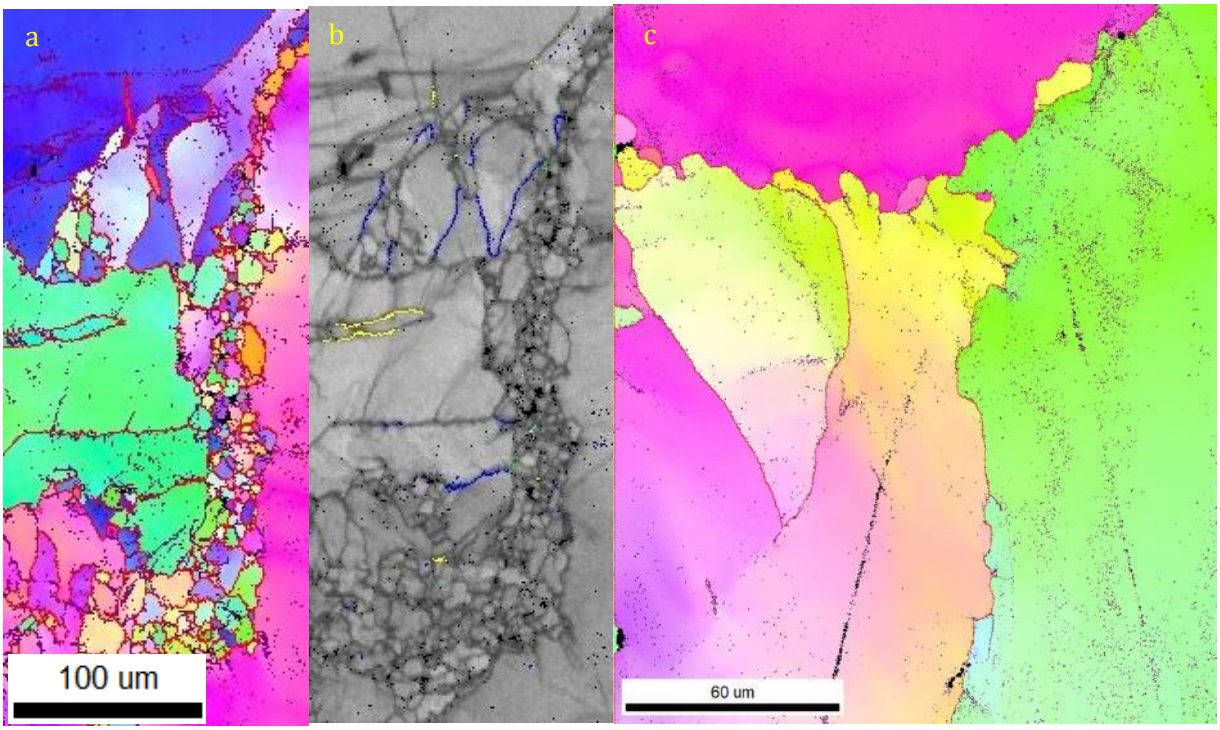

Figure 60: EBSD measurements after a 300 °C, 0.001/s deformation (ε = 0.50), twins highlighted in the image quality figure (b), grain boundaries and subgrain boundaries highlighted in the inverse pole figures (a & c). (a) necklace structure, (c) separation of grains at the grain boundaries.

Even if this evolution from the grain boundaries can be interpreted as discontinuous dynamic recrystallization, comparisons with the literature suggest to consider a continuous mechanism at the present condition. Discontinuous dynamic recrystallization occurs more likely at higher temperatures [26]. In [30] discontinuous effects are described for compressed ZK60 only at 400 °C and 0.01/s. For higher and lower strain rates continuous mechanisms have been observed. Also in AZ31 discontinuous effects are reported only for high temperatures (≥ 400 °C) and high strain

rates [31]. In [27], however, the critical temperature for discontinuous dynamic recrystallisation (for Mg-Zn-Ca alloys) is assumed to be at 280 °C.

Many of the recrystallized grains of Figure 60 (a) have a similar orientation as the surrounding original ones. Althogh, also features can be found within the same sample, which are more concise signals of continuous dynamic recrystallization. Figure 60 (c) shows grain boundaries, on which successively new grains separate, which have a similar orientation as the surrounding original grains. The misorientation within them does not differ significantly from the original large grains. Justifiably lattice rotation of new build grains can be assumed. In the present case the continuous effects arise up to 400 °C as Figure 38 illustrates. At the boundary of the reddish grain (position A) similar oriented small grains can be found, which might develop through lattice rotation.

The evolution of new grains at twin boundaries implies twin aided dynamic recrystallization. The process described in [32] with the serration of twin boundaries, however, hardly comes into appearence in the present images (Figure 60).

An examination of the enlarged violet grain in Figure 61 of the EBSD measurement of the sample deformed at 350 °C presents areas of similar orientation clearly fencing off others. The kernel average misorientation map highlights the interfaces between them obviously. A similar situation can be observed in Figure 35. The misorientation plot contains three subgrain boundaries of different intensity. In the kernel average misorientation map these appear very bright. The demonstrated characteristics are important points in favour for continuous dynamic recrystallization by progressive lattice rotation.

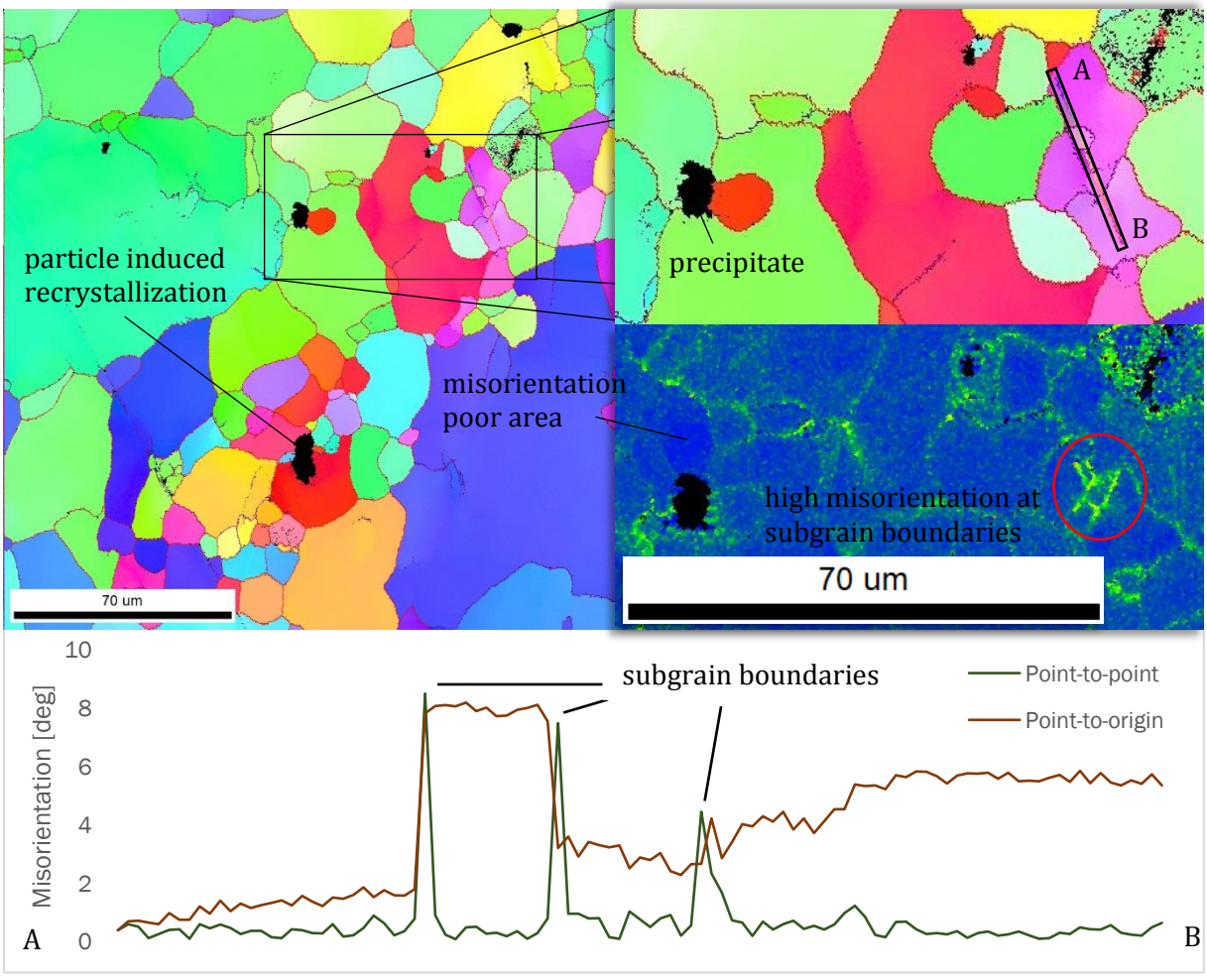

Figure 61: Detail of the EBSD measurement in a sample deformed at 350 °C with $\dot{\varepsilon}$ = 0.001/s. The development of subgrains can well be observed in the kernel average misorientation map in the violet grain.

The large black stain in the enlarged image of Figure 61is an intermetallic phase. Next to it a red recrystallized grain occurs. In the kernel average misorientation map a clear blue area can be found. This can be interpreted as a shadow of cleaned material left by a piling up of dislocations at the other side of the precipitate. Also in the left part of Figure 61 an accumulation of recrystallized grains occurs close to a precipitate. This effect, called particle induced nucleation, produces new grains with random orientation and has been observed e.g. for AZ31 [15]. Due to the discontinuous rearrangement of dislocations this nucleation can be the initialising step of discontinuous dynamic recrystallization[59].

Figure 62 illustrates the length of boundaries in differently wound samples. The logarithmic diagram contains the fraction of low angle grain boundaries for every EBSD measurement as well as 94.8 °, 34.8, 64.4 ° and 57 ° twins on 10 m large angle grain boundaries. In samples deformed with $\dot{\varepsilon}$ = 0.001/s the length of low angle boundaries decreases with the temperature. 94.8 ° tensile twins can be found in the 250 °C sample and with a lower total length after a deformation at 300 °C. In samples deformed at higher temperatures these twins occur one magnitude shorter in length. Considering the logarithmic scale, other twins hardly exist in the structure. Possible inaccuracies appear at the diagram´s bottom much stronger, than at 10 m. Therefore no clear tendency for the occurance of 34.8° and 64.3° twin boundaries can be concluded. Contrary, 57 ° twins can be evaluated at 250 and 300 °C with $\dot{\varepsilon}$ = 0.001/s, which were detected with high reliability in the images. For fast deformed samples ($\dot{\varepsilon}$ = 1/s) numerous low angle boundaries and 94.8 ° twins developed at 250 °C, while only 94.8 ° twins were observed at a deformation at 400 °C.

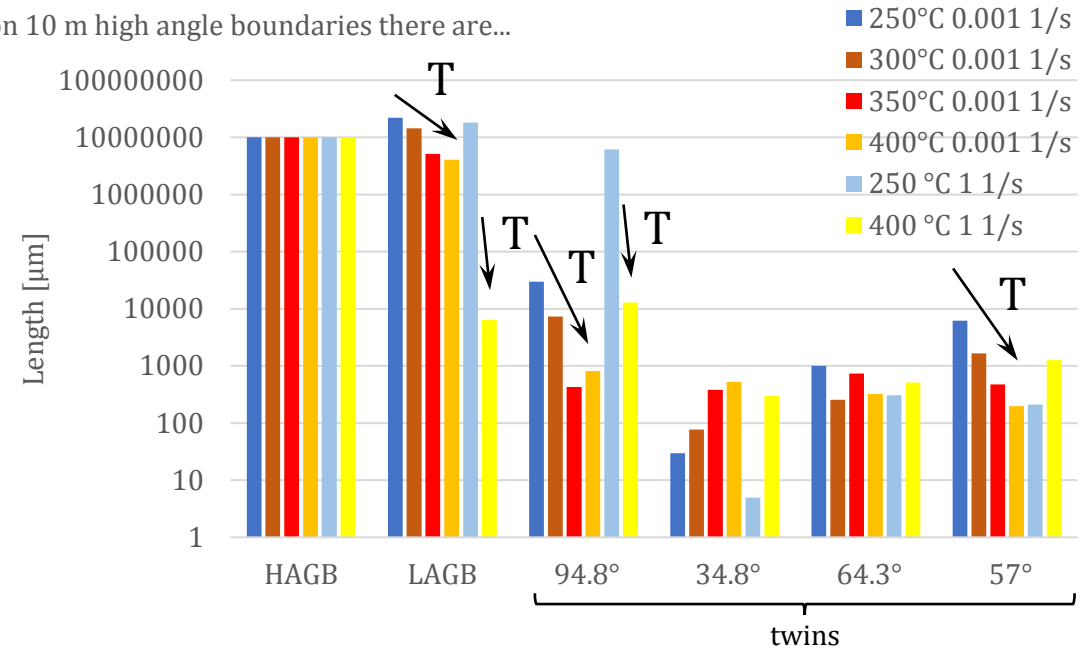

Figure 62: Length of low angle grain boundaries (LAGB) and different types of twins on 10 m of high angle grain boundaries in the figures on pages 39 to 45.

The graph in Figure 62 demonstrates, that there is a direct connection between twins and the peak stresses. Twins arise at low temperatures and at high strain rates. In these cases, also short flow curves without any stability occur. At low temperatures also a high total length of low angle grain boundaries can be observed. Their length decreases with the temperature, which can be explained by continuous dynamic recrystallization, by which low angle grain boundaries convert to high angle grain boundaries [38]. After fast deformation with $\dot{\varepsilon}$ = 1/s the fraction of low angle boundaries at 400 °C is much lower than after $\dot{\varepsilon}$ = 0.001/s. This can be an indication for the preference of continuous dynamic recrystallization at high strain rates, as described for Aluminium [60].

For the twin identification a tolerance angle of 6 ° was assumed. Higher tolerances risked the indication of normal grain boundaries as twins. However, at higher temperatures structures with obvious twin character were not recognised as twins. This can be observed in Figure 60. A possible explanation would be the change of twin angles during hot deformation by diffusion within the boundary. A poor indication also can be explained by low measurement quality [61].

By calculation of average grain sizes of the EBSD measurements no tendency with temperature or strain rate is possible, because prior grains are much larger than recrystallized ones.

Plotting the grains over their size, enables a differentiation between original and recrystallized grains. The area covered by smaller grains within the EBSD measurements is shown in Figure 63. After a deformation with 0.001/s large areas of potentially recrystallized grains arise between 20 and 80 µm for 350 and 400 °C. A low signal at 20 µm can also be found after a deformation with 1/s at 400 °C. The quantification of large grains is of low sufficiency, because in the small measured areas the appearance of large grains is coincidental.

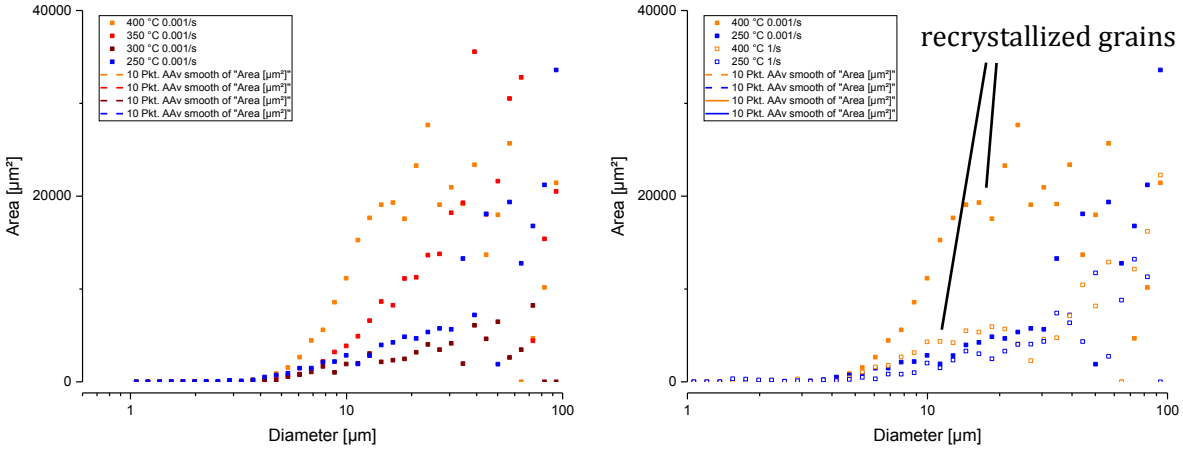

Figure 63: Areas in the EBSD measurements covered with grains of different size. Grains larger than 100 µm exist, but are not shown in this diagram due to strong fluctuations.

Taking the grain orientation spread into account a better differentition between original and recrystallized grains is possible. Figure 64 shows the microstructure excluding all grains, which have a orientational spread larger than 1.3 °. This threshold value results from individual validations of single grains.

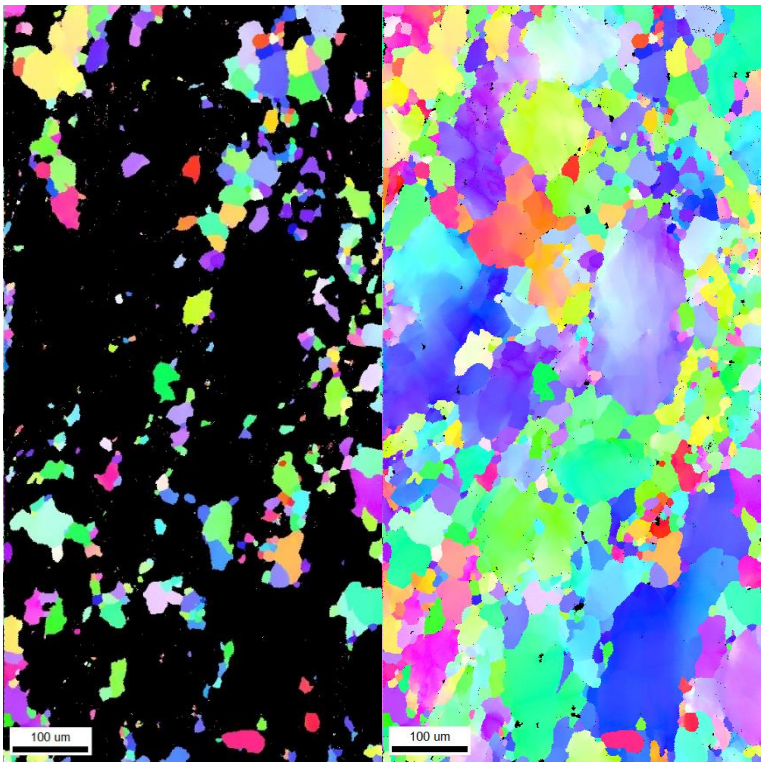

Figure 64: EBSD measurement in a sample deformed at 350 °C with $\dot{\varepsilon}$ = 0.001/s. Exclusion of grains with orientational spread higher than 1.3 °.

The area fraction of these grains was calculated and plotted in Figure 65. The graph shows a strong dependency of the size of recrystallised grains with the temperature. After deformations at low temperatures (250 °C, 300 °C) less than 5% of the measured area contains recrystallized grains, whilst after a 400 °C deformation more than 35% of the microstructure is recrystallized. This value does not seem very high, however, a consideration of grains with higher orientational spread, would have included also definitely deformed grains.

For the comparison of the recrystallized area fraction not only the different deformation temperatures, but also the different deformation grade has to be considered. The strain on the sample deformed with 0.001/ at 400 °C is 3 times larger than the strain, which was achieved at 300 °C.

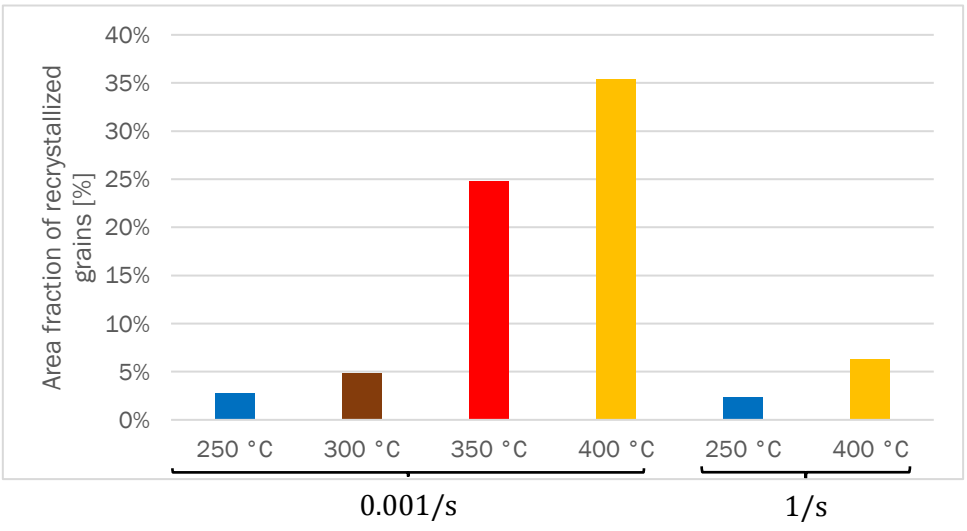

Figure 65: Plot of the area fraction of recrystallized grains of the EBSD measurement.

Additionally the average grain size of recrystallized grains has been calculated. For this calculations only grains with a size larger than 3.5 µm were taken into account, to exclude potential inaccuracies appearing as extremely small grains. The values are plotted in Figure 66. After a deformation at 0.001/s the grain size increases with the temperature from approximately 5 µm at 250 °C to more than 16 µm at 350 °C. The 400 °C measurement however, contains recrystallized grains which have an average grain size of about 9 µm, which is even smaller than the grains in the 300 °C sample. Comparing these results with the EBSD images Figure 33 to Figure 39, illustrates, that actually the recrystallization at 400 °C evolves numerous very small grains. The grain size is similar to the sample deformed with 1/s at the same temperature, whilst the area of recrystallized grains is much larger, which can be correlated again with the higher achieved strain.

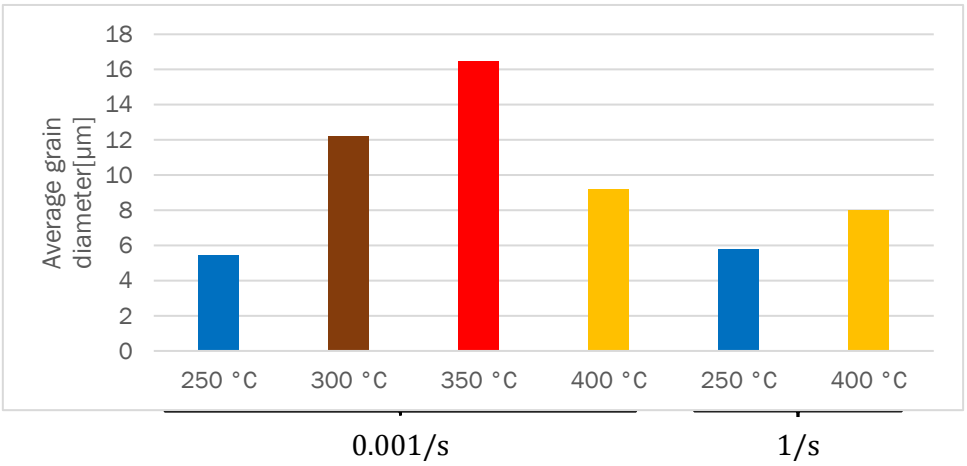

Figure 66: Average grain size of recrystallized grains of the EBSD measurements.

Additionally also the calculation method has to be considered as a potetial origin of inaccuracies. Grains with orientational spread lower than 1.3 ° could be origininal, but also recrystallized grains could have a higher spread. As the calculation indicates more than 2% of the area of the 250 °C 1/s measurement as recrystallized, whilst no further signals of this recrystallization were found, an inaccurate quantification must be assumed. Possible reasons are fragmentations of original grains or the comparison of samples deformed to different strains. Further, the microstructure has a wide spread of features, which suggests to enlarge the area of measurement significantly.

Contrary to observations at room temperature [62], no correlation between strain and twin thickness appeared in the deformed AM50. By contrast twins of different widths could be found at the same conditions, also in multiple layers.

5.2 Friction stir processing on AM50 and ZK40

The used parameters and tool for FSP proved good applicability on both magnesium alloys. For AM50 the first weld shows irregularities (Figure 40), which can be observed in the micrographs as pores too. All trials evolved thin layers of excessive material at the borders of the weld. This effect may result from a too low tool position. These two imperfections in the experimental conditions may correlate.

Within the stir zone inclusions of aluminium were found in both alloys. As the FSP tool was cleaned via stirring in aluminium, it is justifiable to assume, that the inclusions result from the cleaning process. The impurities do not affect the investigation of this thesis, however, for studies on mechanical loadability or corrosion there may show an influence.

Analysis of the process data showed interesting differences between the two alloys (Figure 67). The smooth surface of both welds for ZK40 is reflected in the shoulder force and spindle torque of the tests. ZK40 has a very stable weld process compared to other magnesium alloys as reported

in [52]. By contrast, the regarding Mg-Zn-Ca-Zr-Mn alloy, which has a very similar grain size as ZK40, suffered from large fluctuations. Therefore, another property of the material has to be the origin of the highly stable process in ZK40. Perhaps the occurence and amount of intermetallics due to the composition and the former heat treatment contribute to the differences. As described in [63] torque and force are prone to fluctuate when the weld is defective.

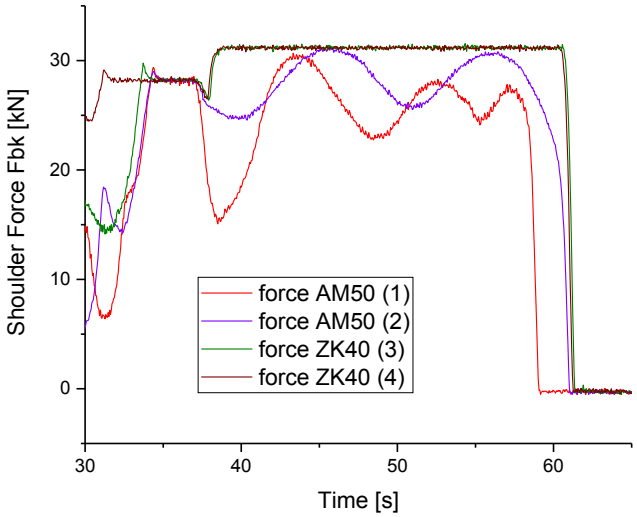

Figure 67: Shoulder force of all FSP tests.

The peak temperature measured during the tests reached from 420 °C to 460 °C, which is near to the solidus temperature for AM50 being 435 °C [13]. This is in good agreement with the literature, where peak temperatures of the process in the stir zone were determined to be 92% to 97% of the melting temperature of the welded material [42].

Regarding the microstructure several interesting characteristics can be analysed in the magnesium alloys. Differences between retreating and advancing side are highly pronounced and suggest a difference in material flow for both sides. This may also result in different material properties on both sides of the weld.

In AM50 small grains can be observed in the stir zone, but there are also areas yielding no information in the EBSD analysis (Figure 48). One possible explanation is that during the process of geometric dynamic recrystallization the formation of new grains in not complete and old grains are heavily deformed. Hence no defined Kikuchi patterns are observable.

The possibilities of orientation identification via EBSD are largely restricted within the stir zone. Althogh in many cases in ZK40 Kikuchi patterns were measured, a wrong indication resulted in poor final EBSD measurements. This may result from the appearance of several Kikuchi patterns at once. This effect is described for grain boundaries, resulting in an overlap of several patterns. Consequently, the quality of the analysis is diminished. In the present case the applied voltage was higher, resulting in a larger interaction volume. However, to make solely this overlap responsible for the low measurement quality, very small grain sizes must be assumed. By contrast the few clearly indicated grains in ZK40 had diameters between 1 and 4 µm, whilst the overlapping peak would be about one magnitude smaller. [64]

In ZK40 only few grains are identified in the stir zone by EBSD. Better measurements are only possible in the base material and the transition zones. Here light optical images reveal a possible prior substructure within grains in the transition zone to the weld (Figure 52). This could be an

indication for continuous dynamic recrystallization by lattice rotation in ZK40 too. Unfortunately the surface suffers of artefacts, which decrease the reliability of the interpretation.

5.3 Comparison of torsion and friction stir processing

Even though the process conditions of FSP are difficult to quantify compared to torsion tests, similar features occur in the deformed microstructure. Torsion at highest temperatures and lowest strain rates does not lead to a fully recrystallized structure. With FSP, at higher temperatures and higher strains, the grains become much smaller. However, there are signs indicating that the recrystallization is not to completed in friction stir processed AM50, too. The poorly indexed segment in Figure 48, interpreted as severly deformed grain could illustrate this assumption. For ZK40 in that sense no conclusions can be drawn.

A higher content of information could be gained out of the thermomechanical affected zone than of the stir zone. In this interface largely elongated grains were observed. Although, their appearance is different to deformed grains in the torsion sample, which have a low deformation and typically are surrounded by smaller recrystallized grains. In FSP samples, however, the local grain size is quite homogeneous and no differentiation between original and deformed grains is possible. These dissimilarities may be largely influenced by the higher temperatures, the severer deformation and axial pressures.

6 Conclusions and Outlook

The torsion tests in AM50 delivered well correlating flow curves with high achievable strains at 350 °C and 400 °C and low strain rates. Microstructural effects correspond to the characteristics of the flow curve. Recrystallization could be detected at 300 °C and higher temperatures. For deformation at 350 °C 0.001/s and 400 °C 0.01/s most of the microstructure was recrystallized. However, always severely deformed grains remained in the structure, characterised by higher misorientation within them. Therefore, the restoration has not completed. At high strain rates twins occured, their amount decreased with higher temperatures. Concerning the nature of the restoration indications, both discontinuous and continuous recrystallization were found in the microstructures. The accuracy of the microstructure would increase with a sufficient quenching system. Flow curves of higher validity could be obtained by considering changing regimes of the strain hardening coefficient and strain rate sensitivity, e.g. by a sigmoidal fit of these parameters. For further investigation of the recrystallization sequence, experiments up to different strains and with lower strain rates (< 0.001/s) should be performed, to gain knowledge about complete recrystallization. EBSD measurement in larger areas of the samples would enlarge the vality of quantification.

The chosen settings for the friction stir processes were sufficient on both alloys. Very regular surfaces developed on ZK40. In AM50 1- 5 µm large grains were detected, indicating a successful grain refinement. Future research should deal with the measurement of grain sizes in ZK40, where EBSD information was limited. Interrupted experiments by quenching would reveal the restoration sequence. Experiments with different parameters would deliver additional information of the influence of these parameters. For an industrial application, investigations on the material properties of the stirred zone are of great interest. This includes tensile tests, hardness tests and testing of the corrosion behaviour.

First approaches for the comparison of torsion tests and friction stir processing are delivered in this thesis, further research is necessary describing the missing links. In any case, an enhancement of the sample preparation is crucial for accurate investigation methods of the microstructure (Figure 68).

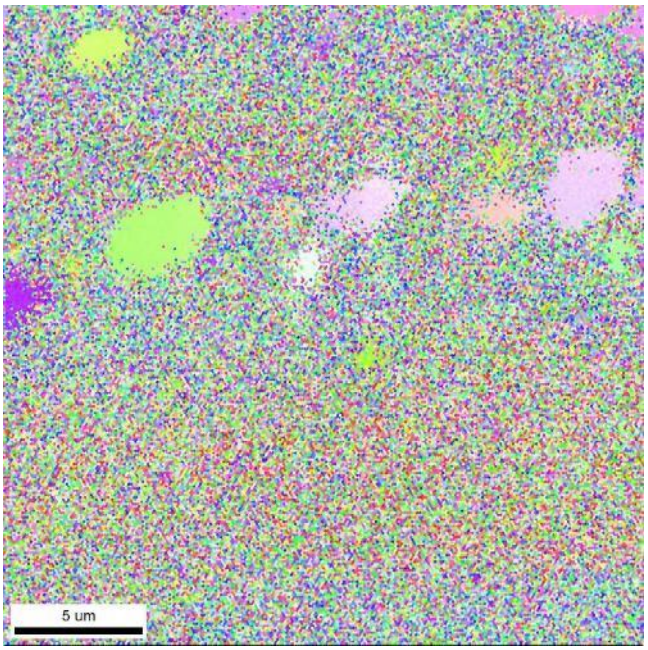

Figure 68: EBSD measurement in the stir zone of ZK40. Only few grains are indicated successfully.

7 Abbreviations

Al	Aluminium
Ca	Calcium
Cu	Copper
DC	Direct current
EBSD	Electron backscattered diffraction
EDX	Electron X-ray diffraction
Fe	Iron
FSP	Friction Stir Processing
HAGB	High angle grain boundary
LAGB	Low angle grain boundary
Mn	Manganese
Ni	Nickel
Si	Silicon
TC	Thermocouple
Zn	Zinc
Zr	Zirconium

8 Mathematical signs

l	mm	gauge length
n	-	hardening coefficient
m	-	strain rate sensitivity
r	mm	sample radius
t	s	time
M	Nm	torque
M_T	Nm	torque
N	rev	revolutions in torsion
T	°C	temperature
ε	-	effective strain
ε_{eff}	-	effective strain
ε_{max}	-	maximum strain in the torsion sample
$\dot{\varepsilon}$	1/s	strain rate
σ	N/mm^2	effective stress
ω	rev	revolutions in torsion
Ø	mm	diameter

9 References

[1] C. Kammer, *Magnesium Taschenbuch*, 1st ed. Aluminium-Verlag, Düsseldorf, 2000.

[2] Y. Templeman, G. Ben Hamu, and L. Meshi, "Friction stir welded AM50 and AZ31 Mg alloys: Microstructural evolution and improved corrosion resistance," *Mater. Charact.*, vol. 126, pp. 86–95, 2017.

[3] A. Zwahr, Ed., *Brockhaus Enzyklopädie*, 21st ed. Leipzig, Mannheim: F.A. Brockhaus, 2006.

[4] H.-J. Bargel and G. Schulze, *Werkstoffkunde, Springer-Lehrbuch*, 11th ed. Heidelberg, Dordrecht, London, New York, 2012.

[5] G. Franke, "Magnesium und Magnesium-Legierungen," *Korrosion und Korrosionsschutz*, pp. 1548–1579, 2001.

[6] K. K. Sankaran and R. S. Mishra, "Magnesium Alloys," in *Metallurgy and Design of Alloys with Hierarchical Microstructures*, Elsevier Inc., 2017, pp. 345–383.

[7] I. J. Polmear, "Magnesium Alloys," *Light Alloy.*, vol. 2, pp. 237–297, 2005.

[8] Y. Ma, J. Zhang, and M. Yang, "Research on microstructure and alloy phases of AM50 magnesium alloy," *J. Alloys Compd.*, vol. 470, no. 1–2, pp. 515–521, 2009.

[9] R. M. Wang, A. Eliezer, and E. M. Gutman, "An investigation on the microstructure of an AM50 magnesium alloy," *Mater. Sci. Eng. A*, vol. 355, no. 1–2, pp. 201–207, 2003.

[10] R. H. Buzolin *et al.*, "As cast microstructures on the mechanical and corrosion behaviour of ZK40 modified with Gd and Nd additions," *Mater. Sci. Eng. A*, vol. 682, no. August 2016, pp. 238–247, 2017.

[11] R. Arrabal *et al.*, "Effect of Nd on the corrosion behaviour of AM50 and AZ91D magnesium alloys in 3.5wt.% NaCl solution," *Corros. Sci.*, vol. 55, pp. 301–312, 2012.

[12] D. Hong *et al.*, "In vitro degradation and cytotoxicity response of Mg-4% Zn-0.5% Zr (ZK40) alloy as a potential biodegradable material," *Acta Biomater.*, vol. 9, no. 10, pp. 8534–8547, 2013.

[13] J. R. Davis, *ASM Handbook, Volume 2, Properties and selection: Nonferrous alloys and specific-purpose materials*. ASM International, 1990.

[14] L. Tan, X. Yu, P. Wan, and K. Yang, "Biodegradable Materials for Bone Repairs: A Review," *J. Mater. Sci. Technol.*, vol. 29, no. 6, pp. 503–513, 2013.

[15] F. Czerwinski, *Magnesium Alloys - Design, Processing and Properties*. 2011.

[16] R. H. Buzolin *et al.*, "In situ synchrotron radiation diffraction study of the role of Gd, Nd on the elevated temperature compression behavior of ZK40," *Mater. Sci. Eng. A*, vol. 640, pp. 129–136, 2015.

[17] Y. P. Ren, Y. Guo, D. Chen, S. Li, W. L. Pei, and G. W. Qin, "Isothermal section of MgZnZr ternary system at 345 ° C," *Calphad Comput. Coupling Phase Diagrams Thermochem.*, vol. 35, no. 3, pp. 411–415, 2011.

[18] L. Lin, Z. Liu, L. Chen, and F. Li, "Tensile properties and strengthening mechanisms of Mg-Zn-Zr alloys," *Met. Mater. Int.*, vol. 10, no. 6, pp. 507–512, 2004.

[19] D. F. Williams, "On the mechanisms of biocompatibility," *Biomaterials*, vol. 29, no. 20, pp. 2941–2953, 2008.

[20] Q. Chen and G. A. Thouas, "Metallic implant biomaterials," *Mater. Sci. Eng. R Reports*, vol. 87, pp. 1–57, 2015.

[21] Y. Ding, C. Wen, P. Hodgson, and Y. Li, "Effects of alloying elements on the corrosion behavior and biocompatibility of biodegradable magnesium alloys: A review," *J. Mater. Chem. B*, vol. 2, no. 14, pp. 1912–1933, 2014.

[22] Y. Zheng, *Magnesium Alloys as Degradable Biomaterials*. Boca Raton: Taylor and Francis Group, 2016.

[23] S. Agarwal, J. Curtin, B. Duffy, and S. Jaiswal, "Biodegradable magnesium alloys for orthopaedic applications: A review on corrosion, biocompatibility and surface modifications,"

Mater. Sci. Eng. C, vol. 68, pp. 948–963, 2016.

[24] M. P. Staiger, A. M. Pietak, J. Huadmai, and G. Dias, "Magnesium and its alloys as orthopedic biomaterials: A review," *Biomaterials*, vol. 27, no. 9, pp. 1728–1734, 2006.

[25] M. Muzyk, Z. Pakiela, and K. J. Kurzydlowski, "Generalized stacking fault energy in magnesium alloys: Density functional theory calculations," *Scr. Mater.*, vol. 66, no. 5, pp. 219–222, 2012.

[26] F. J. H. and M. Hatherly, *Recrystallization and Related Annealing Phenomena*, 2nd ed. Manchester, New South Wales: PERGAMON, 2004.

[27] M. Hradilová, F. Montheillet, A. Fraczkiewicz, C. Desrayaud, and P. Lejček, "Effect of Ca-addition on dynamic recrystallization of Mg-Zn alloy during hot deformation," *Mater. Sci. Eng. A*, vol. 580, pp. 217–226, 2013.

[28] M. M. Myshlyaev, H. J. McQueen, A. Mwembela, and E. Konopleva, "Twinning, dynamic recovery and recrystallization in hot worked Mg-Al-Zn alloy," *Mater. Sci. Eng. A*, vol. 337, no. 1–2, pp. 121–133, 2002.

[29] S. Yi, H. G. Brokmeier, and D. Letzig, "Microstructural evolution during the annealing of an extruded AZ31 magnesium alloy," *J. Alloys Compd.*, vol. 506, no. 1, pp. 364–371, 2010.

[30] Z. Y. Liu, T. T. Huang, W. J. Liu, and S. Kang, "Dislocation mechanism for dynamic recrystallization in twin-roll casting Mg-5.51Zn-0.49Zr magnesium alloy during hot compression at different strain rates," *Trans. Nonferrous Met. Soc. China (English Ed.*, vol. 26, no. 2, pp. 378–389, 2016.

[31] W. P. Peng, P. J. Li, P. Zeng, and L. P. Lei, "Hot deformation behavior and microstructure evolution of twin-roll-cast Mg-2.9Al-0.9Zn alloy: A study with processing map," *Mater. Sci. Eng. A*, vol. 494, no. 1–2, pp. 173–178, 2008.

[32] S. K. Chan Hee Park, Chang-Seok Oh, "Dynamic recrystallization of the H- and O-tempered Mg AZ31 sheets at elevated temperatures," *Mater. Sci. Eng. A*, vol. 542, pp. 127–139, 2012.

[33] H. Ding, K. Hirai, T. Homma, and S. Kamado, "Numerical simulation for microstructure evolution in AM50 Mg alloy during hot rolling," *Comput. Mater. Sci.*, vol. 47, no. 4, pp. 919–925, 2010.

[34] S. Biswas, B. Beausir, L. S. Toth, and S. Suwas, "Evolution of texture and microstructure during hot torsion of a magnesium alloy," *Acta Mater.*, vol. 61, no. 14, pp. 5263–5277, 2013.

[35] G. E. Dieter, *Mechanical Metallurgy*. London: Mc Graw-Hill Book Company, 1988.

[36] C. G. G. R. Canova, S. Shrivastava, J. J. Jonas, "The use of torsion testing to assess material formability," *Formability Met. Mater. A. D.*, vol. 753, pp. 189–210, 1982.

[37] S. R. Lampman, *ASM Handbook, Volume 8, Mechanical Testing and Evaluation*. 1990.

[38] S. Gourdet and F. Montheillet, "A model of continuous dynamic recrystallization," *Acta Mater.*, vol. 51, no. 9, pp. 2685–2699, 2003.

[39] M. S. Węglowski, "Friction stir processing – State of the art," *Arch. Civ. Mech. Eng.*, vol. 18, no. 1, pp. 114–129, 2018.

[40] K. Nakata, *Friction stir welding of magnesium alloys*, vol. 23, no. 5. Beijing: Woodhead Publishing Limited, 2009.

[41] Y. Huang *et al.*, "Friction stir welding/processing of polymers and polymer matrix composites," *Compos. Part A Appl. Sci. Manuf.*, vol. 105, pp. 235–257, 2018.

[42] S. Swaminathan *et al.*, "Peak Stir Zone Temperatures during Friction Stir Processing,"

Metall. Mater. Trans. A, vol. 41, pp. 631–640, 2010.

[43] R. C. Zeng, W. Dietzel, R. Zettler, J. Chen, and K. U. Kainer, "Microstructure evolution and tensile properties of friction-stir-welded AM50 magnesium alloy," *Trans. Nonferrous Met. Soc. China (English Ed.*, vol. 18, no. SPEC. ISSUE 1, pp. s76–s80, 2008.

[44] R. C. Zeng *et al.*, "Corrosion of friction stir welded magnesium alloy AM50," *Corros. Sci.*, vol. 51, no. 8, pp. 1738–1746, 2009.

[45] J. Babu, M. Anjaiah, and A. Mathew, "Experimental studies on Friction stir processing of AZ31 Magnesium alloy," *Mater. Today Proc.*, vol. 5, no. 2, pp. 4515–4522, 2018.

[46] X. Du and B. Wu, "Using two-pass friction stir processing to produce nanocrystalline microstructure in AZ61 magnesium alloy," *Sci. China, Ser. E Technol. Sci.*, vol. 52, no. 6, pp. 1751–1755, 2009.

[47] H. Zhang, *Friction stir welding of magnesium alloys*. Woodhead Publishing Limited, 2010.

[48] D. Qin, H. Shen, Z. Shen, H. Chen, and L. Fu, "Manufacture of biodegradable magnesium alloy by high speed friction stir processing," vol. 36, no. June, pp. 22–32, 2018.

[49] R. Zeng, W. Dietzel, F. Witte, N. Hort, and C. Blawert, "Progress and challenge for magnesium alloys as biomaterials," *Adv. Eng. Mater.*, vol. 10, no. 8, pp. 3–14, 2008.

[50] A. Kos, *Lieferschein AZ91 - AM50*. St. Georgen bei Salzburg: non ferrum GmbH, 2014.

[51] D. S. Inc., "Torsion operation manual," New York, 2017.

[52] K. Holzleitner, "Friction Stir Processing of a Microalloyed Magnesium for Biomedical Application," Technische Universität Graz, 2017.

[53] X. M. Chen *et al.*, "Fine-grained structure and recrystallization at ambient temperature for pure magnesium subjected to large cold plastic deformation," *Mater. Sci. Eng. A*, vol. 708, no. October, pp. 351–359, 2017.

[54] M. Asgar-Khan and M. Medraj, "Thermodynamic Description of the Mg-Mn, Al-Mn and Mg-Al-Mn Systems Using the Modified Quasichemical Model for the Liquid Phases," *Mater. Trans.*, vol. 50, no. 5, pp. 1113–1122, 2009.

[55] K. N. Braszczyńska-Malik and E. Przełożyńska, "Analyses of AM50-Tipmetal-metal composite microstructure," *J. Alloys Compd.*, vol. 731, pp. 1181–1187, 2018.

[56] S. Khoddam and P. D. Hodgson, "Conversion of the hot torsion test results into flow curve with multiple regimes of hardening," *J. Mater. Process. Technol.*, vol. 153–154, no. 1–3, pp. 839–845, 2004.

[57] S. A. Torbati-Sarraf and T. G. Langdon, "Properties of a ZK60 magnesium alloy processed by high-pressure torsion," *J. Alloys Compd.*, vol. 613, pp. 357–363, 2014.

[58] T. Langdon, "The mechanical properties of superplastic materials," *Metall. Trans. 13 A*, pp. 689–701, 1982.

[59] G. Gottstein, *Materialwissenschaft und Werkstofftechnik : Physikalische Grundlagen*. 2014.

[60] J. Zhao, Y. Deng, J. Tan, and J. Zhang, "Effect of strain rate on the recrystallization mechanism during isothermal compression in 7050 aluminum alloy," *Mater. Sci. Eng. A*, vol. 734, no. April, pp. 120–128, 2018.

[61] Y. Chen, L. Jin, J. Dong, Z. Zhang, and F. Wang, "Twinning effects on the hot deformation behavior of AZ31 Mg alloy," *Mater. Charact.*, vol. 118, pp. 363–369, 2016.

[62] B. Peng Chen, Fangxi Wang, Jamie Ombogo, "Formation of 60 ° boundaries between {10-

12} twin variants in deformation of a magnesium alloy," *Mater. Sci. Eng. A*, vol. 737, pp. 173–185, 2019.

[63] P. Shahi, M. Barmouz, and P. Asadi, *Force and torque in friction stir welding*. Tehran: Woodhead Publishing Limited, 2014.

[64] V. Tong, J. Jiang, A. J. Wilkinson, and T. Ben Britton, "The effect of pattern overlap on the accuracy of high resolution electron backscatter diffraction measurements," *Ultramicroscopy*, vol. 155, pp. 62–73, 2015.